UNIVERSITY OF CALIFORNIA, SAN DIEGO

Metallo-dielectric Nanolasers for Dense Chip-scale Integration

A dissertation submitted in partial satisfaction of the requirements for the degree Doctor of Philosophy

in

Electrical Engineering (Photonics)

by

Qing Gu

Committee in charge:

Professor Yeshaiahu Fainman, Chair
Professor Vitaliy Lomakin
Professor Shirley Meng
Professor Lu Sham
Professor Charles Tu

2014

The dissertation of Qing Gu is approved, and it is acceptable in quality and form for publication on microfilm and electronically:

_____

_____

_____

_____

_____
Chair

University of California, San Diego
2014

DEDICATION

To my family

°

EPIGRAPH

Weakness of attitude becomes weakness of character.

– Albert Einstein

TABLE OF CONTENTS

LIST OF FIGURES

LIST OF TABLES

ABBREVIATIONS

2D	two-dimensional
3D	three-dimensional
Al_2O_3	alumina
α-Al_2O_3	amorphous Al_2O_3
AlN	aluminum nitride
ALD	atomic layer deposition
CGW	composite gain waveguide
CMOS	complementary metal–oxide–semiconductor
CW	continuous wave
DFB	distributed feedback laser
EL	electroluminescence
FEM	finite element method
FWHM	full-width-at-half-maximum
I–V	current versus voltage
LASER	light amplification by stimulated emission of radiation
LED	light emitting diode
L–I	light output power versus injected current
MQW	multiple quantum well
MOSFET	metal–oxide–semiconductor field-effect transistor
PECVD	plasma-enhanced chemical vapor deposition
PIC	photonic integrated circuit
PL	photoluminescence
QED	quantum electrodynamics
QW	quantum wells
RC	resistor-capacitor
RIE	reactive ion etching
SPASER	surface plasmon amplification by stimulated emission of radiation
SPP	surface plasmon polariton
SiO_2	silicon dioxide
SiN_x	silicon nitride
SEM	scanning electron microscope
SOI	silicon-on-insulator
TE	transverse electric
TM	transverse magnetic
VCSEL	vertical-cavity surface-emitting laser
WDM	wavelength division multiplexing
WGM	whispering-gallery mode

ACKNOWLEDGMENTS

I would like to thank my advisor, colleagues and family for the help and support along this academic journey.

I would also like to thank Athena Pan for proof-reading the thesis.

Chapter 1, in part, is a reprint of the material as it appears in Q. Gu, J. S. Smalley, M. P. Nezhad, A. Simic, J. H. Lee, M. Katz, O. Bondarenko, B. Slutsky, A. , V. Lomakin and Y. Fainman, "Subwavelength semiconductor lasers for dense chip-scale integration," *Advances in Optics and Photonics,* vol. 6, pp. 1-56, 2014. The dissertation author was the primary co-researcher and author.

Chapter 2, in part, is a reprint of the material as it appears in Q. Gu, B. Slutsky, F. Vallini, J. S. Smalley, M. P. Nezhad, N. C. Frateschi and Y. Fainman, "Purcell effect in sub-wavelength semiconductor lasers," *Opt. Express,* vol. 21, pp. 15603-15617, 2013. and Q. Gu, J. S. Smalley, M. P. Nezhad, A. Simic, J. H. Lee, M. Katz, O. Bondarenko, B. Slutsky, A. Mizrahi, V. Lomakin and Y. Fainman, "Subwavelength semiconductor lasers for dense chip-scale integration," *Advances in Optics and Photonics,* vol. 6, pp. 1-56, 2014. The dissertation author was the primary researcher and author.

Chapter 3, in part, is a reprint of the material as it appears in F. Vallini, Q. Gu, M. Kats, Y. Fainman and N. C. Frateschi, "Carrier saturation in multiple quantum well metallo-dielectric semiconductor nanolaser: Is bulk material a better choice for gain media?" *Opt. Express,* vol. 21, pp. 25985-25998, 2013. The dissertation author was the primary co-researcher and co-author.

Chapter 4, in part, is a reprint of the material as it appears in Q. Gu, J. Shane, F. Vallini, B. Wingad, J. S. Smalley, N. C. Frateschi and Y. Fainman, "Amorphous Al_2O_3 shield for thermal management in electrically pumped metallo-dielectric nanolasers," *IEEE. J. Quantum. Electron.,* (Accepted). and Q. Gu, J. S. Smalley, J. Shane, O. Bondarenko and Y. Fainman, "Temperature effects in metal-clad semiconductor nanolasers," *Nanophotonics Journal*, (Accepted). and J. S. Smalley, Q. Gu and Y. Fainman, "Temperature dependence of the spontaneous emission factor in subwavelength semiconductor lasers," *IEEE. J. Quantum. Electron.,* vol. 50, pp. 175-185, 2014. The dissertation author was the primary co-researcher and co-author.

Chapter 5, in part, is a reprint of the material as it appears in Q. Gu, J. S. Smalley, M. P. Nezhad, A. Simic, J. H. Lee, M. Katz, O. Bondarenko, B. Slutsky, A. Mizrahi, V. Lomakin and Y. Fainman "Subwavelength semiconductor lasers for dense chip-scale integration," *Advances in Optics and Photonics,* vol. 6, pp. 1-56, 2014. The dissertation author was the primary co-researcher and author.

VITA

2014	Doctor of Philosophy, Electrical Engineering (Photonics), University of California, San Diego USA
2008	Bachelor of Applied Science, Electrical Engineering, University of British Columbia Canada

JOURNAL PUBLICATIONS

Qing Gu, Joseph ST Smalley, Janelle Shane, Olesya Bondarenko and Yeshaiahu Fainman, "Temperature effects in metal-clad semiconductor nanolasers," *Nanophotonics Journal*, (Accepted).

Qing Gu, Janelle Shane, Felipe Vallini, Brett Wingad, Joseph ST Smalley, Newton C. Frateschi and Yeshaiahu Fainman, "Amorphous Al_2O_3 shield for thermal management in electrically pumped metallo-dielectric nanolasers," *IEEE Journal of Quantum Electronics*, (Accepted).

Joseph ST Smalley, **Qing Gu** and Yeshaiahu Fainman, "Temperature dependence of the spontaneous emission factor in subwavelength semiconductor lasers," *IEEE Journal of Quantum Electronics,* vol. 50, no. 3, 175-185 (2014).

Qing Gu, Joseph ST Smalley, Maziar P. Nezhad, Aleksandar Simic, Jin Hyoung Lee, Michael Katz, Olesya Bondarenko, Boris Slutsky, Amit Mizrahi, Vitaliy Lomakin and Yeshaiahu Fainman, "Sub-wavelength semiconductor lasers for dense chip-scale integration," *Advances in Optics and Photonics*, vol. 6, no. 1, 1-56 (2014).

Felipe Vallini, **Qing Gu**, Michael Kats, Yeshaiahu Fainman and Newton C. Frateschi, " Carrier saturation in multiple quantum well metallo-dielectric semiconductor nanolaser: Is bulk material a better choice for gain media?" *Optics Express,* vol. 21, no. 22, 25985-25998 (2013).

Olesya Bondarenko, **Qing Gu**, Janelle Shane, Aleksandar Simic, Boris Slutsky, and Yeshaiahu Fainman, "Wafer bonded distributed feedback laser with sidewall modulated Bragg gratings," *Applied Physics Letters,* vol. 103, no. 4, 043105-043105 (2013).

Qing Gu, Boris Slutsky, Felipe Vallini, Joseph ST Smalley, Maziar P. Nezhad, Newton C. Frateschi, and Yeshaiahu Fainman, "Purcell effect in sub-wavelength semiconductor lasers," *Optics Express,* vol. 21, no. 13, 15603-15617 (2013).

Yeshaiahu Fainman, Dawn Tan, Steve Zamek, Olesya Bondarenko, Aleksandar Simic, Amit Mizrahi, Maziar Nezhad, Vitaliy Lomakin, **Qing Gu**, Jin Hyoung Lee, Mercedeh Khajavikhan and Boris Slutsky, "Passive and Active Nanophotonics," *Advances in Science and Technology*, vol. 82, 9-18 (2012)

Jin Hyoung Lee, Mercedeh Khajavikhan, Aleksandar Simic, **Qing Gu**, Olesya Bondarenko, Boris Slutsky, Maziar P. Nezhad, and Yeshaiahu Fainman, "Electrically pumped sub-wavelength metallo-dielectric pedestal pillar lasers," *Optics Express,* vol. 19, no. 22, 21524-21531 (2011).

Olesya Bondarenko, Aleksandar Simic, **Qing Gu**, Jin Hyoung Lee, Boris Slutsky, Maziar P. Nezhad, and Yeshaiahu Fainman, "Wafer bonded subwavelength metallo-dielectric laser," *IEEE Photonics Journal,* vol. 3, no. 3, 608-616 (2011).

Qing Gu, Werner Hofmann, Markus-Christian Amann, Lukas Chrostowski, "Optically Injection-Locked VCSEL as a Duplex Transmitter/Receiver," *IEEE Photonics Technology Letters*, vol. 20, issue 7, pp. 463--465 (2008)

ABSTRACT OF THE DISSERTATION

Metallo-dielectric Nanolasers for Dense Chip-scale Integration

by

Qing Gu

Doctor of Philosophy in Electrical Engineering (Photonics)

University of California, San Diego, 2014

Professor Yeshaiahu Fainman, Chair

Metal-clad nanolasers have recently become excellent candidates for light sources in densely-packed chip-scale photonic circuits. This dissertation focuses on the metallo-dielectric type of metal-clad nanolasers. To understand the quantum effects in nanoscale semiconductor lasers, a formal treatment of the Purcell effect, which describes the modification of the spontaneous emission rate by a sub-wavelength cavity, is first presented. This formalism is developed for the transparent medium condition, using the emitter-field-reservoir model in the quantum theory of damping, and its utility is demonstrated through the analysis and design of nanolasers. Next, the design, fabrication, and characterization of metallo-dielectric lasers under electrical pumping are discussed.

To achieve nanolasers with optimal performance, different active medium materials are compared, and, it is shown that that the commonly suggested multiple quantum well (MQW) structure may not be suitable for nanolasers. The interplay of various temperature-dependent parameters, as well as their effects on optical mode and emission characteristics are subsequently studied. Building on this knowledge, electrically pumped metallo-dielectric nanolasers amenable to room temperature operation are designed, with the focus on minimizing thermal heating and threshold gain. Preliminary experimental validation of the design is shown. Finally, future research directions toward high efficiency nanolasers and their integration into chip-scale photonic systems are discussed.

Chapter 1

Introduction

The infrastructure that supports modern society, including healthcare, education, transportation, finance, and scientific and technological research, has become inextricably tied to the continuous progress in the ability to generate, transmit, receive, and process information. While electronic devices integrated in highly complex circuits have enabled this progress, electronic devices and circuits suffer from inherent limitations, namely resistor-capacitor (RC) time delays [1]. To this end, photonic devices and circuits are envisioned to complement, and perhaps, eventually, supplant electronics as the enabling technology for continuous progress in the collection, transmission, and processing of information. In all photonic systems, an essential component is the light source. Optical sources with coherent emission of light, in the form of light amplification by stimulated emission of radiation (LASER), were first demonstrated in 1960 [2]. Like the first transistors, the first lasers were macroscopic devices, with footprints on the order of centimeters to decimeters.

As the cavity size is reduced with respect to the emission wavelength, interesting physical effects, unique to electromagnetic cavities, arise. Experiments in the radio and microwave frequencies first demonstrated that the spontaneous emission rate of atoms in

a cavity could be enhanced or inhibited, relative to their rate of emission in free space. The change in the spontaneous emission rate was found to depend on the geometry of the cavity as well as the orientation and spectra of the atoms [3]. In the 1990s, the first proposals and experiments were made to extend what has since become known as the Purcell effect to the optical regime. Modified spontaneous emission rates in dyes and semiconductors in optical microcavities were observed [4-7], and significant applications of the Purcell effect were reported, including diode lasers with greater modulation bandwidth [8-10], energy efficiency [11, 12], and absence of a threshold [13, 14]. While the concept of thresholdless operation continues to be a subject of debate [15, 16], the modulation and efficiency improvements enabled by wavelength-scale cavities are fairly well understood. For example, with proper design, the cavity of a sub-wavelength laser may be designed such that most of the spontaneous emission is channeled into the lasing mode [14, 17]. In so doing, unwanted emission into non-lasing modes is mitigated, and the below-threshold efficiency is limited only by non-radiative recombination. Since the observation of the Purcell effect in semiconductor cavities, lasing has been demonstrated in numerous wavelength and sub-wavelength scale structures. These structures include dielectric micro-discs [18-21], photonic crystals [11, 22-25], nanowires [26, 27], nano-membranes [28-30], micro-pillars [31-33], and metal-clad nanocavities [14, 34-38].

1.1 The history of laser miniaturization

To complement micro- and nano-electronics, optical components have undergone a process of miniaturization over the past several decades. Thus, it is not an exaggeration to state that the maintenance and improvement of modern society is directly related to

research advancements in photonic devices and circuits. Similar to transistors, the reduction of the size of lasers would enable a higher packing density of devices and lower power consumption per device. The first laser miniaturization came with the invention of solid state laser diodes [39] in which the device size was reduced from meter to millimeter scale. The invention of vertical-cavity surface-emitting laser (VCSEL) [40] enabled even further miniaturization down to tens of micrometers. More recently, micro-scale whispering-gallery mode (WGM) lasers were achieved in micro-pillars/discs [18, 41] and micro-spheres [42]. In parallel efforts, advancements towards optical mode miniaturization came with the use of 2D photonic crystals in laser designs [22]. While the active regions and the optical mode sizes of these lasers may be on the order of the emission wavelength, the entire structure is quite large due to the many Bragg layers needed to construct a cavity with high finesse. On the other hand, micro-pillars and micro-discs do not necessarily suffer from the same problem. However, until recently, packing a large number of micro-pillar/disk lasers with dielectric cavities in a small region was impractical, because the modes of these lasers are poorly confined to the active regions, and may extend well beyond the physical boundary of the cavities, leading to undesirable mode coupling of neighboring devices [19, 33].

The size of an optical cavity can be defined using different metrics, for example, the physical dimensions of the cavity or the size of the optical mode. If the goal of the size reduction is to increase the integration density, for example, in a laser array, then the effective cavity size should account for both the overall physical dimensions of the resonator and the spread of the optical mode beyond the physical boundary of the resonator. Throughout this thesis, we define the subwavelength cavities following this

metric. By this token, most conventional dielectric laser cavities are not amenable to dense integration because they either have a large physical footprint or a large effective mode volume V_{eff} (defined as $V_{eff} = V_a/\Gamma$, where V_a is the active region volume and Γ is the mode-gain overlap factor). For example, both distributed Bragg resonators and photonic crystal cavities can be designed to have very localized energy distribution and thus very small effective mode volumes. However, several Bragg layers or lattice periods are required to confine the mode and to maintain high finesse, resulting in physical footprints that are many wavelengths in size. On the other hand, it has been demonstrated that the diameter of thick (λ_0/n) microdisk lasers can be reduced below their free-space emission wavelength [21]. However, until recently, packing a large number of micro-pillar/disk lasers with dielectric cavities in a small region was impractical, because the modes of these lasers are poorly confined to the active regions, and may extend well beyond the physical boundary of the cavities, leading to unwanted mode coupling of neighboring devices [19, 33].

A true nanolaser, therefore, should be smaller than the free-space emitted wavelength in all three dimensions, both in terms of the device's physical footprint and optical mode confinement. Furthermore, it should be amenable to electrical injection. Devices with such characteristics are essential for various practical applications including densely integrated chip-scale photonic circuits, displays and sensors.

1.2 Fundamental scale limits of lasers

Before diving into specific nanolaser designs and various applications of nanolasers, we will first consider the fundamental limit on the size of a laser. A typical laser has two vital components. Firstly, it must have a resonator (or cavity) that supports optical mode(s). An inherent size limitation associated with the resonator is that the cavity length in the mode propagation direction cannot be shorter than half of the mode wavelength in the medium. Secondly, a laser must have gain (or active) medium that is population-inverted and supplies energy to the lasing mode(s). There needs to be enough gain medium such that population inversion can be achieved, which sets another restriction to the laser size. One exception is the exciton-polariton laser, which operates without a population inversion in the strong coupling regime. Exciton-polariton lasers were first introduced in 1996 [43], and were demonstrated to operate under electrical injection in 2013 [12, 44]. While they provide an intriguing foundation to explore the quantum coherence of matter [45, 46], the sizes of these lasers are significantly larger than their emission wavelengths, typically in the 10μm scale. Therefore, we do not focus on exciton-polariton lasers in this thesis.

With a conceptual understanding of the two principle elements of a laser, we use a Fabry-Perot cavity as an example to derive the size limits of a laser. Figure 1.1 shows a typical Fabry-Perot cavity. It is an optical resonator that consists of two mirrors with reflectivities r_1 and r_2, respectively, and the space between the mirrors is filled with gain medium. The propagation direction (also called longitudinal direction) is denoted by the z-axis, while the wave-guiding plane (also called transverse direction) is denoted by the xy-plane, schematically shown in Figure 1.1.

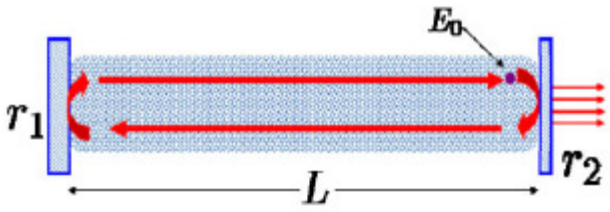

Figure 1.1: Schematic of a conventional Fabry-Perot cavity. The cavity length, L, is along the z-direction in which the wave propagates. The two end-facets have reflection coefficient r_1 and r_2, respectively.

In order for a cavity mode to get amplified, standing waves need to form in the longitudinal z-direction. Physically, it means that a complex field amplitude, $E_0(z)$, at an arbitrary location z inside the cavity, will maintain its original value after a round trip propagation. We denote the complex permittivity of the gain medium as $\varepsilon_g(\omega)=\varepsilon_g'(\omega)+i\varepsilon_g''(\omega)$ and the wave vector as $k(\omega)=k_0(\omega)\sqrt{\varepsilon(\omega)}$, where $k_0(\omega)=\dfrac{\omega}{c}$ is the vacuum wave vector. The standing wave requirement is mathematically expressed as

$$r_1 r_2 e^{i2k_z(\omega)L}E_0(z)=E_0(z) \tag{1.1}$$

Equation (1.1) can be understood by inspecting the effect of the real and imaginary parts of $k_z(\omega)=k_z'(\omega)+ik_z''(\omega)$ separately. The minimum length, $L_{\min}^{long,1}$, asserted by the real part of $k_z(\omega)$, is

$$\begin{aligned} &2k_z'(\omega)L=2m\pi, m=1,2,3,\cdots \\ &L_{\min}^{long,1}=\frac{m\pi}{k_z'(\omega)}=\frac{m\pi\cdot k_0(\omega)}{\mathrm{Re}\left(n_{eff}(\omega)\right)} \end{aligned} \tag{1.2}$$

with effective index defined as $n_{eff}(\omega)\equiv k_z(\omega)/k_0(\omega)$. On the other hand, $L_{\min}^{long,2}$, asserted by the imaginary part of $k_z(\omega)$ is

$$r_1 r_2 e^{-2k_z''(\omega)L} = 1$$
$$L_{\min}^{long,2} = \frac{\ln(r_1 r_2)}{2k_z''(\omega)} = \frac{-\ln(r_1 r_2)}{G_m} \tag{1.3}$$

where G_m is the modal gain. Equation (1.2) describes the half-wavelength condition, also known as the diffraction limit. This applies to all electromagnetic waves and sets a limit to the gain medium size. Equation (1.3) describes the relationship between the length requirement and G_m, ensuring that there is enough gain to compensate for the cavity losses, including the mirror losses as well as the mode gain/loss. It is the underlying principle behind the design of the second component of a laser. In a conventional macro-scale Fabry-Perot cavity, $L_{\min}^{long,2}$ is much larger than $L_{\min}^{long,1}$.

In the transverse xy-plane, as the width of the waveguide core decreases to the subwavelength scale in conventional dielectric surroundings, a significant portion of the modal profile spreads into the dielectric cladding, which reduces the gain-mode overlap and increases scattering loss. Although the first order transverse modes have no cut-off frequency and therefore no cut-off size requirement, guided modes transition into radiation modes as the width of the waveguide core decreases beyond half wavelength.

This simple example shows that, Fabry-Perot lasers, and waveguide-based lasers in general, are ultimately limited by the two characteristic lengths described above. Both electronic waves in electronics and photons in photonic devices are electromagnetic waves. Nevertheless, the wavelengths of electrons are orders of magnitude shorter than photons in optical frequencies. It is thus evident why there is a size mismatch between the miniaturization of electronic and photonic devices. In the field of nanolaser, the ultimate

goal is to reduce the characteristic lengths, $L_{\min}^{long,1}$ and $L_{\min}^{long,2}$, without violating any laws of physics.

To reduce the diffraction limited characteristic length, one needs to increase $k_z'(\omega)$, or equivalently, $\mathrm{Re}(n_{eff})$, in Equation (1.2). Similar to that employed in optical fibers, the most intuitive method is to increase the absolute refractive index of the gain medium in the waveguide core while minimizing that of the dielectric surrounding. For example, for purely semiconductor based lasers in the 1550 nm telecommunication wavelength regime, the gain medium refractive index is around 3, resulting in a half-wavelength of only 250 nm. A number of nanoscale laser and light emitting diode (LED) designs have adopted this approach [47].

To further reduce the half-wavelength, one can increase the mode confinement factor Γ and thus, $\mathrm{Re}(n_{eff})$, by incorporating metal into device designs. Because of the negative real part of metal permittivity at optical frequencies, field penetration into metal is minimal. As a result, a metal-clad waveguide can guide modes that would otherwise be radiating in a pure dielectric waveguide of the same sub-wavelength core size. However, material loss in metals, represented by the large positive imaginary part of the permittivity, is significant at optical frequencies. This is also related to the second length limitation determined by the population inversion requirement of a laser.

To reduce the population-inversion-limited characteristic length in Equation (1.3), the modal gain and/or the end-facet reflectivity need to be increased. The modal gain G_m is related to the material gain and confinement factor Γ. While material gain is fixed for any material at a given pump level and temperature, Γ can be manipulated by cavity

mode design. In conventional lasers where wave-guiding is weak and the wave propagation is qausi-paraxial, Γ can be defined as either the power or the energy in the gain medium divided by that of the entire optical mode. In nanolasers, this power confinement factor definition becomes invalid, because it may exceed unity as the guiding becomes strong. Instead, Γ is defined as the energy confinement factor in nanolasers [48]. It has been proposed that large modal gain can be achieved in metal-clad nanolasers [49, 50]. In terms of facet reflectivity, although enhancing the reflectivity can shorten $L_{\min}^{long,2}$, it also limits the available output power. Additionally, the Fresnel formula used to approximate mirror loss in conventional lasers breaks down on the nanoscale, and more accurate calculation needs to be used [51].

Laser miniaturization therefore involves the search for the optimal design of constituent materials, optical modes, cavity geometry and end-facet reflectivity, such that the significant material and end-facet losses can be compensated by the high modal gain in a small cavity. To this end, the metal-clad waveguide-based nanolaser was introduced [34].

1.3 The metal-clad nanolaser

Since its inception [34], the metal-clad nanolaser has emerged as a technologically relevant light source capable of operation at room temperature, first under pulsed optical pumping [35], then under continuous wave (CW) electrical injection [37]. In this thesis, we focus on this type of nanolasers.

Guided modes in metal-clad waveguide-based nanolasers can be grouped into two main categories: (i) if the real part of the propagation constant, $k_z'(\omega)$, satisfies $k_z'(\omega) < k_0(\omega)\sqrt{\varepsilon_g'(\omega)}$, the wavevector projection along the dielectric-metal interface is shorter than that of a plane wave in the dielectric alone, and which results purely from reflections within the metal cavity. In this case, the guided modes are photonic modes, which are conventional resonant modes. (ii) if the real part of the propagation constant satisfies $k_z'(\omega) > k_0(\omega)\sqrt{\varepsilon_g'(\omega)}$, the wavevector projection along the dielectric-metal interface is longer than that of a plane wave in the dielectric alone. The guided modes under this condition are surface-bound, plasmonic resonant modes (that is, surface plasmon polariton (SPP) modes).

SPP modes are highly confined and thus have high $\mathrm{Re}(n_{eff})$, especially near the SPP resonance where the real part of the wavevector reaches a maximum [52]. The disadvantage of SPP modes is the relatively large mode overlap of the optical field with the metal, which implies high Joule loss, again especially near the SPP resonance where the imaginary part of the wavevector reaches a minimal negative value. One possible solution to the metal loss obstacle is to reduce the temperature of operation. This simultaneously provides two benefits – a reduction of the Joule losses in the metal and an increase in the amount of achievable semiconductor gain. Hill et al. [34] demonstrated the first metal-clad semiconductor nanolaser, in which cryogenic lasing was achieved in gold-coated semiconductor cores with diameters as small as 210 nm. Another solution to the loss in metal is to operate the device in a frequency range much below the SPP

resonance, where loss is less severe and can be fully compensated by gain [53, 54]. Alternatively, one could operate near the SPP resonance in a metal-semiconductor-metal structure in which significant modal gain has been shown in certain ranges of material gain values [49].

In the meantime, the negative real parts of the permittivities of metals not only allow them to support SPP modes, but also enable them to act as efficient mirrors. This leads to the second class of metal-clad cavity modes that utilizes photonic modes, which can be viewed as lossy versions of the modes in a perfectly conducting metal cavity. Because the overlap between the mode and the metal is usually much smaller for these modes, a cavity supporting this type of modes is able to achieve higher Q factors and lower lasing gain thresholds, albeit at the expense of reduced mode confinement (compared to SPP modes). In general, both types of modes can exist in a metal-clad cavity.

Related to the SPP mode lasers, another type of optical source, SPASERs (Surface Plasmon Amplification by Stimulated Emission of Radiation), was proposed by Bergman and Stockman [55] in 2003. The emission modes in SPASERs are surface plasmon modes whose localization lengths are on the scale of tens of nanometers [52]. Although this is an exciting new area of research, we do not investigate this type of nano-emitters in this thesis.

For illustration purposes, an azimuthal index M = 4 WGM of a semiconductor disk with radius r_c = 460 nm and height h_c = 480 nm (Figure 1.2(a)) is shown in Figure 1.2(b), clearly indicating the radiating nature of the mode and its spatial spread, which, as mentioned, can lead to mode coupling with nearby structures. Embedding the

aforementioned gain disk in a gold cladding (Figure 1.2(c)) effectively confines the resonant modes, at the expense of increasing Joule losses. For approximately the same free space wavelength, the SPP mode (Figure 1.2(e)) has both a larger M number and higher losses (M = 6, Q = 36) compared to the photonic mode (Figure 1.2(d), M = 3, Q = 183). It should be noted that even though the metal cladding is the source of Joule loss, the large refractive index of the semiconductor core ($n_{semi} \approx 3.4$) aggravates the problem and increases both the plasmonic and reflection losses. For SPP propagation on a (planar) semiconductor–metal interface, the threshold gain for lossless propagation is proportional to n^3_{semi} [53]. This means that, even though SPP modes with relatively high Q can exist inside metal cavities with low-index cores (for example, silicon dioxide (SiO_2), n = 1.48), using this approach to create a purely surface bound plasmonic, room-temperature semiconductor laser at telecommunication wavelengths becomes challenging, due to the order-of-magnitude increase in gain threshold.

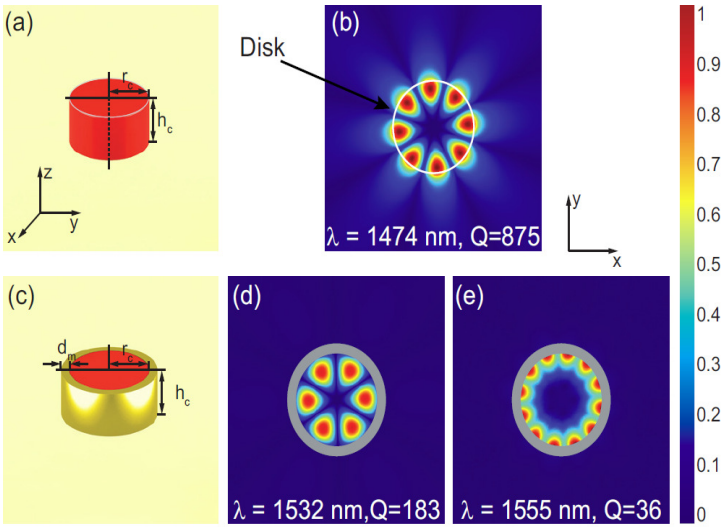

Figure 1.2: The M=4 whispering gallery resonance for a thick semiconductor disk (a) is shown in (b). (r_c = 460 nm, h_c = 480nm, n_{semi} = 3.4). Note the spatial spread of the mode compared to the actual disk size. (c) The same disk encased in an optically thick (d_m = 100 nm) gold shield will have well-confined reflective (d) and SPP (e) modes but with much higher mode losses. |E| is shown in all cases and the section plane is horizontal and through the middle of the cylinder.

To combat the high metal loss in the cavity modes described above, it has been shown that metal losses may be minimized when a dielectric "shield" layer is placed between the active region and the metal cladding [56]. Consider a composite gain waveguide (CGW) having a cylindrical gain medium core, a shield layer, and a metallic cladding, as shown in Figure 1.3(a). For a given CGW cross sectional area, the shield layer thickness is then tuned to maximize the confinement of the electric field in the gain medium and minimize the field penetration into the metal. In so doing, we increase the ability of the device to compensate for the dissipated power with power generated in the gain medium. A direct measure of this ability is the waveguide threshold gain, i.e., the gain required for lossless propagation in the CGW. The field attenuation in the shield layer resembles that of Bragg fibers [57]. The layer adjacent to the core, in particular, is

of high importance and is also used to reduce the loss in infrared hollow metallic waveguides.

The CGW model can also be used to design sub-wavelength 3D resonators. To confine the light in the longitudinal direction, the CGW is terminated on both sides by a low index "plug" region covered with metal, which forms the closed cylindrical structure shown in Figure 1.3(b). A more practical nanolaser configuration from a fabrication point of view is the open structure with a SiO_2 substrate shown in Figure 1.3(c). The inherent radiation losses into the substrate provide means for collecting the laser light, in contrast to the closed structure, where extracting light requires modification of the metal coating, such as opening an aperture. The threshold gain for the 3D resonator, defined as the gain required to compensate for the metal losses in the closed structure or to compensate for both the metal and the radiation losses in the open structure, is shown in the following sections to be sufficiently low to allow lasing at room temperature. The details of the optical mode design and gain threshold optimization can be found in Ref [56]. Because of the important role of the dielectric "shield" layer in the CGW-based nanolaser design, this class of metal-clad nanolaser is also called the metallo-dielectric nanolaser.

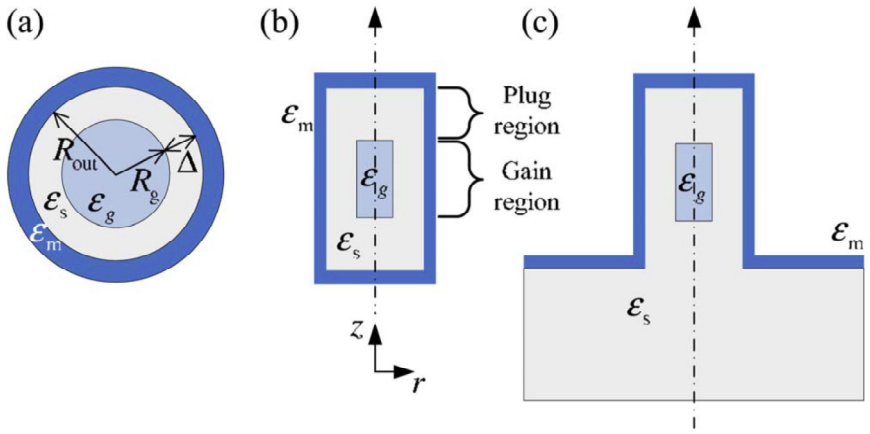

Figure 1.3: (a) Cross section of the metal-coated composite gain waveguide. (b) Cylindrical closed 3D resonator. (c) Cylindrical open 3D resonator.

Note that the discussion so far has assumed that light propagates in the z-direction and is guided in the xy-plane, as in conventional waveguide lasers (Figure 1.1) and in cylindrical nanolasers (Figure 1.4(a)). However, the distinction between propagation and guiding directions becomes less obvious as the size of a laser approaches one wavelength in all three dimensions, such as the nanocavity schematically shown in Figure 1.3(c) and Figure 1.4(b).

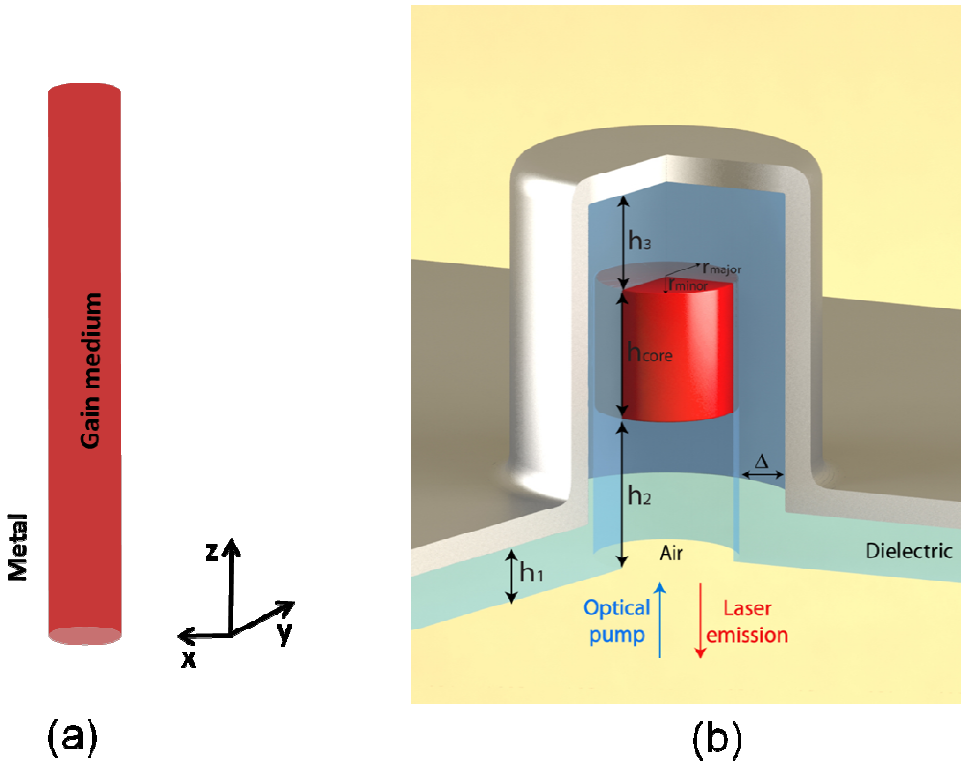

Figure 1.4: (a) A metal-clad cylindrical nanocavity with a subwavelength gain medium cross section, acting as a Fabry-Perot nanolaser, and (b) A metal-clad nanocavity whose size is subwavelength in all three dimensions.

Optically pumped metal-clad nanolasers using the CGW design have been demonstrated at room temperature [35]. The target device is schematically shown in Figure 1.4(b), in which a gain core is suspended in a bi-layer shell of SiO_2 and metal. The gain material is InGaAsP MQW with height h_{core}=480 nm, and the major and minor core radii of the slightly elliptical gain (caused by fabrication imperfections) are r_{major}=245 nm and r_{minor}=210 nm, respectively. The SiO_2 shield layer has thickness $\Delta \approx 200$ nm, and aluminum is used as the metal-cladding. The device is pumped through the bottom aperture and the emitted light is also collected from the same aperture. The cross-sections of $|\boldsymbol{E}|$ for the target TE_{012} photonic mode are depicted in Figure 1.5.

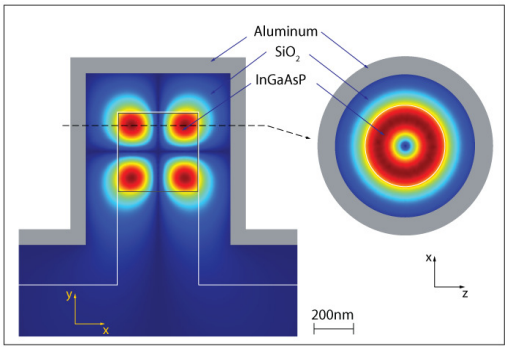

Figure 1.5: Cross-sections of |E| for the TE_{012} mode of the cavity.

A standard micro-photoluminescence (PL) setup was used for measurements. A 1064 nm pulsed fiber laser (300 kHz repetition rate, 12 ns pulse width) was used for optical pumping. The pump beam was focused onto the samples using either a 20× or 50× long-working-distance microscope objective, which also collected the emitted light. To estimate the amount of pump power absorbed by the core, a full three-dimensional finite-element analysis was carried out over a range of core sizes. Using a double 4-f imaging system in conjunction with a pump filter (Semrock RazorEdge long wavelength pass), the samples were imaged onto either an IR InGaAs camera (Indigo Alpha NIR) or a monochromator (Spectral Products DK480) with a resolution of 0.35 nm and equipped with a cooled InGaAs detector in a lock-in detection configuration. In Figure 1.6(a), the light–light curve corresponding to a laser emitting at 143 0nm is shown. It shows a slope change indicating the onset of lasing at a pump intensity of about 700 W/mm^2. The same data set is shown in a log-log plot (Figure 1.6(a), inset graph), with the slopes of different operation regions indicated on the plot. The S-shaped curve clearly shows the transition from PL to amplified spontaneous emission (ASE) and finally to the lasing regime. Also shown in Figure 1.6(a) are the emission patterns of the defocused laser images captured with the IR camera, corresponding to CW (Figure 1.6(a)-I) and pulsed (Figure 1.6(a)-II)

pumping configurations. The average pump intensity in each case was approximately equal to 8 W/mm^2. Only broad PL emission occurs in the CW case, owing to the low peak intensity. However, when the pump is switched to pulsed mode, lasing is achieved due to the 278-fold increase in peak power. At the same time, the defocused image forms a distinct spatial mode with increased fringe contrast, indicating increased spatial coherence and therefore, lasing. The polarization of the emission has a strong linear component, which is due to the slight ellipticity of the gain core resulting from fabrication imperfections. Figure 1.6(b) shows the evolution of the emission, from a broad PL spectrum to a pair of competing ASE peaks and finally into a narrow lasing line at 1430 nm with 0.9 nm width.

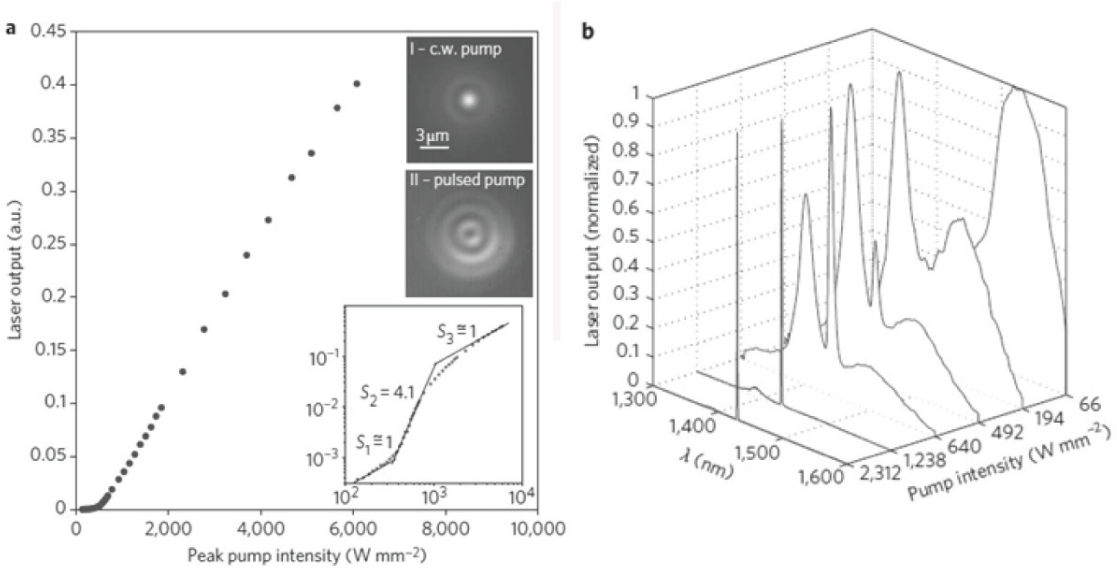

Figure 1.6: (a) Light–light curve for a nanolaser with major and minor core diameters of 490 nm and 420 nm (dotted curve). The same data set is shown as a log-log plot (dotted inset) together with the slopes for the PL, ASE and lasing regions. Also shown are the images of the defocused emitted beam cross section (taken at about 10μm away from the nanolaser exit aperture) for I) CW pumping and II) pulsed pumping. The appearance of the higher contrast fringes indicates increased coherence due to lasing. (b) Evolution of the emission spectra from PL to lasing.

Chapter 1, in part, is a reprint of the material as it appears in Q. Gu, J. S. Smalley, M. P. Nezhad, A. Simic, J. H. Lee, M. Katz, O. Bondarenko, B. Slutsky, A. Mizrahi, V. Lomakin and Y. Fainman, "Subwavelength semiconductor lasers for dense chip-scale integration," *Advances in Optics and Photonics,* vol. 6, pp. 1-56, 2014. The dissertation author was the primary co-researcher and author.

Chapter 2

Purcell Effect and the Evaluation of Purcell factor and Spontaneous Emission Factors

In nanolasers, the Purcell factor is often taken as a figure of merit when comparing performances of different lasers. For a cavity of quality factor Q, active region volume V_a and refractive index n, emitting at the free space wavelength λ, the Purcell factor describes the rate of spontaneous emission relative to the emission in bulk, and is expressed for a two-level system and a single-cavity mode as [7]

$$F_p \equiv \frac{\tau_{bulk}}{\tau_{cav}} = \left[\frac{3}{4\pi^2}\frac{Q}{V_a}\left(\frac{\lambda}{n}\right)^3\right]\left[\frac{\left|\boldsymbol{d}\cdot\boldsymbol{f}(\boldsymbol{r}_e)\right|^2}{\left|\boldsymbol{d}\right|^2}\right]\left[\frac{\Delta\omega_c^2}{4(\omega_e-\omega_c)^2+\Delta\omega_c^2}\right] \tag{2.1}$$

where $\boldsymbol{d}$ is the microscopic dipole, $\boldsymbol{f}(\boldsymbol{r}_e)$ describes the electric field of the mode, and ω_e, ω_c, $\Delta\ \omega_c$, are the emitter frequency, cavity frequency, and cavity full-width-at-half-maximum (FWHM), respectively. Under the assumptions that the cavity mode is resonant with the emitter transition and that the emitter is located at an anti-node of the cavity mode, the second and third bracketed terms of Equation (2.1) become unity, and the Purcell factor expression simplifies to

$$F_p = \left[\frac{3}{4\pi^2} \frac{Q}{V_a} \left(\frac{\lambda}{n} \right)^3 \right] \tag{2.2}$$

Note that these assumptions lead to the maximum attainable value of the Purcell factor. This simplified form is the one most commonly seen and used in the literature [58] to quantify the cavity-enhanced or -inhibited rate of spontaneous emission, relative to the emission in free-space. Applying Equation (2.2) to the metallo-dielectric lasers just presented, we find that the Purcell factor of the lasing mode – the mode with the highest Q, is about 40, and could be as high as 135 if the aluminum cladding is replaced with silver [35]. In other words, the rate of spontaneous emission of the InGaAsP MQWs surrounded by the metallo-dielectric cavity is about 40 times greater than the rate in the absence of the cavity.

The use of Equation (2.2) for quantifying the Purcell effect has several flaws. Firstly, rarely does the cavity mode frequency exactly match the transition frequency of the emitter. Inevitably, fabrication errors in sub-wavelength cavities lead to detuning. Additionally, dynamic effects, such as the carrier-dependent refractive index may further detune the cavity and emitter frequencies.

A more accurate method to evaluate the Purcell effect uses the emitter-field-reservoir model in the quantum theory of damping and captures effects ignored in the commonly used Purcell factor expression. Within this model, the emitter-field interaction is modified to the extent that the field mode is modified by its environment. In the ensuing section, we show that all Purcell factor expressions in the literature are recovered only in the hypothetical condition when the gain medium is replaced by a transparent medium [59]. Furthermore, under the transparent medium condition, the Purcell factor

expressions given by Equations (2.1) and (2.2) are only valid if the cavity lineshape is much wider than the gain medium inhomogeneous broadening lineshape, which is not the case in moderate- to high-Q semiconductor lasers. The general expression should therefore be obtained by considering both lineshapes. Mathematically, this effect is expressed by the convolution of the cavity lineshape, characterized by the quality factor, with both homogeneous and inhomogeneous broadening mechanisms. When this convolution is taken into account, the role of the cavity Q may be diminished, and Equations (2.1) and (2.2) may no longer adequately describe the cavity-modified spontaneous emission rate. When the formalism of the proceeding section is used to quantify the Purcell factor of the metallo-dielectric lasers just described, we find that F_p<1.

2.1 Formulation of Purcell effect for semiconductor nanolasers at room temperature

The cavity quantum electrodynamics (QED) effects caused by the interaction of the matter and electromagnetic field in sub-wavelength structures have been the subject of intense research in recent years [59-61]. The generation of coherent radiation in nanostructures has attracted considerable interest, owing both to the QED effects that emerge in small volumes, and the potential of these devices for future applications, ranging from on-chip optical communication to ultrahigh resolution and high throughput imaging/sensing/spectroscopy.

Improving Purcell factor F_p and the spontaneous emission factor β in nanolasers has also attracted significant attention, largely motivated by the quest for energy-efficient

operations in nano-scale devices. While the concept of thresholdless operation continues to be a subject of debate [15, 16], the modulation and efficiency improvements enabled by wavelength-scale cavities, which are directly related to the modification of the spontaneous emission (Purcell effect) in these cavities, is fairly well understood [8-10]. For example, with proper design, the cavity of a sub-wavelength laser may be designed such that most of the spontaneous emission is channeled into the lasing mode. In so doing, unwanted emission into non-lasing modes is mitigated, and the below-threshold efficiency is limited only by non-radiative recombination. In nano-scale lasers, enhanced emission together with a reduced number of cavity modes relative to large lasers can have significant effects, especially on sub-threshold behavior. These effects are generally desirable, as they tend to increase the utilization of spontaneous emission into the lasing mode, thus lowering the lasing threshold and increasing β. If the desired cavity mode has the highest Purcell factor amongst all cavity modes, a high β laser can be realized even in a multi-mode cavity. With this design goal in mind, it is first and foremost important to accurately evaluate the F_p of all cavity modes, taking into account the emitter environment and the semiconductor gain material properties. While the original Purcell effect evaluation was for radio frequency micro-cavities, as shown in Equation (2.2), the formal treatment of Purcell effect specific to nano-scale devices wasn't presented until the work of [10, 59, 62]. Tailored for nanolasers, these studies provide insight into the fundamental physics in the nano-cavities.

We apply the results from the non-relativistic QED treatment of 2-level systems to a 3-level laser, in which emitters are pumped from the ground state |1> to an excited state |3> and quickly decay from state |3> to a lower state |2>; the lasing transition is

between states |2> and |1> [59]. Semiconductor lasers in particular are frequently modeled in this manner, even though their underlying physics differs: state |2> describes the condition where a conduction band state is occupied and the valence band state of the same crystal momentum is vacant, while state |1> describes the condition when the conduction band state is vacant and the valence band state is occupied [63]. To describe such a system, we construct a basic model similar to that in ([64]. §9) and [65]. We suppose each emitter to interact with all modes of the cavity, but ignore direct interaction among emitters. The cavity modes, on their part, undergo damping as a result of loss at the cavity boundaries, and we model the loss as a thermal reservoir.

Loss at the cavity boundary, such as loss in a metallic mirror, or loss of energy through the mirror and its eventual conversion to heat at some remote point in space, generally satisfies the assumptions of a reservoir model: it is weak interaction with a large stochastic system that is disordered and does not retain memory of past interactions. Further, this reservoir is passive, as it does not return energy to the mode. Rather, it drains the mode energy over time and is commonly known as the zero temperature condition. The Hamiltonian describing each single emitter in this system can be expressed as

$$\hat{H} = \hat{H}_A + \hat{H}_F + \hat{H}_{AF} + \hat{H}_R + \hat{H}_{FR} \tag{2.3}$$

Where $\hat{H}_A$, $\hat{H}_F$ and $\hat{H}_R$ are the emitter, field and reservoir Hamiltonian, respectively. $\hat{H}_{AF}$ denotes interaction between the emitter and the field modes, while $\hat{H}_{FR}$ denotes interaction between the field modes and the reservoir.

We note that even if, by assumption, a given emitter does not directly interact with other emitters, the field modes still interact with all emitters present, rather than only with a single emitter. This interaction is not included in the Hamiltonian in Equation (2.3) , either explicitly or as part of the reservoir. It will be argued in Appendix A.3 that the effect of the emitter population on the field modes cannot justifiably be ignored in semiconductor lasers. However, we adopt the simplified model as a starting point to illustrate how it leads to the expressions for Purcell factor commonly found in the literature [7, 35, 66-69].

In a system where an emitter interacts with the field, and the field interacts with a thermal reservoir, the results summarized in Appendix A.1 and A.2 apply directly. The cavity Purcell factor F_{cav} is defined as the ratio of spontaneous emission in a cavity to that in free space. In the evaluation of F_{cav} in the literature, it is common to replace the vacuum free space emission probability presented in Equation (10) (Appendix A) by the emission probability of bulk material of effective index n_r, with no cavity [7, 68]. The spontaneous emission probability in the bulk material, $P^{material}_{2\to 1,|0\ldots 0\rangle}$, takes the same form as in free space, except that ε_{00} is replaced by the permittivity of the medium $\varepsilon_r = n_r^2 \varepsilon_0$ and that c is scaled down by the refractive index n_r. From Equation (10) (Appendix A) we obtain

In a solid-state system where an emitter interacts with the field, and the field interacts with a thermal reservoir, the cavity Purcell factor F_p is defined as the ratio of spontaneous emission in a cavity to that in bulk material of effective index n_r, with no cavity [7, 68]. The spontaneous emission probability in the bulk material, $P^{material}_{2\to 1,|0\ldots 0\rangle}$, takes

the same form as in free space, except that ε_{00} is replaced by the permittivity of the medium $\varepsilon_r = n_r^2 \varepsilon_0$ and that c is scaled down by the refractive index n_r. It is expressed as

$$\begin{aligned} P_{2\to 1,|0\ldots 0\rangle}^{material} &\approx \int \frac{\omega_{21}^3}{3\pi\hbar\varepsilon_r (c/n_r)^3} \tau_{coll} \left|\wp_{12}(\omega_{21})\right|^2 D(\omega_{21})\, d\omega_{21} \\ &\approx \frac{\bar{\omega}_{21}^3}{3\pi\hbar\varepsilon_r (c/n_r)^3} \tau_{coll} \left|\wp_{12}(\bar{\omega}_{21})\right|^2 \end{aligned} \tag{2.4}$$

where ω_{21} is the mode resonant frequency, $\wp_{12}(\omega_{21})$ is the dipole matrix element, and $D(\omega_{21})$ characterizes the inhomogeneity of the system. The intraband collision time, τ_{coll}, is the average time between carrier-carrier and carrier-phonon collisions, and decreases with increasing temperature [70]. In the second line of Equation (2.4), we evaluate ω_{21}^3 and $\wp_{12}(\omega_{21})$ at the center frequency $\bar{\omega}_{21}$ of the inhomogeneous broadening spectrum $D(\omega_{21})$ and pull them out of the integration, because these quantities vary relatively little over the homogenous broadening range.

In a damped cavity, the mode interacts with the reservoir. Provided that equilibrium between the mode and the reservoir is reached, we obtain the photonemission probability in steady-state,

$$\begin{aligned} &P_{2\to 1,\text{equilibrium}}^{cav} \\ &= \sum_k \frac{\omega_k}{\hbar} \left(\bar{n}(\omega_k)+1\right) \int \left|\wp_{12}(\omega_{21}) \cdot \boldsymbol{e}_k(\mathbf{r}_e)\right|^2 D(\omega_{21}) \int L_k(\omega-\omega_k) R(\omega-\omega_{21},\tau_{coll})\, d\omega d\omega_{21} \end{aligned} \tag{2.5}$$

where $R(\omega\text{-}\omega_{21},\tau_{coll})$ is the homogeneous broadening function and depends on τ_{coll}. Viewed as a function of ω, $R(\omega)$ peaks at ω_{21}, has a width on the order of $1/\tau_{coll}$, and satisfies $\int R(\omega-\omega_{21},\tau_{coll})\, d\omega = 2\pi \cdot \tau_{coll}$ [71]. The Lorentzian $L_k(\omega\text{-}\omega_k)$ in Equation (2.5)is expressed as

$$L_k(\omega-\omega_k) \equiv \frac{1}{\pi}\frac{\frac{1}{2}C_k}{\left(\frac{1}{2}C_k\right)^2+(\omega-\omega_k)^2} = \frac{2}{\pi}\cdot\frac{Q}{\omega_k}\frac{\left(\frac{1}{2}\Delta\omega_k\right)^2}{\left(\frac{1}{2}\Delta\omega_k\right)^2+(\omega-\omega_k)^2}, \quad \text{where } C_k = \Delta\omega_k \tag{2.6}$$

and the quality factor is defined as $Q \equiv \omega_k / \Delta\omega_k$, where $\Delta\omega_k$, is the FWHM of cavity lineshape. The convolution in Equation (2.5)determines the emission probability in a cavity for an inhomogeneously broadened ensemble of emitters, when the mode-reservoir equilibrium has been reached. The effect of the reservoir on the emission probability is described by $L_k(\omega-\omega_k)$, whose spectral property is described by Equation (2.6).

The Purcell factor of the cavity mode F_{cav} is then

$$\begin{aligned} F_{cav} &\equiv \frac{P^{cav}_{2\to1,\text{equilibrium}}}{P^{material}_{2\to1,|0\ldots0\rangle}} \\ &= \sum_k \frac{3\pi\varepsilon_r(c/n_r)^3}{\tau_{coll}}\frac{\omega_k}{\bar{\omega}_{21}^3}\frac{1}{\left|\boldsymbol{\wp}_{12}(\bar{\omega}_{21})\right|^2}\int\left|\boldsymbol{\wp}_{12}(\omega_{21})\cdot\boldsymbol{e}_k(\mathbf{r}_e)\right|^2 D(\omega_{21})\int L_k(\omega-\omega_k)R(\omega-\omega_{21},\tau_{coll})d\omega d\omega_{21} \\ &\approx \sum_k \frac{3\pi\varepsilon_r(c/n_r)^3}{\tau_{coll}}\frac{\omega_k}{\bar{\omega}_{21}^3}\frac{\left|\boldsymbol{\wp}_{12}(\bar{\omega}_{21})\cdot\boldsymbol{e}_k(\mathbf{r}_e)\right|^2}{\left|\boldsymbol{\wp}_{12}(\bar{\omega}_{21})\right|^2}\int D(\omega_{21})\int L_k(\omega-\omega_k)R(\omega-\omega_{21},\tau_{coll})d\omega d\omega_{21} \end{aligned} \tag{2.7}$$

The emission probability in Equation (2.5), and hence the Purcell factor in Equation (2.7), depends on the location $\mathbf{r}_e$ of the emitter. More precisely, it depends on the normalized mode field at the location of the emitter $\boldsymbol{e}_k(\mathbf{r}_e)$, as well as on the orientation of the emitter's dipole moment matrix element $\boldsymbol{\wp}_{12}(\bar{\omega}_{21})$ relative to the field. If the emitters are randomly oriented and uniformly distributed over an active region of volume V_a, the quantity $\left|\boldsymbol{\wp}_{12}(\bar{\omega}_{21})\cdot\boldsymbol{e}_k(\mathbf{r}_e)\right|^2$ is replaced by its average over all locations and orientations.

$$\left|\wp_{12}(\bar{\omega}_{21})\cdot \boldsymbol{e}_k(\mathbf{r}_e)\right|^2 \;\rightarrow\; \frac{1}{3}\left|\wp_{12}(\bar{\omega}_{21})\right|^2 \frac{1}{V_a}\int_{V_a}\left|\boldsymbol{e}_k(\mathbf{r})\right|^2 d^3\mathbf{r} \tag{2.8}$$

where the coefficient 1/3 accounts for the random emitter orientation.

In certain situations, the carrier distribution over V_a may become non-uniform. For example, in MQW structures, the carrier distributions in the well and barrier regions differ significantly. Even in bulk semiconductors, the recombination of carriers may vary spatially, with the highest rates occurring at field antinodes. This is the case if the recombination at field antinodes is so rapid that diffusion of carriers from other parts of the active volume is not fast enough to avoid depletion. Carrier depletion at field antinodes and subsequent diffusion from the nodes toward the antinodes leads to the spatial inhomogeneity of the recombination. At room temperature, the diffusion length of carriers in InGaAsP (i.e., average distance traveled before recombination) is on the order of 1-2 μm [72]. The distance between the field node and antinode in visible and near infra-red sub-wavelength semiconductor cavities, on the other hand, is usually less than 0.5 μm [34, 35]. Thus, the depletion regions would remain relatively depleted due to the finite diffusion time. Under these circumstances, Equation (2.8) should then be replaced by an appropriately weighted average.

$$\begin{aligned}
F_p &= \sum_k \frac{\pi\left(c/n_r\right)^3}{\tau_{coll}} \frac{\omega_k}{\bar{\omega}_{21}^3} \frac{1}{V_a} \left\{ \frac{\varepsilon_r \int_{V_a} \left|\mathbf{E}_k(\mathbf{r})\right|^2 d^3\mathbf{r}}{\int \left[\left(\left.\frac{\partial\left(\omega' \varepsilon_R(\mathbf{r},\omega')\right)}{\partial \omega'}\right|_{\omega'=\omega_k} + \varepsilon_R(\mathbf{r},\omega_k) \right) \mathbf{E}_k^2(\mathbf{r}) \right] d^3\mathbf{r}} \right\} \times \\
&\quad \int D(\omega_{21}) \int L_k(\omega-\omega_k) R(\omega-\omega_{21},\tau_{coll}) d\omega d\omega_{21} \\
&= \sum_k \frac{\pi\left(c/n_r\right)^3}{\tau_{coll}} \frac{\omega_k}{\bar{\omega}_{21}^3} \frac{1}{V_a} \{\Gamma_k\} \int D(\omega_{21}) \int L_k(\omega-\omega_k) R(\omega-\omega_{21},\tau_{coll}) d\omega d\omega_{21} \\
&= \sum_k F_{cav}^{(k)}
\end{aligned} \tag{2.9}$$

where Γ_k is the energy confinement factor of mode k. Equation (2.9) permits several observations. Firstly, the double integral in Equation (2.9) is the convolution of inhomogeneous broadening $D(\omega_{21})$, cavity Lorentzian $L_k(\omega-\omega_k)$, and homogeneous broadening $R(\omega-\omega_{21},\tau_{coll})$. It should be noted that although the homogenous broadening function $R(\omega)$ and the inhomogeneous broadening function $D(\omega)$ appear symmetrically in Equation (2.9), they may in principle exhibit different dynamics. In particular, rapid recombination of carriers near the mode frequency ω_k may deplete the carrier population at that frequency faster than it is replenished by intraband scattering (this phenomenon is known as "spectral hole burning"). In such cases, it could be meaningful to disaggregate the integral in $d\omega_{21}$ in Equation (2.9) and define separate Purcell factors for carriers at different frequencies ω_{21} [73]. More typically, however, especially at room temperatures, the intraband relaxation time τ_{coll} ~0.3 ps of InGaAsP is much shorter than photonemission time, and the distribution of carriers $D(\omega_{21})$ is at all times the equilibrium distribution ([74]. Appendix 6). This equilibrium distribution closely resembles the photoluminescence spectrum [75]. In semiconductor lasers utilizing bulk or MQW gain material, it is the broadest of the three convolution factors in Equation (2.9) and therefore dominates the convolution. For InGaAsP at room temperature, the FWHM of $D(\omega_{21})$ and $R(\omega-\omega_{21},\tau_{coll})$ are approximately $7\cdot10^{13}$ rad/s and $6.7\cdot10^{12}$ rad/s, respectively. $D(\omega_{21})$ dominates the convolution in Equation (2.9) as long as the cavity Q factor is above 19, which corresponds to a FWHM of $7\cdot10^{13}$ rad/s. For practical cavities, the Q factor will be significantly larger; thus diminishing the contribution of $L_k(\omega-\omega_k)$ to the resulting Purcell factor. In fact, $R(\omega-\omega_{21},\tau_{coll})$, alone, dominates $L_k(\omega-\omega_k)$ if the Q factor is greater than 200 [70, 76]. Consequently, in typical III-V semiconductor lasers with MQW or bulk gain

material, the cavity Q factor plays a negligible role in determining the spontaneous emission rate and F_p. Further, while the cavity lineshape broadens with temperature for well-confined cavity modes, the homogeneous lineshape broadens as well. Secondly, F_p may be large in small laser cavities due to its inverse proportionality to the active region volume V_a.. However, F_p is actually inversely proportional to the effective size of the mode, V_a/Γ_k , where the mode-gain overlap factor Γ_k is defined in Equation (2.9) and describes the spatial overlap between the mode and the active region. Thus, if the mode is poorly confined, $\Gamma_k << 1$, F_p will remain small, despite a small active region.

Additionally, note that the Purcell factor F_p is the sum of contributions $F_{cav}^{(k)}$ from each cavity mode present, as is the emission probability in Equation (2.5). Since the Purcell factor is positively related to the modulation speed of a device, it is an important figure of merit in designing high-speed lasers [1, 32].

2.2 Evaluation of Purcell effect in a metallo-dielectric nanolaser

In this section, we illustrate the formulation using the device demonstrated in Figure 1.6. Reiterating the key geometrical parameters: the InGaAsP MQW gain core is of height h_{core}=480 nm, and the major and minor core radii of the slightly elliptical gain (due to fabrication imperfections) are r_{major}=245 nm and r_{minor}=210 nm, respectively. The SiO_2 shield layer has thickness $\Delta \approx 200$ nm. Assuming the aluminum cladding thickness to be 70 nm (which is twice the skin depth), the height, the major and minor total diameters of this laser are 1.35 μm, 1.03 μm and 0.96 μm respectively, resulting in a laser cavity that is smaller than its emission wavelength in all three dimensions. The lasing

mode of the device, designated TE_{012}, is depicted in Figure 2.1(a). The model yields the electric field profile $\mathbf{E}_{TE012}(\mathbf{r})$, mode frequency $\omega_{TE012}=1.330\cdot10^{15}$ rad/s (λ=1416 nm), and transparent cavity Q factor Q=479, from which the Lorentzian $L_{TE012}(\omega-\omega_{TE012})$ follows via Equation (2.6). By transparent, we mean that the permittivity of the gain medium is purely real, and all losses are characterized by the imaginary part of the permittivity of the cavity metal as well as radiation out of the cavity.

The sinc-like shape of the homogeneous broadening function $R(\omega-\omega_{21},\tau_{coll})$ in Equation (10) (Appendix A) is a consequence of the assumed abrupt dephasing of emitter-field interaction due to an intraband collision at time $t=t_0+\tau_{coll}$. In reality, the dephasing is not abrupt, and collisions do not happen at precise intervals. Although more accurate lineshape models have been given [70, 77, 78], it is common to describe homogeneous broadening with a simple Lorentzian, and calibrate the intraband collision time τ_{in} so that $2/\tau_{in}$ represents the FWHM of the Lorentzian ([74]. §4.3; [79]. §5.5; [80]). The value of τ_{in} reported in this context is 0.3 ps for an InGaAsP MQW at room temperature [70, 81]. For the present purposes, the exact shape of homogeneous line broadening is not essential, and we adopt the Lorentzian approximation. The spectra $L_{TE012}(\omega)$ normalized to area 1 and $R(\omega-\omega_{21},\tau_{coll})$ normalized to area $(2\pi\tau_{coll})$ are shown in Figure 2.1(b) and Figure 2.1(c), respectively.

The origin of inhomogeneous broadening in semiconductors is the quasi-equilibrium Fermi distribution of carriers in the conduction and valence bands, which is maintained through intraband scattering [82]. In bulk material, this distribution can be estimated from the PL spectrum. Emission probabilities into the various free space modes $(\mathbf{k},\boldsymbol{\varepsilon})$ are given by the summation terms on the second line of Equation (10) (Appendix

A): they take the same form as in vacuum modeled classically, except that ε_{00} is replaced by the permittivity of the medium. The spectrum of this emission is therefore just the convolution $\int D(\omega_{21}) R(\omega - \omega_{21}, \tau_{coll}) d\omega_{21}$, after neglecting the variation in $\wp_{12}(\omega_{21})$ over the frequencies involved. $D(\omega_{21})$ can be recovered from the convolution if $R(\omega-\omega_{21},\tau_{\text{coll}})$ is known. For emission into cavity modes, we use the same emitter distribution $D(\omega_{21})$ as that used for emission into free-space modes. This follows from the assumption that the carrier recombination rate (rate of level transitions) is smaller than the intraband relaxation rate, $1/\tau_{\text{coll}}$, which was used to justify the use of Equation (9) (Appendix A). A necessary consequence of this assumption is that spectral hole burning will not occur [9, 81]. In the Purcell factor evaluation presented in this section, we use the PL spectrum of the material without the presence of a cavity either measured at low pump powers or as provided by OEpic Semiconductor Inc., who grew the material. The distribution of $D(\omega_{21})$ is obtained from the PL spectra, which are plotted in Figure 2.1(d).

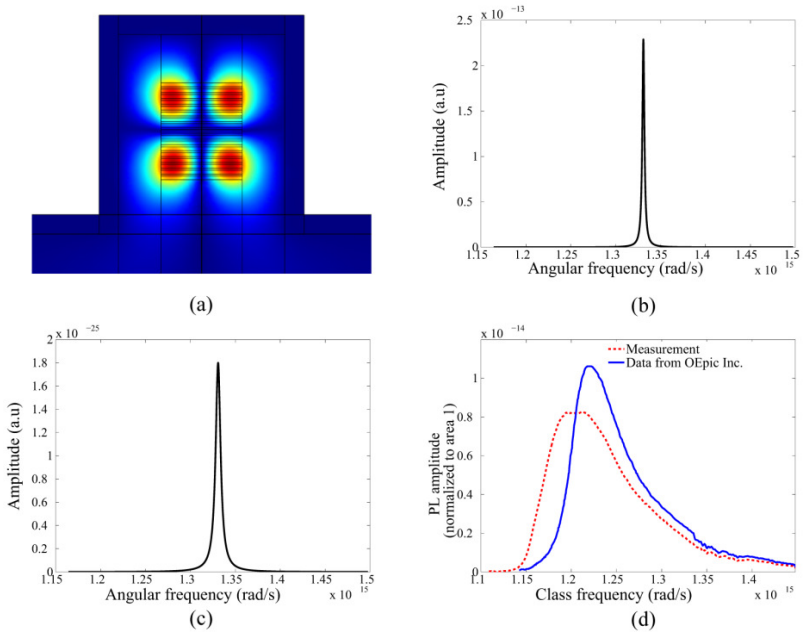

Figure 2.1: (a) The lasing mode's electric field profile and the three spectra in the evaluation of the Purcell factor: (b) cavity lineshape, (c) homogeneous broadening lineshape and (d) PL spectra. Dashed red: measured at low pump powers, and solid blue: datasheet provided by OEpic Inc.

Knowledge of the cavity Lorentzian L_{TE012}, the homogeneous broadening function $R(\omega\text{-}\omega_{21},\tau_{\mathrm{coll}})$, the inhomogeneous distribution $D(\omega_{21})$ and the field profile $\mathbf{E}_{\mathrm{TE012}}(\mathbf{r})$ allows us to evaluate the summation term $F_{cav}^{(TE012)}$ in Equation (2.9). Table 2.1 lists the values of $F_{cav}^{(TE012)}$ (sometimes thought of as "single mode Purcell factor") if material dispersion is neglected, for the following cases [59]: (i) assuming an inhomogeneously broadened gain medium, by evaluating Equation (2.9); (ii) ignoring inhomogeneous broadening and assuming instead that all emitters are on exact resonance with the cavity mode, i.e., $D(\omega) = \delta(\omega\text{-}\omega_{\mathrm{TE012}})$; (iii) following the method used in the supplementary material of [35], where both the inhomogeneous and the homogeneous broadening were neglected, i.e., $D(\omega)=\delta(\omega\text{-}\omega_{\mathrm{TE012}})$ and $R(\omega\text{-}\omega_{21},\tau_{\mathrm{coll}})=(2\pi\tau_{\mathrm{coll}})\cdot\delta(\omega\text{-}\omega_{\mathrm{TE012}})$. Both

homogeneous and inhomogeneous broadenings lower the spontaneous emission rate into mode TE_{012}, because, when broadened, not all emitters are on resonance with the TE_{012} mode frequency. Further, spontaneous emission from emitters with transition frequencies near the mode resonance in the presence of intraband scattering is less enhanced than that from the same emitters in the absence of intraband scattering. Approximate calculations that do not account for the broadening, such as in [35], may therefore dramatically over-estimate the emission rate and the Purcell factor.

Table 2.1: Evaluation of the Purcell factor $F_{cav}^{(TE012)}$ using different methods

Inhomogeneously and homogeneously broadened	Homogeneously broadened	Unbroadened
0.170 (Measurement) 0.215 (OEpic. Inc)	5.175	8.79

Because greater emission into the mode that would ultimately lase is generally desirable as it helps utilize the carriers more efficiently, whereas emission into other modes is wasteful. From this point of view, therefore, the appropriate figure of merit is not the Purcell factor F_{cav} but the spontaneous emission factor β,

$$\beta = \frac{F_{cav}^{(1)}}{\sum_k F_{cav}^{(k)}} \tag{2.10}$$

where the lasing mode is indicated by the index k=1, and the summation is over all modes k, including cavity modes and modes radiating out of the cavity into free space. The spontaneous emission factor is brought closer to its theoretical limit β=1 when one summation term in Equation (2.9) is increased and other terms are suppressed, for example by eliminating unwanted cavity modes [14].

To compute the spontaneous emission factor β in Equation (2.10), it is necessary to evaluate the total spontaneous emission rates in all modes *k*, including cavity modes and modes radiating out of the cavity into free space. The Q factors of the radiating modes are low, but their number is large, making a direct summation of terms in Equation (2.9) difficult. Alternative estimation methods exist, based on the formal equivalence between spontaneous emission and the radiation of a classical point dipole. For a cavity such as that of [35], which is not strongly radiating, it may be helpful to obtain the upper bound on β by including in the denominator of Equation (2.10) only the cavity modes thought to contribute most to spontaneous emission.

Figure 2.2 depicts the electric field distribution and $F_{cav}^{(k)}$ of all the cavity modes with Q factors greater than 20, and whose resonance wavelengths fall within the material PL spectrum of 1300-1670 nm. Limiting the summation in the denominator of Equation (2.10) to these 5 modes yields the upper bound β_{max}=0.359 using measured PL, and β_{max}=0.377 using PL by OEpic Inc. We note that the geometry of this device is not optimized for maximizing β in the metallo-dielectric cavity design.

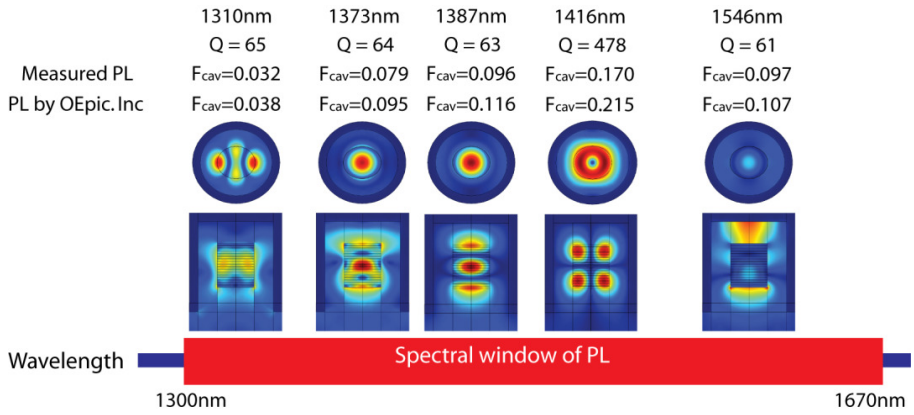

Figure 2.2: Simulated mode distribution of all modes that falls within the spectral window of PL and have cavity Q>20. Also shown are Purcell factors for each mode, F_{cav}, calculated using two different sources of PL spectra.

2.3 Dependence of spontaneous emission factor on temperature

The spontaneous emission factor β depends upon the resonant frequency of the lasing mode and the spectral spacing between cavity modes, in addition to the spontaneous emission spectrum of the material. All of these factors depend upon the device temperature, hence making the spontaneous emission factor temperature dependent. The resonant frequencies of the cavity vary with temperature due to the thermo-optic effect, or the temperature dependence of the real part of the active region permittivity. This is generally a weak effect, in comparison to the temperature dependence of the imaginary part of the active region permittivity, which determines the material emission spectrum under different pumping levels. The emission spectrum is a strong function of temperature due to the temperature dependence of the bandgap energy and the Fermi-Dirac distribution functions. A natural question in the design of sub-wavelength lasers is the following: For a selected material system and cavity geometry,

how sensitive is β to temperature changes? Such temperature changes could be either dynamic, occurring as the laser operates, or static, representing different well-controlled experimental conditions. A common experimental technique for determining β requires temperatures as low as 4.5K for elimination of non-radiative recombination [14]. Understanding the dependence of β on temperature is essential to predicting whether a laser that exhibits near unity-β at such low temperatures will indeed exhibit similar β near room-temperature. We now briefly summarize the process by which the sensitivity of β to temperature in subwavelength semiconductor lasers may be determined. A complete analysis and discussion of this technique may be found in [17].

The dependence of β on temperature may be seen as a consequence of the temperature dependence of the Purcell factor of Appendix A.2. Writing F_{cav} of Equation (2.9) as an explicit function of temperature we have,

$$F_{cav}^{(k)}(T) = \frac{\pi(c/n_r)^3}{\tau_{coll}} \frac{\omega_k(T)}{\bar{\omega}_{21}^3} \frac{\Gamma_k}{V_a} \int \mathrm{Z}_{SP}(\omega_{21},T) \int L(\omega-\omega_k,T) R(\omega-\omega_{21},\tau_{coll},T) d\omega d\omega_{21} \quad (2.11)$$

In Equation (2.11), $\mathrm{Z_{SP}}$ is the rate of spontaneous emission in the absence of the cavity, calculated according to the semiclassical treatment of Ref [74]. The maximum spontaneous emission factor as a function of temperature then becomes

$$\beta_{\max}(T) = \frac{F_{cav}^{\text{lasing}}(T)}{\sum_k F_{cav}^{(k)}(T)} \quad (2.12)$$

The evaluation of Equations (2.11) and (2.12) requires knowledge of the transparent carrier densities for all cavity mode wavelengths. These can be found by plotting the temperature dependent material gain spectra and identifying when the gain changes from positive- to negative-valued. The obtained transparent carrier densities for a

10nm 1.6Q/1.3Q QW are shown in Figure 2.3(a), corresponding to the resonant wavelengths of the TE_{011} mode at various temperatures. The TE_{011} mode is the dominant mode in a cavity similar to that discussed in Section 2.2, but with core and total radii of 250 nm and 350 nm, respectively. To obtain β(T) for this laser, we evaluate Equations (2.11) and (2.12) at the appropriate carrier densities. The result is shown in Figure 2.3 (b). Cases of both positive and effectively negative thermo-optic coefficients are shown in Figure 2.3 [17].

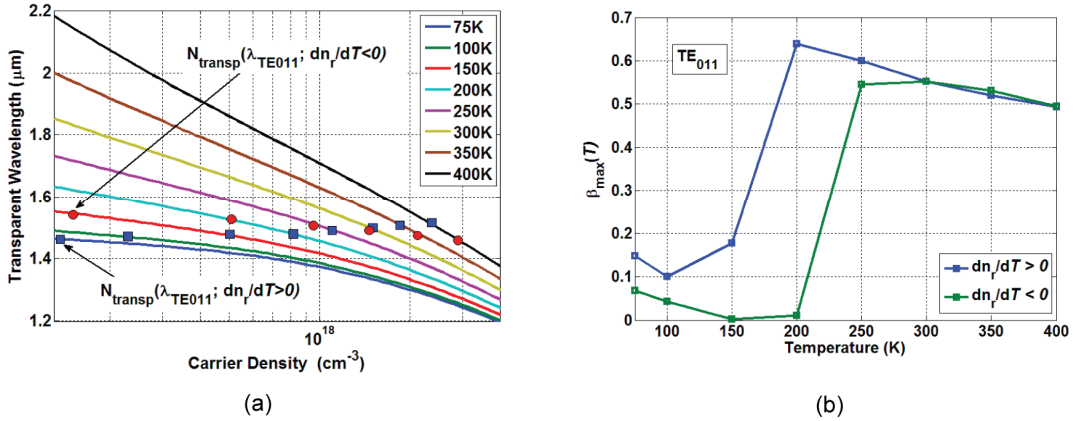

Figure 2.3: (a) Transparent wavelength versus carrier density and (b) Spontaneous emission factor versus temperature for a 10 nm MQW-InGaAsP-metal-clad nanolaser similar to that of Section 2, but with 250 nm and 350 nm core and total radii, respectively. The cases of positive and effectively negative thermo-optic coefficients are denoted by $dn_r/dT>0$ and $dn_r/dT<0$, respectively.

The major effect of the temperature in the calculation of $\beta_{max}(T)$ is to shift the gain and spontaneous emission spectra significantly. The effect of the temperature on the real parts of the cladding and semiconductor permittivities is not as dramatic. The rapid rise in β_{max} with temperature and the subsequent broad maximum was similarly observed for VCSELs and microcavitiy [83, 84]. However, the critical temperature at which β decreases sharply appears lower for a subwavelength cavity. In this sense, the analysis

demonstrates the rather non-intuitive result that β of a subwavelength cavity may be more robust to temperature variation than that of a larger laser. This appears to be a direct consequence of the sparse mode density in the cavity that we have considered. However, the analysis also shows that a laser with high-β near room-temperature may have significantly lower β at low temperatures, and vice versa. Therefore, experimental measurements of β must bear the temperature dependence in mind.

With knowledge of the temperature dependence of the gain material, cavity mode and β, it becomes possible to evaluate nanolaser designs for their temperature performance, as well as to make modifications to improve thermal management, and evaluate the effects of these modifications. An analysis of a device's temperature performance requires calculation of its self-heating, such as the simulation performed by Liu et al. [85] for a CW optically pumped device, or by Gu et al. [38] for a CW electrically pumped device. This self-heating, tempered by the nanolaser's ability to dissipate heat, can cause a significant temperature rise in the semiconductor, which in turn affects material parameters and therefore the nanolaser's QED effects as well as optical behavior. Analysis of the nanolaser's performance, therefore, should take place at the actual internal operating temperature, rather than at the ambient temperature. With the ability to do this interdependent analysis, it is then possible to evaluate the effects of design modifications that reduce the amount of heat generated, or increase the nanolaser's ability to dissipate heat.

2.4 Discussion

Because a common technique for the determination of F_p and β uses curve-fitting of experimental light−light curves at low temperatures in the rate equation analysis, one can more accurately analyze experimental light−light curves with better understanding of the temperature dependence of F_p and β. The analysis can also serve as an important tool for optimizing the cavity-material system to yield maximum or minimum β**,** depending on the application [86]. Although we focused on analyzing an optically pumped metal-clad nanolaser with MQW gain, the analysis may be applied to an arbitrary semiconductor nanolaser geometry. It may also be applied to the construction of devices with active control of the temperature. If it were possible to tune the temperature of the device reliably, the high and low β regions of the device might be used as a mechanism for switching between single-mode and multi-mode outputs, even before the onset of lasing.

Chapter 2, in part, is a reprint of the material as it appears in Q. Gu, B. Slutsky, F. Vallini, J. S. Smalley, M. P. Nezhad, N. C. Frateschi and Y. Fainman, "Purcell effect in sub-wavelength semiconductor lasers," *Opt. Express,* vol. 21, pp. 15603-15617, 2013. and Q. Gu, J. S. Smalley, M. P. Nezhad, A. Simic, J. H. Lee, M. Katz, O. Bondarenko, B. Slutsky, A. Mizrahi, V. Lomakin and Y. Fainman, "Subwavelength semiconductor lasers for dense chip-scale integration," *Advances in Optics and Photonics,* vol. 6, pp. 1-56, 2014. The dissertation author was the primary co-researcher and author.

Chapter 3
Active Medium for Semiconductor Nanolasers: MQW vs. Bulk Gain

Apart from the fundamental study of quantum effects in nanolasers, such as those discussed in Chapter 2, the ability to produce small, high-density, high-efficiency nanolasers also have wide-ranging technological applications. Nanolasers will be useful for ultrahigh resolution and high-throughput imaging, sensing and spectroscopy systems, all with low power consumption and with the coherent light source integrated with the sensor, reducing the fabrication cost of such devices. In optical telecommunications, semiconductor nanolasers can produce on-chip high density optical interconnects with very low power consumption [87]. These nanolasers will need to be electrically pumped, and will need to have small footprints [13]. To achieve this, two major issues have to be considered in nanolaser design: the architecture for photonic confinement and the choice of material for the optical gain region.

The first important aspect of design is to choose the method of photonic confinement for the optical cavity. In Chapter 1, we overviewed recent efforts towards high mode confinement and low threshold gain in the field of nanolasers. Using the metallo-dielectric nanolaser as an example, we saw that by optimizing the thickness of

the dielectric shield layer, one can decrease the metal-loss by reducing the optical mode overlap with the metal and, at the same time, reduces the radiation losses [35].

The second important aspect of design is the electron confinement and material choice for the active region of the device. While we have used optically pumped nanolasers to study fundamental light-matter interaction phenomena on the quantum level in Chapter 2, electrically pumped devices are necessary for insertion into chip-scale circuits. Therefore, in designing for the active region material, we consider electrically pumped metallo-dielectric nanolasers. We note that this design consideration can be applied to optically pumped nanolasers too.

To the best our knowledge, electrically pumped metallo-dielectric resonators have employed bulk alloy $In_{0.53}Ga_{0.47}As$ material as the active medium inside a double heterostrucure for current injection and electron confinement. These are the only demonstrated metallo-dielectric semiconductor electrically pumped nanolasers, operating from cryogenic to room temperatures. Unfortunately, the threshold current, the required material gain and self-heating effects are still high and need to be reduced for an efficient operating device. A frequent suggestion found in the literature is to employ quantum wells (QW's) as the gain media, which has been successfully employed in convential semiconductor lasers. The interest on QW material relies on their lower transparent carrier density in comparison with bulk materials, which allows lower threshold currents due to the higher material gain and power consumption. Furthermore, quantum well engineering allows the tailoring of the emission wavelength which is used to adjust the laser wavelength to the several available wavelength division multiplexing (WDM) channels. Another possibility of using QW's is to generate coherent emission of light

through the decay of exciton-polaritons, which is called an inversionless laser and have a very small threshold current compared to a photon laser [43]. Unfortunately such devices operate at cryogenic temperatures or with a large magnetic field applied to them due to the very small binding energy of the excitons [45, 46].

3.1 Current injection in semiconductor nanolasers

Besides all the above-mentioned advantages of using QW as gain media, these structures present some disadvantages that can explain why electrically pumped metallo-dielectric nanolasers with QW active region have not been demonstrated yet. First, the confinement factor in MQW gain media is very low in comparison with a bulk gain media, which makes the modal threshold gain to be lower for the bulk. Second, not yet widely discussed in the nanolaser literature, is the leakage of carriers to the barriers. As the photonic radiation losses become very high and the gain medium size diminishes, such as in the case of nanolasers, very high injected carrier density is necessary to achieve a material gain to overcome such radiation losses. This regime of high excitation leads to a large separation between the electron and hole quasi-Fermi levels. This, in turn, leads to barrier pumping as well as the saturation of the carrier concentration and of the material gain within the QW [88]. Finally, one could argue that barrier population can be prevented or minimized by increasing the barrier height without changing the well height. However, in order to achieve the threshold material gain, structures with MQW are necessary. The taller the barriers, the more inhomogeneous the population in the wells becomes. Inhomogeneous pumping is extremely detrimental for achieving the threshold condition.

In order to qualitatively understand the dependence of the carrier population on current injection for the bulk and for the MQW active region, we have simulated the band diagram of both structures when unbiased, under small bias and large bias. In all cases, the gain medium is placed within a double heterostructure P-i-N diode. The structure is as follows: semi-insulating InP substrate, 1 μm p^+-$In_{0.733}Ga_{0.227}As_{0.493}P_{0.507}$ layer, 1 μm p-InP layer, 10 quantum wells consisting of 100 Å $In_{0.56}Ga_{0.44}As_{0.938}P_{0.062}$ (E_g=0.761 eV) wells within 200 Å $In_{0.734}Ga_{0.266}As_{0.571}P_{0.429}$ (E_g=0.954 eV) barriers, 0.2 μm n-InP layer and a 0.125 μm n^--$In_{0.53}Ga_{0.47}As$ layer. The highly doped layers are used for the ohmic contact formation, the doped InP layers are the cladding layers, and the MQW layers form the active region. In the case of bulk active region, we considered an $In_{0.53}Ga_{0.47}As$ layer replacing the MQW. All layers are lattice matched to InP and the active region thickness is 400 nm for both cases. The band diagram simulations were performed using the software SILVACO which solves self-consistently the Poisson equation, the Schrodinger equation and the carrier transport equations. Figure 3.1(a) and (c) show the unbiased band diagrams for the MQW and the bulk gain structures, respectively. Considering only the semiconductor layers, we define the material width in the simulation such that the gain medium volume is ~0.23 μm^3, which is on the same order of typical nanolaser cavities [37]. E_{fc} and E_{fv} are the quasi-Fermi levels for the electrons and for the holes, respectively. Figure 3.1(b) and (d) show the biased band diagrams for the MQW and the bulk gain structures, respectively. Two biases conditions are displayed: the dashed red line is obtained under a low bias (around 0.8 V) and the blue dashed line is obtained under a higher bias condition (around 1.0 V). For the bulk gain structure we observe the band filling effect since the E_{fc} and E_{fv} separation shifts the band edges

towards shorter wavelengths. On the other hand, for the MQW gain structures, the barriers become populated in the high injection regime. As a result, the increase of the well carrier density with bias becomes smaller and eventually stops. Under optical pumping condition, the same problem exists since carrier density within the QW is univocally dependent upon the quasi-Fermi level separation. However, without the self heating effects of current injection, lower gain threshold requirement may permit lasing at the well wavelength. In fact, optically pumped MQW nanolasers have already been demonstrated rather extensively [14, 26, 27, 35].

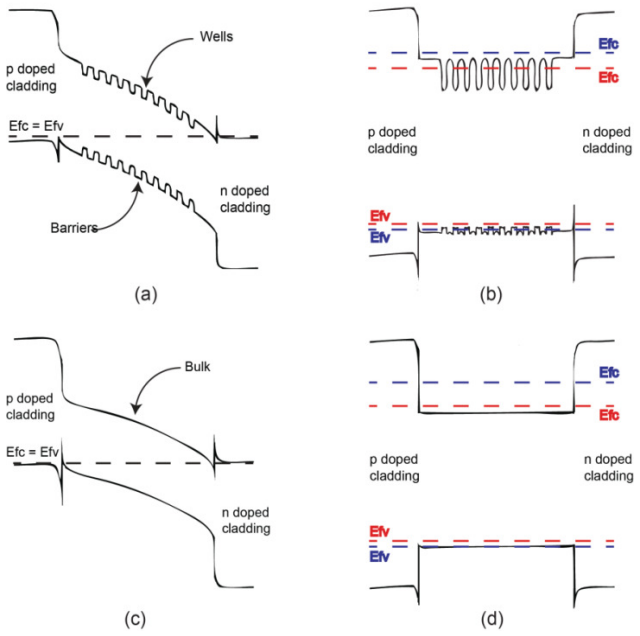

Figure 3.1: Simulated band diagrams with the electrons and holes quasi-Fermi levels (E_{fc} and E_{fv}) of a (a) unbiased MQW heterostructure; (b) forward biased MQW heterostructure; (c) unbiased bulk heterostructure and (d) forward biased bulk heterostructure. Red dashed lines are for 0.8 V bias and blue dashed lines are for 1.0 V bias.

3.2 Optical cavity and material gain optimization

Several experimentally demonstrated and/or theoretically proposed electrically pumped metallo-dielectric nanolasers [34, 36-38, 89]. Because the analysis comparing MQW and bulk gain media should not depend upon a particular cavity design, rather than using the optically pumped cavity design example explored in the preceding chapters, we have chosen to explore the electrically pumped nanopatch design, a metallo-dielectric resonator proposed by Ding et. al [89]. The nanopatch laser is a strong candidate for planar integration with silicon based photonics and due to its high spontaneous emission β-factor. A schematic drawing of the device is shown in Figure 3.2. The MQW (bulk) gain device consists of a 190 (185) nm radius cylindrical gain core held by two 150 (185) nm radius InP cylindrical plugs. One should notice that the core and plug have the same radius for the optimized bulk gain resonator, i.e., there is no undercut in this case. The optimization is based on the optical confinement and carrier injection as discussed in the next sub-sections. A 200 nm thick silicon dioxide conformal layer is deposited on the plugs and core. The entire structure is surrounded by 300 nm of silver and covered by a 300 nm layer of gold as shown in Figure 3.2. The SiO_2 shield layer reduces the overlap between the optical mode and the metal, and the silver and gold thicknesses are designed such that they can act as an antenna to couple light to an adjacent waveguide [89]. The total height of the structure is 1550 nm.

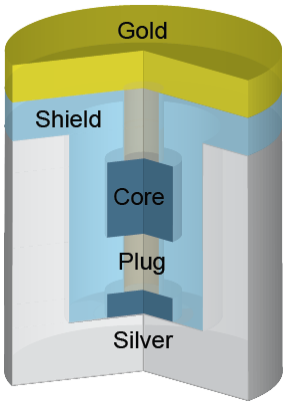

Figure 3.2: Schematics of a nanopatch laser resonator.

The optimization of core and plug radii for each case was performed as follows [90]: we varied both radii from 100 nm to 200 nm minimizing the calculated threshold current. The minimum radius is limited by the resolution of fabrication, while the maximum radius is limited by the onset of degenerate multimode behavior in the 1550 nm emission range.

For modal calculation, commerical software COMSOL Multiphysics was used. As the core and the plug radii change, the resonant mode wavelength, the confinement factor Γ and quality factor Q change. The inset of Figure 3.3(a) titled QW and the inset of Figure 3.3(b) titled Bulk #1 contains the spatial distribution and the modal properties for the first order confined optical mode. For both cases the resonant mode is the axial symmetric TE_{011}.

To calculate the threshold current, sssuming metallic and radiation losses, we can then obtain the lasing threshold gain g_{th} as a function of the mode wavelength, as shown by the green curves in Figure 3.3(a) and (b) for MQW and bulk gain, respectively. Since the resonant wavelength range is different for each structure, the range of calculation was increased to facilitate the comparison between the two structures. For each core and plug

radius in our range, we calculate the material gain for the resulting structure (as described in the following sub-section), and then use our calculated gain versus carrier concentration relation to calculate threshold carrier density to reach g_{th} for each structure. Considering the emission within the range of 1500 to 1610 nm one searches for the minimum threshold current. To calculate the threshold current necessary to populate the active gain medium with the threshold carrier density, we use the software SILVACO, which self-consistently solves the Poisson equation, the Schrodinger equation, and the carrier transport equations considering Fermi Dirac statistics. The threshold current sets the desired optimum core and plug radii with the respective resonance wavelengths shown by vertical dashed red lines in Figure 3.3(a), at 1562.7 nm, and Figure 3.3(b), at 1602.1 nm.

To calculate the material gain for both types of gain media, the reduced effective mass approach, Fermi Dirac statistics and intraband scattering broadening are employed. In the case of the MQW medium, we include both the bound (energy lower than the barrier height) and unbound (energy higher than the barrier height) electrons [91] ([92]. §9). Due to the shallow height of the barrier, there is only one quantized energy level for the electrons in the conduction band and three quantized levels for the holes in the valence band: two for the heavy hole bands and one for the light hole band. Since the transition from the conduction band level to the second heavy hole level is not allowed, and the density of states for the light hole is small, only the transition from the conduction band level to the first heavy hole level was considered in the calculations. Also, the barrier material optical gain was calculated considering the region as a bulk.

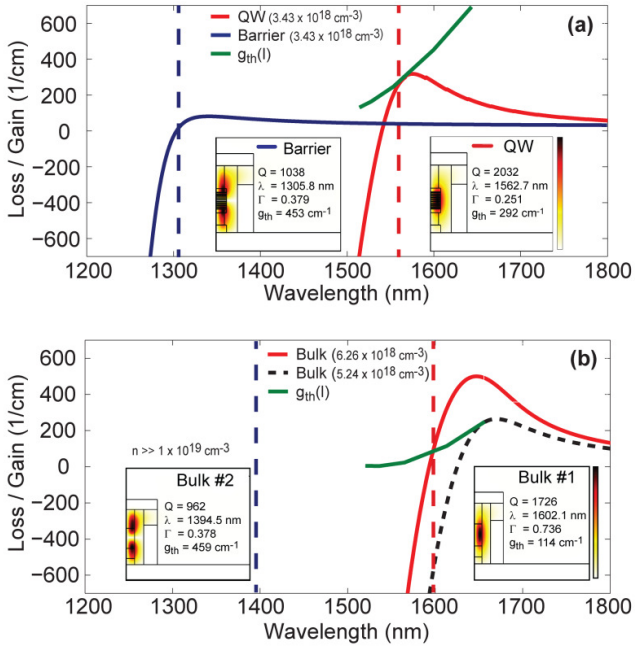

Figure 3.3: Material gain dependence with wavelength for (a) an InGaAsP MQW structure (red) and an InGaAsP barrier (blue) at the threshold carrier density for the first order mode and (b) an InGaAsP bulk material for two different carrier densities, one at the threshold (red) and other for an optimized cavity (black dashed line). The green curves are the threshold gain dependence with resonance wavelength. Insets: possible confined optical modes and their properties. The thermal color scale indicates the normalized power from 0 (white) to 1 (black). The rightmost inset of Figure 3.3(a) shows the fundamental mode (well mode) with a quality factor (Q) of 2032, resonance wavelength of 1562.7 nm, a confinement factor (Γ) of 0.251 and a threshold gain (g_{th}) of 292 cm^{-1}. The leftmost inset of Figure 3.3(a) shows the second longitudinal mode (along the height direction), (barrier mode), with a Q of 1038, resonance wavelength of 1305.8 nm, a Γ of 0.379 and a g_{th} of 453 cm^{-1}. The insets of Figure 3.3(b) also contain the first order mode and second longitudinal order mode for the bulk core media. The first mode, labeled Bulk #1, has a Q of 1726, resonance wavelength of 1602.1 nm, a Γ of 0.736 and a g_{th} of 114 cm^{-1}. The second order mode, labeled Bulk #2, has a Q of 962, resonance wavelength of 1394.5 nm, a Γ of 0.378 and a g_{th} of 459 cm^{-1}.

The red curves in Figure 3.3 are the calculated material gain at the threshold carrier density for the first order mode. We observe that in Figure 3.3(a), for the MQW, the maximum gain matches the threshold gain at the resonance wavelength. This is possible since one can optimize the well/barrier composition; a definite advantage of using MQW design. For the bulk case in Figure 3.3(b) we notice that the same

optimization is impossible unless the dimensions are changed beyond the established radii limits, causing a shift in resonance wavelengths, as shown by the black dashed line on Figure 3.3(b), or one must use a quaternary (InGaAsP) alloy. In our study, we will keep the ternary alloy for the bulk gain media, even though it is not optimized. Therefore, in terms of gain/resonance overlap, the MQW material is more optimized for the nanopatch laser. A final important remark about the cavity design is the fact that it is very difficult to avoid the presence of high order modes with resonances near 1300 nm. The high order mode (second longitudinal mode), here called the barrier mode, shown in the inset of Figure 3.3(a), with a Q of 1038, has resonance wavelength of 1305.8 nm, a Γ of 0.379 and a g_{th} of 453 cm^{-1} for the MQW gain core. The second order mode for the bulk gain core, Bulk #2 on the inset of Figure 3.3(b), has a Q of 962, resonance wavelength of 1394.5 nm, a Γ of 0.378 and a g_{th} of 459 cm^{-1}. The difference between the two cases is that material gain may be available for the barrier mode for the MQW core when the quasi-Fermi level difference allows barrier population. The blue curve in Figure 3.3(a) shows the calculated material gain of the barrier, considering the media as a bulk, at the threshold carrier density of the well mode. In fact, this second order mode is undesired but inherent to the cavity design. Since any modification to the design to prevent this mode would affect the fundamental mode which is already fully optimized, no optimization was performed to minimize the effect of the second order mode. Therefore, with the high carrier density needed for lasing at the 1560 nm resonance, a competition with this second order mode may cause yet more saturation for the well emission. This does not mean that the second order mode will reach its threshold; it means that the injected carriers will start populating the barrier together with the well levels. Since the

density of states in the barrier (considered here as a bulk material) is higher than that in the well levels, the tendency is a saturation of carrier density in the wells. Even if there was no gain in the barrier the same saturation effect would be present since the barriers still consume carriers. Notice in Figure 3.3(b) that no material gain is available in the bulk gain core near the second order resonance, at least at the moderately high carrier density shown. Also, the rightmost inset in Figure 3.3(b) shows that the bulk design has a higher Γ compared with the MQW design.

In the following section, using the laser rate equations, we will compare the performance of the MQW gain structure, which has the advantage of being fully optimized, with the bulk gain structure, which has the advantage of having a higher confinement factor.

3.3 Reservoir model for semiconductor lasers

Reisinger *et. al.* [93] comment that while quantum well lasers have very small threshold currents and are almost insensitive to the cavity length for long lasers, quantum wells are not suitable for very short lasers. In short nanolasers, leakage of carriers and other two non-radiative processes inherent to the materials: Auger recombination and recombination from L valleys are prominent, which are detrimental to device performance [93]. The effects of carrier leakage was introduced to the threshold current analysis to explain the sharp rise of the threshold current in very short quantum well lasers [94-96]. In this context, the carriers have enough energy to reach the barriers layers and be swept away by drift or diffusion, while carriers also decay by spontaneous emission or stimulated emission, if the cavity losses allow. Furthermore, the threshold

gain for such small lasers leads to a dramatic increase in threshold current, and consequently, a collapse of the quantum efficiency. Lastly, if the wells allow, while the current increase, it is possible to have other transitions between the higher quantized levels, which means an emission wavelength shift. As already known, such wavelength shift can be detrimental for nanolasers, which have a very specific cavity design with a very sensitive resonant wavelength.

In our model, we include the carrier leakage to the barriers. The effects of barrier pumping on lasing were analyzed employing the reservoir model proposed by Rideout *et al.* [88]. In this model, we consider two reservoirs for carriers: one for the confined electrons (in the well) and the other for the unconfined electrons (in the barrier). These two reservoirs can exchange carriers with time constants τ_{cap} and τ_{esc}, for capture and escape respectively. The capture time describes electrons' displacement from the barrier to the well while the escape time is related to the opposite situation. These characteristic times are described by phonon-assisted quantum transitions, tunneling (which depends on effective barrier height and width as well as on the applied electric field), thermionic emission (which depends strongly on the effective barrier height), and classical carrier diffusion in each region [88, 97]. Although the capture and escape dynamics depend on the effective barrier height, which in term depends upon the quasi-Fermi levels, we will use average constant capture and escape times, as employed by other authors [97, 98] ([99]. §5). The full description of the dynamics would be needed to describe the modulation response of the device; however, this is beyond the scope of this work.

To illustrate the idea of considering an interchange of carriers we use Figure 3.4 that shows a simple reservoir schematic that can be useful to illustrate the role of the

barrier in saturating the quantum well emission. In Figure 3.4, the left reservoir is the QW and the right reservoir is the barrier. Both reservoirs are connected and can be filled with carriers (in blue) until the pump-dependent Fermi level (Δμ, shown as a green dashed line) is reached. In Figure 3.4(a), the QW starts to be filled before the barrier does, until the Fermi level Δμ1 is reached, since the QW has a narrower band gap than the barrier. When the pump is increased to Fermi level Δμ2, above the interconnection region between the two reservoirs, the barrier also starts to be populated, as depicted in Figure 3.4(b). Because of the connection, the density of carriers into the wells stops increasing while there are empty states for the carriers in the barrier, as shown in Figure 3.4(c). Once both reservoirs are filled to the interconnection level, they start increase together until they reach the Fermi level Δμ3, as shown in Figure 3.4(d). The limit for filling the reservoir is the threshold condition and carrier clamping with consequent material gain clamping. The threshold condition in the Figure 3.4 is represented by red and blue dashed lines, for the well and for the barrier, respectively. This model is suitable to describe semiconductor nanolasers, where the lasing threshold gain is so high that this interconnection region is reached and the barrier is populated. It does not matter whether the barrier material is in the absorbing or amplifying regime, since it is sharing carriers with the well. This is the regime we have been described in this manuscript.

For larger lasers, the threshold gain (dashed red line) is expected to be much lower and will lye below the interconnection region of our model, as shown in Figure 3.4(e), enabling lasing before the barrier starts to be populated. If the reservoir interconnection is far below the threshold gain for the first mode, as depicted in Figure 3.4(f), only spontaneous emission will occur. Obviously, there are other effects that are

not taken into account in this simple schematic. For example, the carriers are injected into the wells through the barriers; as a result, we expect a small increase in the barrier carrier density with pumping before the Fermi level reaches the interconnection region between the reservoirs.

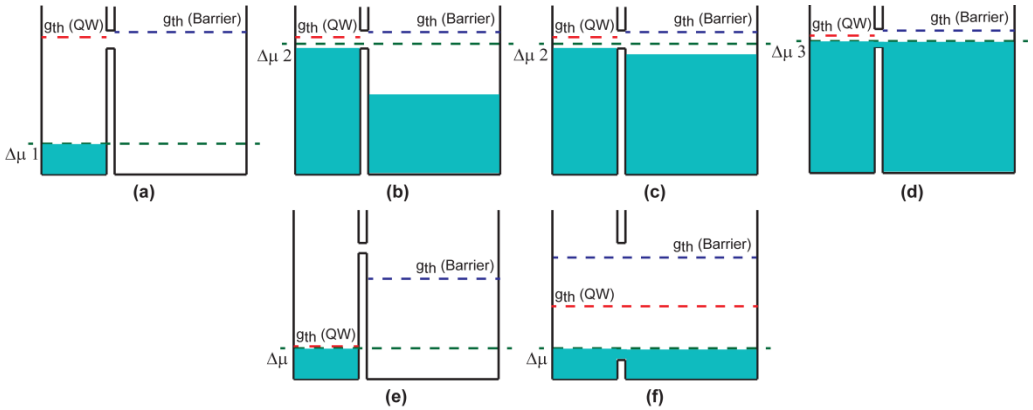

Figure 3.4: Reservoir schematics to illustrate the interchange of carriers between the well and barrier. The red and blue dashed lines represents the threshold gain for the well and the barrier mode, respectively, while the green dashed line represents the pumping level Δμ that increases from (a) to (d). The lower Figs. show a reservoir where the threshold gain for the first mode is (e) lower and (f) much higher than the reservoir interconnection.

It is hard to predict the cavity dimensions where the carrier leakage starts to be detrimental for the performance of a nanolaser. It is well know that for larger MQW conventional lasers the threshold current starts to increase for cavities tens of μm's long [93]. But such studies have never been done in the case of nanolasers, so the authors suggest to include the muti-carrier equations into the analyze of metallo-dielectric semiconductor nanolaser performance.

3.4 Laser rate equation analysis with the reservoir model

In order to apply the reservoir model described in Section 3.3, we construct a photonic rate equation at the well wavelength, a photonic rate equation at the barrier wavelength, a carrier rate equation for the well and a carrier rate equation for the barrier. For the MQW structure, we lump all barrier regions together. Assuming uniform carrier distribution in the wells as did in the barriers, it is also possible to lump the well regions since the calculated gain is for the entire set of 10 wells. The rate equations are

$$\frac{dn_{barrier}}{dt} = \frac{I}{qV_{barrier}} - R_{NR} - R_{barrier} - \frac{n_{barrier}}{\tau_{cap}} + \frac{n_{wells}}{\tau_{esc}}\left(\frac{V_{wells}}{V_{barrier}}\right) - v_g p_{barrier} g_{barrier} \quad (3.1)$$

$$\frac{dn_{wells}}{dt} = \frac{n_{barrier}}{\tau_{cap}}\left(\frac{V_{barrier}}{V_{wells}}\right) - R_{NR} - R_{wells} - \frac{n_{wells}}{\tau_{esc}} - v_g p_{wells} g_{wells} \quad (3.2)$$

$$\frac{dp_{barrier}}{dt} = \Gamma_2 \beta_2 R_{barrier} + \left[\Gamma_2 v_g g_{barrier} - \frac{\omega_2}{Q_2}\right] p_{barrier} \quad (3.3)$$

$$\frac{dp_{wells}}{dt} = \Gamma_1 \beta_1 R_{wells} + \left[\Gamma_1 v_g g_{wells} - \frac{\omega_1}{Q_1}\right] p_{wells} \quad (3.4)$$

where $n_{barrier}$ and n_{wells} are the lumped carrier densities in the barriers and in the wells respectively, I is the injection current, q is the electron charge, $V_{barrier}$ and V_{wells} are the volume for the barrier and wells region respectively, R_{NR} is the non-radiative recombination rate, $R_{barrier}$ is the spontaneous emission at the barrier, v_g is the group velocity, $p_{barrier}$ and p_{wells} are the photon density at the barrier and at the wells respectively, $g_{barrier}$ and g_{wells} are the material gain at the barrier and at the wells, R_{wells} is the spontaneous emission at the wells, β_1 and β_2 are the spontaneous emission coupling

factors for first order and second order mode respectively, and ω_1 and ω_2 are the resonance frequency for the first order and second order mode respectively. The Purcell factor was not taken into account in our analyses. Its insertion in the model would affect almost equally the MQW and the bulk structures. It is well know each confined mode has different group velocities, but here we have considered them equal since the difference should not be meaningful in our analysis. The gain and all recombination rates are carrier density dependent. For non-radiative recombination rates, we have considered Auger effect and surface recombination. The surface recombination is the most relevant in the case of nanolasers since the area/volume ratio is very high due to their small features. Typical values for Auger coefficient and surface recombination velocity of $1.1\text{x}10^{-31}$ cm^6/s and $5\text{x}10^4$ cm/s were considered, respectively. We calculate the dependence of material gain on carrier injection and wavelength using the same methods as described in the optimization procedure above. For τ_{cap} and τ_{esc}, typical theoretical values found in the literature were used: 60 and 300 ps respectively [97, 98] ([99]. §5). With such short characteristic times, thermal equilibrium of carriers can be assumed in the rate equation analysis.

The dynamic rate equations are solved until a steady state condition is reached. Figs. 4(a) and 4(b) shows the light output power calculated for the MQW and bulk gain respectively nanopatch lasers versus injected current (L–I) for several β factors. To facilitate a clear comparison, the same β factors were used for both barrier and well modes. The solid lines are the L–I curves for the well mode and the dashed lines are for the barrier mode.

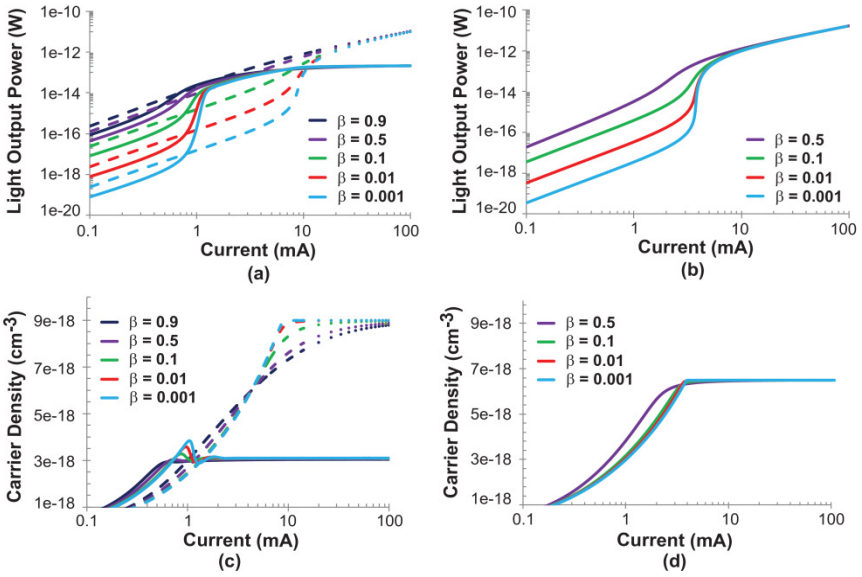

Figure 3.5: Log-log curves of the light output power versus injection current for (a) MQW gain media and (b) bulk gain media with several β's. (c) and (d) are the carrier density versus injection current for the MQW and bulk gain media respectively. The solid lines are for the first order mode while the dashed lines are for the second order mode. Note that in the MQW gain system, the second order mode is the barrier mode.

As depicted in Figure 3.5(a), the emitted power from the barrier (dashed line) overcomes the well emission (solid line) when under low injected current. This happens because the radiation losses of total Q for the barrier mode is almost half the radiation losses of the total Q for the QW mode so the double of the light is expected from the barriers. Comparing the curves for the same mode the emitted power is proportional to the β-factor. Therefore, at these low currents, light output that is proportional to the radiation loss of the barrier mode is larger. With further increase in current, the well mode goes into the ASE regime, seen by the change of slope in the curves around 0.5 to 1 mA, while the barrier mode remains in the electro-luminescent regime. At this point, the well emission is higher than the barrier emission. If current is further increased, stimulated emission is dominant for the well mode, and all solid lines show that the

system is close to the threshold condition. After this point, the curves suggest that the well mode has already passed threshold (which is commonly interpreted as the center point of the ASE regime at the inflexion point of the curve); however, the photon number doesn't rise linearly as it would in a single mode laser. Instead, the photon number stays constant due to the suppression of the well emission with the onset of barrier emission. If the well mode was the only resonant mode, or if there were no material gain available for other resonant modes, the well mode should show a clear threshold behavior. The second order mode, in the barriers, can reach a threshold condition at around 10 mA. The gain at the barrier mode is a result of the quasi-Fermi levels separation that leads to barrier pumping. Under this condition, the injected carriers into the active region are shared between the well and the barrier. It is uncertain whether the emission from the wells is lasing behavior or saturated amplified spontaneous emission.

Figure 3.5(c) shows the carrier density versus injected current for the well and barrier mode (solid and dashed lines, respectively). As expected for a typical laser behavior, the curves show carrier clamping for the well at the injected threshold current. Although there is a clear clamp for the carriers into the well mode, the carrier density continues rising linearly in the barrier until reaching the threshold carrier density for the barrier mode. Based on Figs. 4(c) and 4(a), we can conclude that the carrier clamping in the wells that saturates the well mode output power indicates a carrier leakage into the barriers. Figures 4(a) and 4(c) show that the transition from spontaneous to stimulated emission (lasing threshold) becomes smoother as β increases; this is an expected result [34]. The oscillations in the QW carrier density near this transition point are due to capture and escape carrier dynamics coupled to the recombination dynamics.

If it is possible to have a material with higher gain or a cavity with lower losses (reducing the threshold gain), all the curves for the well mode would be displaced to the left in Figure 3.5(a), and lasing would occur with a reduced threshold current. In the scenario with the opposite condition, if one employs a design with lower gain or a cavity with higher losses, all the curves for the well mode would be displaced to the right, with increased threshold current. This implies that the nanolasers under consideration, employing MQW gain medium, would hardly work as a laser. It should be clear that besides the inherent problem of the quasi-Fermi levels displacement until the barrier energy level, a small modification of the cavity design can drastically change the performance of the nanolaser. If the mode behavior of the first order mode is deviated from its optimal values, complete inhibition of lasing may possibly occur.

Indeed, even without the resonant mode with wavelength within the barrier bandgap, the QW mode would be saturated due to the leakage of carriers to the barriers and its spontaneous emission. A possible solution for the problem may be to change the depth of the wells and/or use other alloys, such as InGaAlAs that provides different band offsets, to avoid carrier population in the barriers. However, increasing the depth of the wells would create a second quantized level at the conduction band that also will compete for carriers. Also, it may create problems for the equalized carrier distribution amongst the wells. Therefore, the QW design for nanolasers may be extremely complex.

The same simulations were performed for the case of bulk gain medium, and the results are shown in Figure 3.5(b). In this case, we have used the typical rate equations (without the reservoir model) considering a multimode solution for photons. The β-factor in this case is no higher than 0.5 for each mode because now the spontaneous emission,

and consequently the stimulated emission, arises from the same material. Without this assumption the β-factor would be unphysical higher than 1. With identical β values for both modes, the spontaneous emission is equally shared between the two confined optical modes; however, the spectral density of the spontaneous emission is much higher for the first order mode and there is no available material gain for the second order mode. Consequently, the first order mode can reach the threshold around 5 mA, while there is no emission from the second order mode. The carrier density versus current injection is also shown in Figure 3.5(d), where we can see a smoother clamping at threshold for the highest β.

The threshold current simulated for the bulk device is high, 5mA, while experimental results with electrically pumped semiconductor nanolaser have reached threshold currents of only 1mA [37]. We believe this high value is due to the surface carrier recombination that is proportional to the area/volume ratio of the active region. In our case, parts of the top and bottom surface are exposed due to the pedestal, increasing the area for surface recombination, consequently increasing the threshold current [72]. In fact, our device has a reduced volume if compared with the recorded threshold current nanolaser, which increase even more the are/volume ratio [37]. Besides that, our gain values may be slightly underestimated due to the choice of the intraband scattering time value. This does not affect our conclusions in any form.

The model applied to account for carrier leakage to the barriers in MQW nanolasers can be extended to any laser cavity with two or more confined modes. The modal properties play an important role to determine the threshold gain and for each new mode an extra photon rate equation must be added into the system of coupled equations.

Independently of the number of confined modes, the modes with resonant wavelength nearest to the maximum gain will be favorable to reach the threshold condition. Since the threshold gain for these nanolasers are very high due to the small quality factors, the leakage of carriers to the barriers will always play an important role. It is hard to predict if a higher order mode will be more propitious to lasing or not, independently of the gain media, but a cavity mode engineering can be done to increase the difference between the threshold gain of the desired mode with all the other confined modes threshold gain.

These results indicate that bulk active medium is more suitable for this class of nanolasers because it inhibits carrier losses to barrier levels that only feed higher order modes.

3.5 Discussion

We discussed the advantages and disadvantages of using InGaAsP MQW as the active medium in comparison with InGaAs bulk material towards obtaining a high performance electrically pumped semiconductor nanolaser operating at room temperature. In the case of the MQW structure, we demonstrated that the level of current injection required to reach the threshold carrier density in the wells creates a highly degenerate condition where the quasi-Fermi levels displacement for electrons and holes allow the barriers to be populated. In this situation there is a clear competition for carriers between the barriers and the wells. Such competition saturates the emission from the QW mode while increasing the emission into the barrier mode. This saturation occurs independently of whether the emission from the well is stimulated or only spontaneous.

One may suggest an engineering of the multiple quantum wells to provide enough gain with a reduced carrier leakage to the barriers. The most obviously solution would be to increase the barrier height. In this case, there will be more quantized levels, which will provide transitions with shorter wavelengths and that could start to be populated before the threshold condition again saturating the emission around the desired wavelength. To avoid the second and higher quantized levels is necessary to reduce the wells thickness, but in consequence the confinement factor will also be reduced, increasing the modal threshold gain. So, the next step would be to increase the number of wells. Increasing the number of wells has the implication of creating a non uniform injection of carriers into the wells. It can also increase the volume of the active region leading to an increase of the entire laser volume. Another reasonable solution is to use strained quantum wells and barriers to increase the material gain and control the quantized levels energies. However, the defects at the interface of the strained growth material can increase the surface recombination due to possible imperfections created after the selective etching step to create the nanopillars. Besides the choice of using strained materials or performing further quantum well engineering, the design of the nanolaser become more complex. Since there are several implications in the design of nanolasers with MQW gain media, the authors agree that much more work should be done to conclude if it is possible or not to have a room temperature electrically pumped metallo-dielectric semiconductor nanolaser resonators with MQW gain media, but by now the evidences shown MQW are not the best suitable material to reach this objective.

In the case of bulk structure, we have shown the fundamental mode reaches the threshold condition long before the competition for carriers with the second mode starts.

The cost of using a bulk gain media to avoid the second order mode is a higher threshold current in comparison with the MQW device. This threshold current can be reduced if the bulk ternary alloy is substituted by a bulk quaternary alloy whose available material gain is within the optimized threshold gain for a specific cavity.

These results show that while quantum well structures allow large semiconductor lasers to have very low threshold current, they can inhibit lasing action in high gain demanding nanolasers due to a competition between wells and the barriers for injected carriers. Although the optical gain for bulk material is smaller and the transparency carrier density is larger than for MQW structures, the high threshold gain and the barrier pumping problem makes bulk gain media more suitable for obtaining room temperature electrically pumped metallo-dielectric semiconductor nanolaser resonators.

Chapter 3, in part, is a reprint of the material as it appears in F. Vallini, Q. Gu, M. Kats, Y. Fainman and N. C. Frateschi, "Carrier saturation in multiple quantum well metallo-dielectric semiconductor nanolaser: Is bulk material a better choice for gain media?" *Opt. Express,* vol. 21, pp. 25985-25998, 2013. The dissertation author was the primary co-researcher and co-author.

Chapter 4

Electrically Pumped Metallo-dielectric Nanolasers

The realization of optically pumped metallo-dielectric nanolasers described in Chapter 1 (Section 1.3) not only reveals behaviors specific to nano-scale devices and opens up new routes for the study of quantum behaviors in them, such as those discussed in Chapter 2, but also paves way to highly integrated photonic circuits. For practical insertions, as discussed in Chapter 3 (Section 3.1), it is always desirable to be able to operate the optical sources by electrical injection, allowing chip-level integration with existing electronic circuitry.

In semiconductor fabrication technology, electrical contacts are usually implemented using highly doped semiconductors. Apart from the increased optical losses that would result from the interaction of the optical mode with these highly doped regions, the optical mode profile is affected by the substitution of doped semiconductor for the otherwise lower index material [36]. Furthermore, any electrically pumped device requires an insulating region between the semiconductor annulus and the core and outer metals. In the case of the metallo-dielectric nanolasers, the dielectric shield also serves as the electrical insulation layer and the passivation layer.

Relative to its behavior in an optically pumped laser, the TE_{0m1} mode of an electrically pumped sub-wavelength metallo-dielectric laser suffers greater loss for two reasons. Firstly, the highly doped layers needed for adequate longitudinal carrier flow behave similarly to metal, in that the mode-free carrier interaction is a form of damping. Secondly, the same doped layers needed for electronic conduction also act as "plug" regions that confine the mode vertically. However, compared to dielectric or air plugs, the index contrast between these doped layers and the active region is very small, which leads to a less confined mode. In this chapter, we will see that, through a careful design process and judicious selection of device parameters, both of these challenges may be surmounted.

4.1 Initial electromagnetic cavity mode design and experimental validation

In Chapter 3, we saw that, as a result of carrier saturation at high carrier densities in MQW, bulk semiconductor can be a better choice for gain media in electrically pumped metallo-dielectric nanolasers. To realize the electrically pumped version of the metallo-dielectric nanolaser described in Chapter 1 (Section 1.3), InGaAs/InP double heterostructure grown on an InP substrate was chosen as the material platform, similar to the material stack reported in [34]. The schematic of the laser structure is shown in Figure 4.1(a). The material stack is the same as that detailed in Section 3.1 – the intrinsic 300 nm thick (h_{core}) InGaAs bulk layer is the active layer and the upper (470 nm thick) and lower (450 nm thick) InP layers are the cladding layers through which the injected carriers are flowing into the active layer. Highly doped n-InGaAs on the top and p-

InGaAsP in the lower layer form the n and p contact layers, respectively. Thin dielectric and metal layers are coated on the pillar structure which forms a metallo-dielectric cavity. As shown in the previous chapter, efficient lateral mode confinement in the sub-wavelength scale can be achieved in metallo-dielectric nanocavities, because metal offers high confinement while the dielectric shield helps reduce the optical ohmic loss by minimizing the mode overlap with the metal [53]. The dielectric constant of bulk silver at room temperature (ε_{Ag}=-120.43-*j*3.073 at 1.55 μm) was used in optical simulations [100].

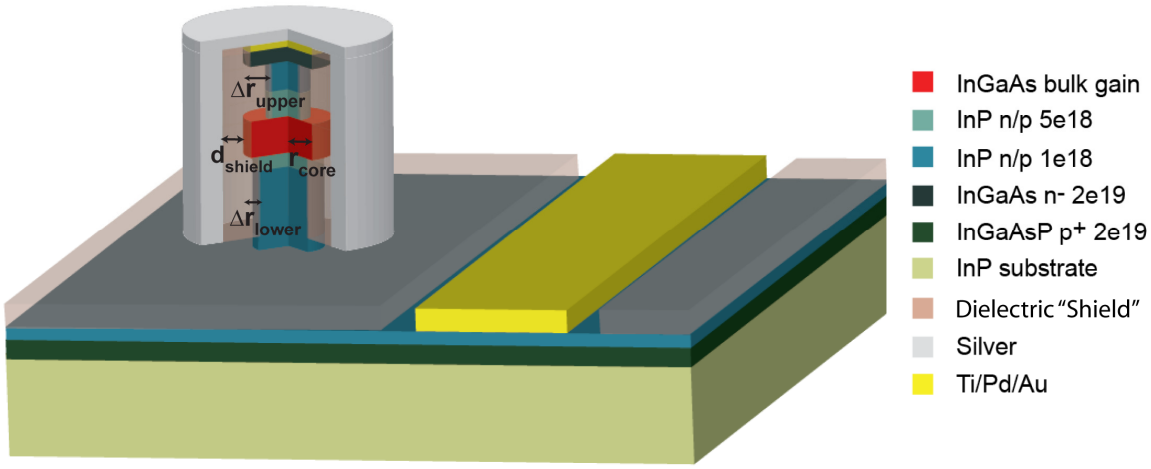

Figure 4.1: A schematic of the electrically pumped nanolaser with a dielectric shield and InP pedestals, where rcore is the radius of InGaAs gain layer, Δr_{upper} and Δr_{lower} are the undercut depths of the upper and lower InP pedestals, respectively. d_{shield} is the thickness of the dielectric shield layer.

The widths of the top and bottom doped InP layers can be intentionally reduced using selective wet etching of InP, such that InP pedestal layers can be formed for enhancing the vertical optical confinement while maintaining a conduit for carrier flow of both electrons and holes. To quantitatively analyze the effect of the pedestal in the structure, we calculated the Q factor and the threshold gain by varying Δr.

We first designed the wavelength scale cavity in which the gain core radius (r_{core}) is 750 nm ($2r_{core}$~λ), the InP pedestal undercut is 60nm (Δr_{upper}=Δr_{upper}=Δr=60 nm) and SiO_2 shield thickness (d_{shield}) is 150 nm. The calculated Q factor and threshold gain for the 750nm core radius device, with various Δr is presented in Figure 4.2(a). Shield thickness (d_{shield}) and the metal coating were kept constant. When Δr=0 nm, the Q factor is 163 and the threshold gain is 1505 cm^{-1}. As Δr is increased to 150 nm, the Q factor is enhanced to 1731; which is about an order of magnitude improvement; and the threshold gain is decreased to 99 cm^{-1}, which is a 93% reduction. As the pedestal undercut is made deeper (Δr is larger), the threshold gain is flattened and the resonant wavelength is shifted out of the optimal gain spectrum which is not desirable. We also calculated the Q factor and threshold gain when r_{core}=220 nm with changing the pedestal size which is shown in Figure 4.2(b). The Q factor is enhanced from 152 (Δr=0 nm) to 1572 (Δr=150 nm), which is an order of magnitude improvement. The resonant mode is strongly confined inside the gain layer with pedestal structure as shown in Figure 4.2(d) where r_{core}=220 nm and Δr=120 nm compared to the cylinder type structure shown in Figure 4.2(c). The threshold gain is reduced from 1473 cm^{-1} to 89 cm^{-1}, which is a 94% reduction. The threshold gain of 89 cm^{-1} is a promising result for possible room temperature operation of this laser structure. Both cases showed that the threshold gain is significantly suppressed when a minimal pedestal undercut is employed. At Δr=60 nm, the threshold gain of 750 nm and 220 nm r_{core} are 338 cm^{-1} and 236 cm^{-1}, respectively, which are still lower than the target threshold gain of 400 cm^{-1} [101]. This is another advantage since heat dissipation and carrier diffusion in the active layer have been critical issues for most pedestal type micro-disk lasers [85, 102].

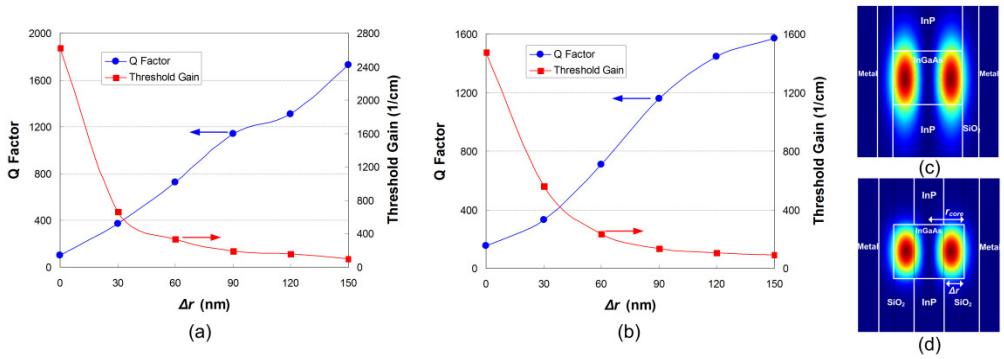

Figure 4.2: Numerical simulation results of the cavity Q factor and threshold gain for various pedestal sizes. $\Delta r_{upper}=\Delta r_{upper}=\Delta r$ is pedestal undercut depth. (a) r_{core} =750 nm, d_{shield}=150 nm, and Δr=0~150 nm. The blue curve represents the cavity Q and the red curve represents the threshold gain. (b) r_{core}=220 nm, d_{shield}=150 nm, and Δr=0 ~ 150nm. (c) Vertical cross section of the resonant mode field (TE_{011}) intensity when r_{core}, Δr=0 nm and d_{shield}=150 nm. (d) The resonant mode field (TE_{011}) intensity when r_{core}=220 nm, Δr=120 nm, and d_{shield}=150 nm.

To validate our simulated results, we fabricated electrically pumped nanolasers on both the wavelength scale (750 nm radius) and the sub-wavelength scale (355nm radius). Circular masks on InGaAs/InP heterostructure wafer were patterned by the e-beam lithography using HSQ resist. Subsequent reactive ion etching (RIE) was performed using CH_4:H_2:Ar gas chemistry to form the sub-wavelength scale pillar structure (the scanning electron microscope (SEM) micrograph is shown in Figure 4.3(a)). The selective etching of the doped InP layers was performed using HCl:H_3PO_4 (1:3) wet etching and the result of which is shown in Figure 4.3(b). 160nm of InP was etched on both sides through the wet etching process while the gain layer was preserved. 150 nm of SiO_2 layer was then conformally deposited on the pedestal pillar surface by Plasma-enhanced chemical vapor deposition (PECVD) process (Figure 4.3(c)) which both provides the low index shield minimizing the mode-metal overlap and passivates the InGaAs surface.

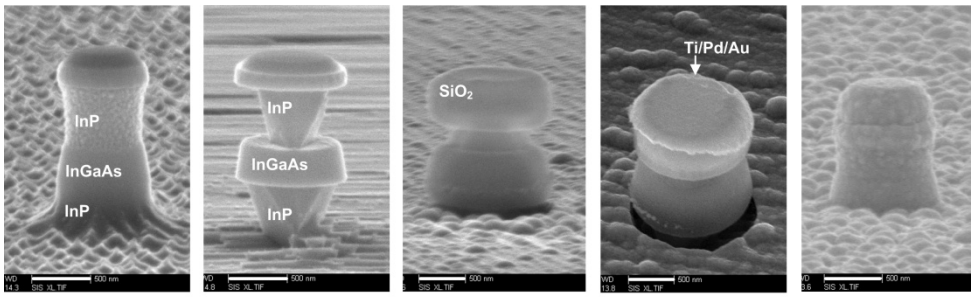

Figure 4.3: SEM micrographs of sub-wavelength pillar laser structure during fabrication procedure. (a) A pillar (r_{core}=395 nm) structure after dry etching. (b) Pedestal pillar is formed by selective InP wet etching. (c) Thin SiO_2 layer (150 nm) is deposited on the pillar structure by PECVD. (d) N-contact metal (Ti/Pd/Au) layer deposited on the top of the pillar. (e) Silver is deposited on whole pillar structure. Scale bar in each image represents 500 nm.

The SiO_2 layer on the top of the pillar structure was removed through the photoresist planarization and SiO_2 dry etching to access the n-side contact layer (n-InGaAs). Metal contacts (Ti/Pd/Au) were formed on the top of the pillar structure by the e-beam evaporation and lift-off (Figure 4.3(d)). After n contact formation, a 200 nm thick silver layer was deposited to cover the entire pillar structure including the top and side wall of the pillar and n contact pad (Figure 4.3(e)). A 20 nm thin chromium (Cr) layer was deposited prior to the silver deposition for better adhesion. Since a high optical loss of Cr could degrade the Q factor of the cavity and therefore increase the threshold gain, the unintentionally deposited Cr on the side wall of the pillar structure was subsequently removed by Cr wet-etching while protecting the adhesion layer on the substrate by the photoresist masking. P-contact was separately processed by the photolithographic patterning and wet-etching of SiO_2 and InP layer to access the underlying highly doped InGaAsP layer. The sample was then annealed to 400ºC for 60s to reduce the contact resistance. Finally, the sample was mounted on the device package (TO 8) and wire-bonded.

The devices were forward biased and the CW emission from the device was collected through a 20× objective lens and then imaged by the CCD camera. The spectral characteristics were analyzed by a monochromator with a maximum spectral resolution of 0.35 nm (with a 100 μm slit opening). The lasing characteristics of electrically pumped pedestal pillar lasers with two gain core radii (750 nm and 355 nm) were measured and analyzed. Figure 4.4(a) shows an SEM micrograph of the pedestal pillar in which r_{core}=750 nm, Δr=40 nm with 1.4μm pillar height. The shield thickness (d_{shield}) was 140 nm and silver provided the metal coating. In the numerical simulation, the Q factor was estimated to be 458 and the threshold gain was 534 cm^{-1} at the resonant wavelength of 1.50 μm. The lasing characteristics of this device at 77K are shown in Figure 4.4(b). Electroluminescence (EL) around 1.55 μm was observed when the injected current was higher than 20 μA. As the injected current was increased, the emission spectrum showed a spectral narrowing and the lasing peak appeared at 1.49 μm which is very close to the calculated resonant wavelength of 1.50 μm. The *L-I* curve (Figure 4.4(c)) shows a kink around the threshold current (50 μA) which is also an indication of the onset of lasing. The linewidth narrows to 0.9 nm at an injection current of 300 μA. We also investigated the temperature dependence of the lasing characteristics of this device. A local heater inside the cryostat kept the target temperature constant during the measurement. Lasing behavior was observed at 100K, 120K and 140K with constant current pump. The spectral evolution and *L-I* curve at 140K is shown in Figure 4.4(e). The lasing wavelength remained in the vicinity of 1.49 μm and the linewidth was also less than 1nm at 140K. However, the threshold current increased to 240 μA (inset in Figure 4.4(e))

which is 5 times higher than the threshold current at 77K. At 160K, spectral narrowing at 1.49 μm is still observed but lasing was not achieved primarily due to increased heat generation in the gain medium and the higher optical loss in the metal cavity. We also observed lasing behavior from a 355 nm core radius pillar laser at 77K [36]. We are currently working on optimizing the design and fabrication to minimize the electrical power dissipation and self-heating in the device. Incorporation of quantum well or quantum dot gain structures in the devices could also allow for building highly efficient sub-wavelength scale lasers [33, 35].

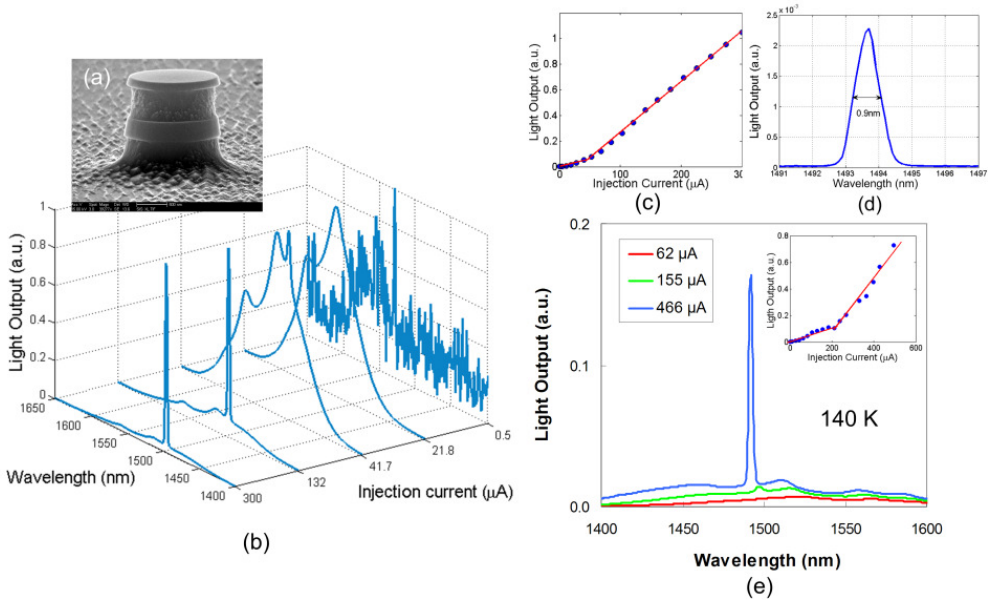

Figure 4.4: Lasing characteristics of r_{core}=750 nm pedestal sub-wavelength pillar laser device. (a) An SEM micrograph of r_{core}=750 nm pedestal pillar structure. (b) Spectral evolution graphs with increasing injection currents. (c) L-I curve of this device. (d) Linewidth measurement by a monochromator with 0.35 nm resolution. (e) Lasing spectrum measured at 140K. Inset shows L-I curve at 140K.

4.2 Thermal management and design co-optimization of electrically pumped metallo-dielectric nanolasers

While all nanolasers demonstrated for far in the literature enable fundamental research of various nanoscale phenomena [16, 59, 103], the design and analysis of nanolasers have focused almost exclusively on the optical mode, i.e. pure electromagnetic consideration, usually at 4.5K, 77K and room temperature. The experimental demonstrations have therefore focused on validating the optical cavity design and showing lasing behavior. Furthermore, the geometrical parameters used in design and simulations are usually idealistic, namely, straight shapes and smooth surfaces are assumed. As the field of nanolasers becomes more mature, and continues developing toward stable devices suitable for on-chip integration, more accurate and realistic electromagnetic consideration will be necessary, and other interdependent aspects of nanolaser design will need to be considered.

The first step towards nanolaser design co-optimization is to understand the temperature effects on nanolasers, and to use this knowledge to design and evaluate nanolasers with improved thermal performance. While thermal dynamics in VCSELs has been studied in depth [104, 105], it has been largely overlooked in nanolasers. However, thermal effects can have a profound impact on a nanolaser's performance, both as a potential failure mechanism and through the temperature dependence of material parameters such as gain spectrum and cavity mode behavior. In studying nanolaser thermal behavior, we seek to accomplish two primary goals, namely, to understand the

interplay of temperature-dependent effects on nanolasers, and to use this knowledge to design and evaluate nanolasers with improved thermal performance.

4.2.1 Simulation of nanolaser's temperature performance

4.2.1.1 Calculation of self-heating

First and foremost, the design of thermally-robust nanolasers requires the ability to simulate the temperature performance of nanolaser designs. The internal operating temperature of a nanolaser depends not only on the ambient temperature, but also on the amount of self-heating the nanolaser experiences. For an optically-pumped nanolaser, the self-heating will depend on the power absorbed from the optical pump; most of this absorbed power is converted to heat, and only a small portion is utilized in the generation of emitted light. For an electrically-pumped nanolaser, self-heating can be calculated using the effective heat source model used in VCSELs ([105]. §5.3), with modification to include the heat generated from non-radiative recombination in the active region, which is insignificant in micro- or large-scale lasers, but can play an important role in the self-heating of nanolasers.

In the modified effective heat source model, the cavity self-heating in an electrically-pumped nanolaser can be categorized into three mechanisms: 1) junction and heterojunction heating, 2) Joule heating, and 3) non-radiative recombination heating.

The first type of heating is generated at the interface of the differently doped semiconductor layers. It consists of junction heating, a term that is designated to describe the heat generated at the interfaces between the doped semiconductors and the un-doped gain region; it also consists of heterojunction heating, which accounts for the heat

generated at all doped semiconductor layer interfaces. Both terms are expressed as $I \cdot V_{Jn}$, where I denotes current and V_{Jn} is the potential difference at the n^{th} junction. These two terms take the same form below threshold, where I is the injection current I_{inj} Above threshold, I for junction heating is clamped at the threshold current I_{th}, while the heterojunction heating continues to use I_{inj}.

The second type of heating is Joule heating due to the series electrical resistance in all doped semiconductor layers, and takes the form $(I_{inj})^2 \cdot R_i$, where the resistance R_i of the i^{th} layer is calculated using the layer's thickness t_i, cross-sectional area A_i, doping concentration n_i, and carrier mobility μ_i [106], using the formula

$$R_i = \frac{1}{n_i q \mu_i} \frac{t_i}{A_i} \tag{4.1}$$

where q is the carrier charge. Each doped semiconductor layer, therefore, becomes a distributed source of Joule heating.

The third type of heating is generated by non-radiative recombination inside the gain region. In nanolasers, the non-radiative recombination heating is generated by Auger recombination and surface recombination. Auger recombination is significant at high temperatures and/or high carrier densities, and surface recombination, is significant at high temperature and/or large surface-to-volume ratios, the latter being especially significant relevant to nanolasers. Therefore, the gain region becomes a distributed heat source whose power is given by the non-radiative recombination, assuming that all non-radiative energy is converted to lattice vibrations through the creation of phonons.

The above calculation of junction and heterojunction heating requires knowledge of the potential differences needed to forward bias each junction. These can be obtained

using software such as SILVACO's ATLAS, a two-dimensional electronic device simulator. Given the operating temperature and properties of the device's constituent materials, ATLAS self-consistently solves the Poisson equation, the Schrodinger equation, and the carrier transport equations, considering Fermi-Dirac statistics, and obtains at each injection level the carrier density, the electron and hole quasi-Fermi levels, and the potential difference necessary to forward bias the junctions.

4.2.1.2 Simulation of nanolaser heat dissipation

Once the amount of nanolaser self-heating is known, the internal operating temperature of the nanolaser can be calculated using finite element software such as COMSOL's heat transfer module. Each layer and junction can be treated as a heat source according to the effective heat source model described in Section 4.2.1.1 (or by the amount of pump absorption, for optically pumped lasers), and the transient or steady-state temperature in the laser can be obtained.

Accurate thermal analysis of a nanolaser design requires knowledge of the thermal conductivity, heat capacity, and density of each material used in the nanolaser. Since these parameters are themselves temperature-dependent, the thermal analysis should ideally include thermal feedback mechanisms to update the material parameters as the device's temperature rises. However, experimental or experimentally-validated thermal parameters are lacking for most commonly-used nanolaser materials; temperature-dependent study of these material properties would be valuable to future nanolaser research.

Also valuable would be investigation into microscale heat transfer, as applied to nanolasers. The heat conduction models in most commercial finite element software, such as COMSOL, use macroscopic heat transfer equations, which may break down on the micro-/nano- scale. When the device dimension becomes comparable to or smaller than the mean free path of constituent materials' heat carriers, we enter the microscale heat transfer regime [107]. Microscale conductive and radiative heat transfer in VCSELs and convective heat transfer in carbon nanotubes have been studied [107], but this has not yet been a subject of attention in the field of nanolasers.

The above analysis also does not include the effects of non-ideal ohmic contacts, defects at material interfaces, or the effects of surface passivation on surface recombination [108]. Further refinements of nanolaser models to include these and other parameters will serve to increase the accuracy and value of nanolaser thermal simulations, as well as to suggest avenues for design improvement.

4.2.2 Choice of dielectric material and fabrication techniques for thermal management

One method of improving a laser's thermal performance is through use of materials with higher thermal conductivities, to improve the laser's ability to dissipate heat. Metal-clad nanolasers have the possibility of heat dissipation via conductive heat transfer to the metal cladding.

Two types of dielectric materials, namely SiO_2 and silicon nitride (SiN_x), have been used in metal-clad nanolasers. In electrically pumped nanolasers, for SPP mode operation, the dielectric layer is on the order of 20 nm to provide electrical insulation;

SiN_x is used because of its effectiveness as a passivation layer [34, 109]. For photonic mode operation, a thicker shield is usually used, to minimize cavity threshold gain, from the electromagnetic point of view [56, 110]; SiO_2 is the usual choice of shield material, because its low refractive index compared to SiN_x yields better mode confinement [53]. However, both SiO_2 and SiN_x largely prevent heat dissipation through the shield, due to their low thermal conductivities.

To this end, sapphire (crystalline alumina (Al_2O_3)) would a good choice as a low refractive index, thermally conductive dielectric layer. Indeed, sapphire is chosen over air as the membrane or substrate material in sapphire-bonded photonic crystal lasers, because of its ability to conduct heat better than air [111]. Sapphire is also a common substrate material for nanowire lasers, owing to its epitaxial compatibility (matching Wurtzite crystal structures) with semiconductor nanowires, as well as its optical transparency over a wide range of wavelengths [112, 113]. However, thin film deposition techniques, which are required to create shield layers on nanolasers, yield amorphous Al_2O_3 (α-Al_2O_3), rather than the crystalline sapphire form. α-Al_2O_3 has a lower thermal conductivity than its crystalline counterpart, but is nonetheless a better thermal conductor than SiO_2 or SiN_x. The thermal properties of SiO_2 [114] and Si_3N_4 [114] deposited via plasma-enhanced chemical vapor deposition, and α-Al_2O_3 deposited via atomic layer deposition (ALD) [115-117] are listed in Table 4.1.

Table 4.1: Optical and Thermal Properties of Materials Used in Numerical Modeling, at 1550nm and 300K

Material	Permittivity ε	Thermal conductivity T_c ($W \cdot m^{-1} \cdot K^{-1}$)
α-Al_2O_3	2.69	1.7-20
SiO_2	2.1	1.1
Si_3N_4	4.49	1.7
InP	6.96	68
$In_xGa_{1-x}As$ (x=0.53)	11.56	16
$In_xGa_{1-x}As_{1-y}P_{1-y}$ (x=0.773,y-0.493)	11.83	11
Ag	-130.6-j3.33	429

α-Al_2O_3 created by wafer fusion has been explored as a thermally conductive membrane layer in photonic crystal microlasers, but its thermal advantages for metallo-dielectric nanolasers have not been explored so far. Although ALD deposited α-Al_2O_3 with thickness typically less than 20nm has been used in nanolasers, its role was strictly for electrical insulation or passivation, which utilizes its surface smoothness [118, 119]. It was mentioned in Ref [120] that Al_2O_3 or diamond can potentially replace SiO_2 as the low-index membrane in silicon nanomembrane reflector VCSELs, such that improved thermal conductivity and power dissipation handling can be achieved, but so far this discussion has not been followed by experimental implementation.

α-Al_2O_3 also shows promise because of its surface smoothness when deposited via ALD. The breakdown voltage and leakage current of a device are directly related to the number of surface states, and in turn, surface roughness. Although SiN_x is traditionally used as the passivation layer [109], high-k dielectrics deposited by ALD have shown advantages over SiN_x for (metal–oxide–semiconductor field-effect transistor

) MOSFETs and solar cells by having atomic layer smoothness [118, 119]. In nanoscale devices, as the surface to volume ratio becomes significant, ALD deposited dielectrics becomes an especially good candidate.

In addition to choice of shield material, there is another, potentially thermally-relevant, parameter to choose: the diameters of the InP pedestals above and below their gain region. To better control this parameter, we develop a multi-step InP wet etching process [38]. Using similar fabrication procedure as detailed in Section 4.1 (Figure 4.3), cylindrical pillar structures such as that shown in Figure 4.5(a) are formed. Next, a two-step selective wet etching process is used to etch the doped InP layers, without affecting the InGaAs gain layer, creating undercut InP pedestals. In the first step of the selective etching, the $HCl:H_3PO_4$ (1:4) etchant combination is used, similar to that employed in Section 4(Figure 4.3). Due to the $HCl:H_3PO_4$ combination's anisotropic etching, the etch rate is slowest in the (111) plane, resulting in cone shaped regions (Figure 4.5(b)). In the second step, the $HCl:CH_3COOH$ (1:4) combination is used, whose anisotropic etch rate in the (111) plane also produces cone shaped regions, but in the opposite direction of that from the $HCl:H_3PO_4$ etchant combination, if used alone (Figure 4.5(c)). Therefore, applying the two chemistries sequentially with the proper ratio of etching times, vertical pedestal sidewalls can be obtained, (Figure 4.5(d)). Because the etching rate varies for different dopant types and concentrations, the upper InP layer is always narrower than the lower InP layer.

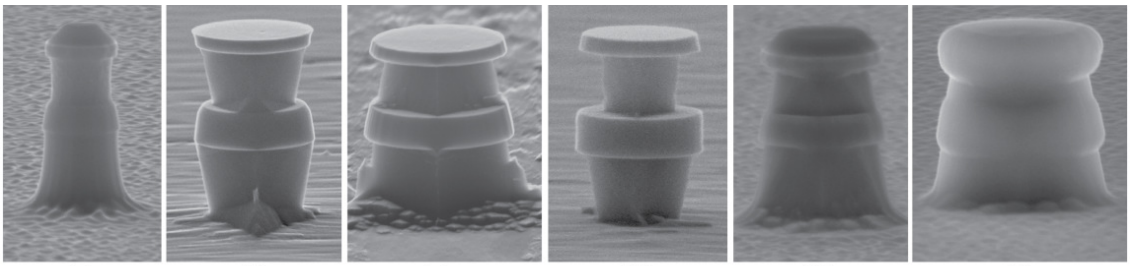

Figure 4.5: SEM images of pedestal pillar lasers (a) after RIE, (b) after HCl:H_3PO_4 etching alone, (c) after HCl:CH_3COOH etching alone, (d) after the 2-step selective etching. (e) Fabricated device after the 2-step selective etching. (f) Fabricated device after α-Al_2O_3 deposition.

After removing the HSQ mask following the two-step InP etching, we deposit α-Al_2O_3 conformally around the semiconductor pillar using thermal ALD (Beneq TFS 200 system). The growth temperature is set at 250°C. Trimethylaluminum $Al(CH_3)_3$ (TMA) precursor is used as the Al source, and H_2O is used as the oxygen source. One layer of α-Al_2O_3 is grown by 45 ms of TMA exposure, 850 ms of N_2 purge, 50 ms of H_2O exposure, and 850 ms of N_2 purge, and the procedure is repeated until the desired thickness is reached. The purpose of the N_2 purge is to minimize the parasitic chemical vapor deposition during the growth. The film thickness is then measured, using both ellipsometry and SEM (Figure 4.5(f)). To access the n- InGaAs contact layer in preparation for n–type electrode deposition, the α-Al_2O_3 region on top of the pillar structure is removed through photoresist planarization and etching of α-Al_2O_3. Although the CHF_3:Cl_2 chemistry is usually used in Al_2O_3 etching, we avoid the use of Cl_2 due to its reactivity with III–V semiconductors. Instead, we use CHF_3:Ar (50:10 sccm) plasma at 40 mTorr and 150 W RF power in a RIE chamber, resulting in an etch rate of ~8 nm/min. Electrodes (Ti/Pd/Au) and cavity metal (Ag) are formed through multiple

photolithography steps, metal deposition or sputtering, lift−off and annealing processes, similar to those described in Section 4 (Figure 4.3).

4.2.3 Preliminary experimental validation

We fabricated devices with modest undercut, as shown in Figure 4.5(e), and, used ALD deposited α-Al_2O_3 (Figure 6(f)) to minimize anticipated self-heating in the semiconductor stack. We tested the device in a standard mirco-EL set up as that described in Section4. We characterized the device (SEM images of which are shown in Figure 4.5(e) and (f)) of r_{core}≈575 nm, d_{shield}≈170 nm, Δr_{upper}≈90 nm and Δr_{lower}≈20nm. We note that the shield thickness and InP undercut depth are not optimized for the device. Figure 4.6(a)−(c) depict the device's behavior at an ambient temperature of 77K under CW electrical injection. The side-view schematic of the fabricated device is shown in the inset of Figure 4.6(a), where different regions are represented by their respective refractive indexes. Figure 4.6(a) shows the measured emission spectra, from a broadband EL at low injection currents to an emission peak with 2 nm linewidth at 1515 nm, at high injection currents. The peak at 1515 nm is one of two degenerate WGM, as shown in Figure 4.6(b). At higher pump levels, as depicted in Figure 4.6(a), a broad peak appears at shorter wavelengths than the main peak, due to the existence of an additional cavity mode at 1423 nm (see Table 4.2). This cavity mode begins to compete with the 1515 nm mode, with the help of a broadened and blue-shifted material gain spectrum at high pump levels. When the injection current is increased beyond 450 μA, the 1515 nm mode stops further narrowing in linewidth or rising in amplitude, and the mode at 1423 nm continues to increase in amplitude. While lasing threshold might not have been reached for the

1515 nm mode, for our analysis in the following sections we approximate the threshold current to be the current level beyond which this mode linewidth stops narrowing, ~400 μA in this case. The linewidth under this condition is depicted in Figure 4.6(b) In Figure 4.6(c), we plot the measured current–voltage (*I*–*V*) curve at 77 K.

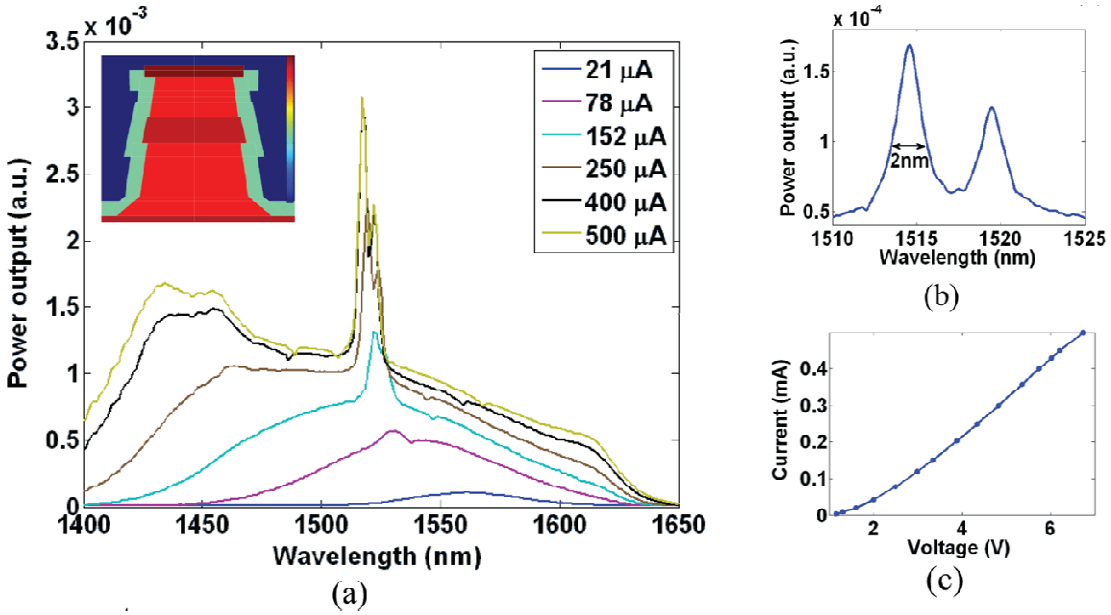

Figure 4.6: Measured and simulated device performance at an ambient temperature of 77K. (a) Spectral evolution with increasing injection current. Inset: side-view of the fabricated device schematic. (b) Linewidth measurement by a monochrometer with 0.35 nm resolution, at an injecion current of 0.4 mA. c) I–V curve at 77K.

3D simulation of the fabricated device at 77K was then performed using commercial software COMSOL. The cavity resonance wavelength depends on temperature to the extent that the complex relative permittivity ε = ε'+j·ε", of the metal and semiconductor depend on temperature. Specifically, the resonant wavelength depends on the real part of the permittivity, whereas the imaginary part determines gain or loss. We use silver permittivity values at 1550 nm from [17], ε(Ag,77K) = −132.5−j0.5, which is calculated via a temperature dependent Drude model [121, 122]

and scaled to match the empirical data of Johnson and Christy [100]; at room temperature, $\varepsilon(Ag,300K)=-130-j4.2$. The imaginary part of silver's permittivity is strongly dependent on temperature: it changes by nearly an order of magnitude, while the real part changes only by 2%. The real permittivities of semiconductors are only weakly dependent on temperature. Therefore, the effect of temperature on the cavity resonance wavelength is small [17]. Due to the lack of empirical thermo-optic data at temperatures other than 300K for the various semiconductor compositions in our cavity, we assume constant permittivity values with respect to temperature. Given that the thermo-optic coefficients are generally on the order of 10^{-4} [123], [124], this assumption has a minor effect on the resulting locations of the cavity resonances.

Table 4.2 lists the simulated optical mode behavior of the two experimentally observed competing modes in terms of resonant wavelength λ_{cav}, cavity Q-factor, mode confinement factor Γ, and threshold gain $g_{th}=2\pi n_g/(\lambda Q\Gamma)$, where n_g is the group refractive index. At 77K, two degenerate WGM modes, with azimuthal mode number M=5, reside at around 1515 nm, in agreement with the two narrow emission peaks observed at the same wavelengths (Figure 4.6(b)). Even though the degenerate modes at 1423 nm have similar g_{th}, the magnitude of the material gain at those wavelengths is less than that at 1515 nm at low to moderate pump levels. At higher pump levels, as well as at higher ambient temperature, these modes compete, limiting laser performance [38]

Table 4.2: Simulated Optical Mode Characteristics at 77K, of Experimentally Observed Competing Modes

λ_{cav} (nm)	g_{th} (cm^{-1})	Q	Γ	Degeneracy
1423	8415	67	0.268	Yes
1515	10622	51	0.259	Yes

Even though self-heating is sometimes believed to be the most detrimental effect in nanolaser performance at high temperatures and/or under CW pumping [125], as we will show in the next section, this is not the case in our fabricated device. Instead, the most detrimental effect to the operation of our device is the angled sidewalls and the negligibly undercut lower InP pedestal, causing high radiation loss and poor mode confinement, and thus high threshold gain. In order to reach such high gain values in the material, both cryogenic temperature operation and a high carrier density are necessary.

We note that these detrimental effects are only evident under detailed optical simulations that take sidewall angles into account, as well as the differing amounts of undercut in the upper and lower InP pedestals (Table 4-3). These are not typically simulated, yet are common experimental occurrences. For example, the gain sidewalls formed by RIE are not always vertical [36], although the fabrication process can be calibrated to minimize the deviation from a vertical sidewall [110]. The upper and lower InP pedestals are frequently cone shaped, due to anisotropic properties of the etchants, as detailed in Section 4.1. Even though sidewalls that are more vertical than those in the devices of Section 4.1 [36] can be obtained using the two-step InP selective etching process, there is usually at least some sidewall angle. Furthermore, due to the material-selectivity of the etchants, the InP layers with different doping types and concentrations

inevitably have different undercut depths. To show the effects of the abovementioned differences between the fabricated and typically simulated structures, we construct the model of the lasing device with the exact geometric parameters measured from SEM images during various fabrication steps. We additionally model three increasingly idealized structures with the same device footprint and gain volume (Table 4.3, second to fourth rows) as the experimentally realized one (Table 4.3, first row). The first structure has a vertical gain sidewall, whose radius is set to match that measured at the center of gain of the fabricated device, but has as-fabricated pedestals (Table 4.3, second row); the second structure has a realistic undercut ratio between the upper and lower pedestal, albeit all sidewalls are set to vertical (Table 4.3, third row); and the third structure has vertical sidewalls and equal amount of undercuts in the upper and lower pedestal (Table 4.3, fourth row). Table 4.3 lists the simulated optical mode characteristics including λ_{cav}, g_{th}, Q and Γ, of the four structures at 77K. We notice that the idealized structures typically have much better performance.

Table 4.3: Optical Mode Simulation of the Lasing Cavity Mode of the As-fabricated as well as Three Increasingly Idealized Structures, at 77K.

	λ_{cav} (nm)	g_{th} (cm^{-1})	Q	Γ
As-fabricated	1515	10622	51	0.259
Realistic undercut; Vertical gain sidewalls	1512	9809	53	0.270
All sidewalls vertical; realistic undercut ratio	1506	373	768	0.495
All sidewalls vertical; 1:1 undercut ratio	1504	103	2445	0.562

Experimental and simulation results of the above device highlights a case in which the combination of thermal, material, electrical, and optical analyses revealed that the most detrimental effect at high temperatures and/or under CW pumping was not the usually-suspected self-heating [125]. Nor was the laser performance limited by increased metal loss at room temperature [38]. Instead, the most detrimental effect to the operation of the device was the angled sidewalls and the negligibly undercut lower InP pedestal, causing high radiation loss and poor mode confinement, and thus high threshold gain [38].

4.2.4 Nanolaser's electrical and thermal analysis

In this section, we use the procedure outlined in Section 4.2.1 to evaluate the temperature performance in the fabricated nanolaser with α-Al_2O_3 shield (Section 4.2.3) at 300K, where material parameters are more available than those at the experimental ambient temperature of 77K. The ability to determine the operating temperature of a

nanolaser design at a given ambient temperature and pumping level, as discussed in Section 4.2.1, are crucial to the design of nanolasers for improved thermal performance, and to the evaluation of their success.

We use the software SILVACO's ATLAS to predict the heterojunction and junction heating. Because sidewall angles are not expected to be as critical to the device's electrical behavior as to its optical behavior, as well as due to the complexity in constructing angled-sidewall structures in SILVACO, we model a range of devices with straight sidewalls, similar to those shown in the last two rows of

Table 4.3, and vary the gain and pedestal radii within the range of widths measured in our fabricated device. We found that such variations did not affect the device's performance significantly; thus we take the average of the results. At an injection current of 0.5 mA, Figure 4.7(a) plots the simulated electric potential along the pillar length with respect to the minimum potential level. Length=0 corresponds to the top of the laser pillar (the top of the n−InGaAs layer), and the device temperature is set to be 300K. From the voltage rise or drop at each interface, we calculate the amount of junction and heterojunction heating at the respective interfaces. Junction heating, summed from the contribution from the InP and InGaAs gain interfaces, is 0.122 mW. We obtain heterojunction heating of 0.517 mW in a similar manner. Joule heating is estimated to be 0.214 mW. To calculate heating generated by non-radiative recombination, we first obtain the carrier density and the QFL separation as a function of bias current from SILVACO, plotted in Figure 4.7(b) and (c), respectively. At 0.5 mA, using the corresponding carrier density, the QFL separation which describes the transition energy, as well as the surface velocity and Auger coefficient at 300K [126], we estimate

the heating to be 2.621 mW. The total estimated heat source power at 0.5 mA current is 3.474 mW, comparable to the experimental value of 3.375 mW injection power. We note that, in calculating the junction heating, we had used a threshold current of 0.4 mA, as roughly estimated in Section 4.2.3. If this value was under-estimated, junction heating would correspondingly increase. However, we do not expect this difference to affect the thermal performance significantly, because non-radiative heating is an order of magnitude greater than junction heating at such high injection levels. We also recognize the discrepancy between the experimental and simulated bias voltages at the same injection current. This is most likely due to the non-ideal Ohmic contacts of the fabricated device as well as defects at material interfaces, the behavior of which is not captured in the simulation.

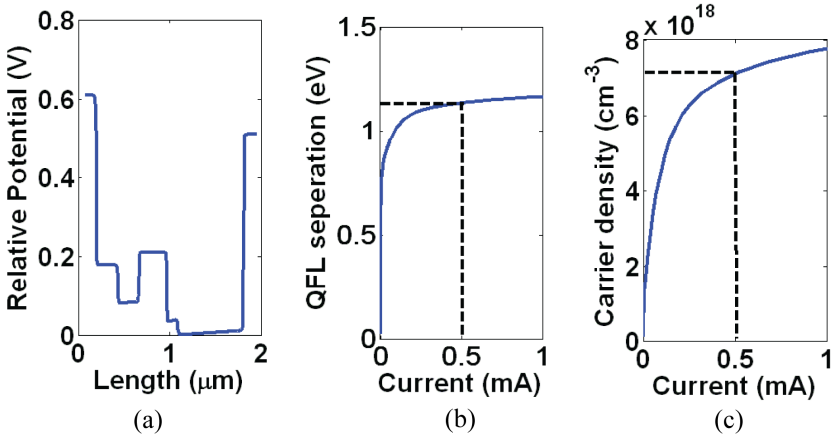

Figure 4.7: (a) Potential difference across the pillar at 0.5 mA bias current, where Length = 0 corresponds to the top of the structure. (b) Carrier density as a function of bias current. (c) QFL separation as a function of bias current.

The heat sources at the various junctions and layers are subsequently input into COMSOL's 2D axial-symmetric steady-state heat conduction model for thermal analysis. In this model, the structure matches the fabricated geometry, including sidewall angles

and undercut amounts. The bottom surface of the 350 μm thick InP substrate is kept at the constant ambient temperature of 300K, and the far edge of the 220 nm thick Ag cavity metal coating, 20 μm from the laser, as schematically drawn in Figure 4.1, is also set to 300K, allowing the possibility of heat conduction through the metal cladding layer. All other boundaries are set to symmetry/insulation, except for the top surface of the Ag, which is allowed to lose heat through radiation. The thermal conductivities of the constituent materials are listed in Table 4.1. Because the literature thermal conductivity T_c values for ALD-deposited α-Al_2O_3 ranges from 1.7 to 20 W/(m·K), we perform two simulations with T_c of 20 and 10W/(m·K), respectively. For the lowest T_c value of 1.7 W/(m·K), the thermal performance approaches that of a device with SiO_2 shield, which we also simulate for comparison. Figure 4.8 shows the temperature distribution, steady-state temperature T_{ss} and heat flux of the fabricated device, with different shield materials and/or thermal conductivities. We notice that while a higher thermal conductivity corresponds to a lower steady-state temperature, the steady-state temperatures reached with a lower-conductivity shield are also moderate. This is a consequence of the relatively large gain core diameter, which mitigates surface recombination and Joule heating, as well as the large upper and lower pedestals, which mitigate Joule heating and provide a large pathway for heat dissipation. Nonetheless, the arrows indicating the magnitude and direction of the heat flux highlight the advantage of the α-Al_2O_3 over SiO_2. In the case of the α-Al_2O_3 shield, a significant portion of the heat generated in the pillar is dissipated through the shield into the cavity metal. In the case of the SiO_2 shield, the path for heat dissipation is limited to the semiconductor pedestals.

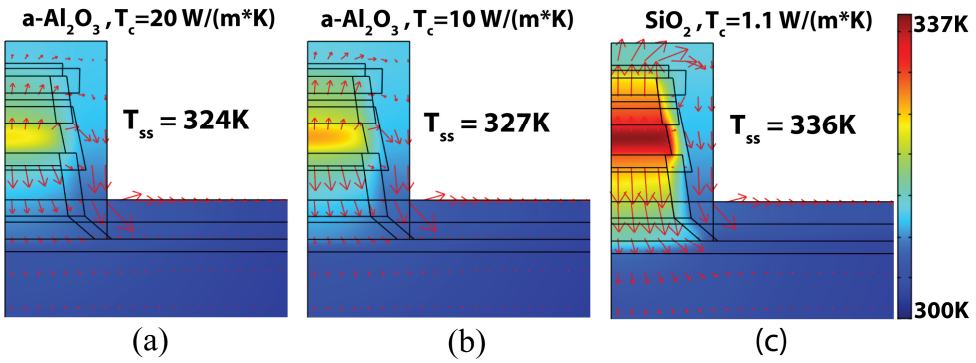

Figure 4.8: Surface temperature distribution, steady-state temperature T_{ss} and heat flux (indicated by the red arrows) of the fabricated device, with α-Al_2O_3 shield, taking (a) the highest literature thermal conductivity value of 20 W/(m·K), (b) medium literature thermal conductivity value of 10 W/(m·K). (c) SiO2 shield with well-calibrated literature thermal conductivity value of 1.1 W/(m·K).

Because material gain is dependent on the device temperature and pump level, it is beneficial to calculate the gain spectrum at different pump levels and the corresponding SILVACO – calculated carrier densities. This analysis procedure is detailed in Section 4.3, when we design a device for room temperature operation. For the present purpose of analyzing the fabricated nanolaser, we note that material gain decreases as temperature increases, and consequently, lasing is harder to achieve, with all else equal. This decrease in material gain can be compensated by increased pumping, but at the expense of a broadened and blue-shifted material gain spectrum, leading to mode competition. Additionally, the surface recombination rate is related to the square-root of temperature, and can become significant at high temperatures [126]. None of these effects is captured in the electromagnetic model alone. Combining all aspects of the analysis, we believe that the absence of lasing behavior of the fabricated device at temperatures higher than 77K is a result of the optical mode's high threshold gain (Table 4.3), rather than the self-heating in the device.

4.3 Integrated nanolaser design for room temperature operation

The integrated analysis of optical, electrical and thermal properties revealed that, the poor performance of the device in Section 4.2.3 is a result of poor optical mode properties, rather than the commonly believed thermal heating in CW pumped nanolasers. These insights motivated the design of an improved nanolaser for room temperature operation, in which the pedestal undercut was increased to improve the mode confinement, and thus Q-factor and threshold gain. Keeping all other geometrically laser parameters the same as the fabricated device (Figure 4.5(e)), including gain volume and sidewall angle, optical simulations were performed to determine the optimal InP undercut depth. To reflect a realistic undercut condition, we use upper and lower pedestal width ratio obtainable from the two-step InP selective etching process (which etches the differently-doped upper and lower pedestals at different rates). We use the experimentally-measured gain and top n- InGaAs layer sidewall angles; as we will show, even with angled gain sidewalls, a high degree of mode confinement to the gain region is possible. Here, we model vertical pedestal sidewalls, while noting that the sidewall angles achievable in fabrication will vary, but, compared to the poorly-confined case in

Table 4.3, will not have as large a deleterious effect on modes that are well-confined to the gain region. The rigorous investigation of the effects of non-vertical pedestal sidewalls, combined with non-vertical gain sidewall and various undercut depths, is outside the scope of this report, but is a subject of future research.

The improvement of optical properties of the mode with increasing undercut depth is shown in Figure 4.9(a), which shows the threshold gain g_{th} and Q-factor of the lowest g_{th} mode, at each undercut level. We define the optimal undercut depth to be the depth of the lower InP pedestal, Δr_{lower}, which is the lesser of the two undercuts, that corresponds to the minimum threshold gain in Figure 4.9(a). We find the optimal Δr_{lower} to be 174 nm, more than two times larger than that obtained in [36], which was $\Delta r_{lower}=\Delta r_{upper}$ ~80 nm for both the R_{core}=350 nm and 750 nm structures. As the undercut depth is increased, the cavity resonant wavelength of each mode blue-shifts, and eventually, moves outside of the wavelength window of interest, 1300 nm to 1650 nm. This behavior is captured in Figure 4.9(a): at Δr_{lower}~200nm, the original lasing mode has blue-shifted beyond the gain bandwidth window, leaving a higher order mode to take its place as the lowest g_{th} mode, which has a lower Q and a slightly higher g_{th} than the original mode. The lowest threshold gain corresponds to a structure that has a Δr_{lower} of 174 nm, whose side-view is shown at the bottom of Figure 4.9(a). Figure 4.9(b) depicts the target structure's λ_{cav}, the electric field distribution, g_{th}, and Γ, for modes with g_{th}<200 cm^{-1} and whose resonant wavelengths fall within the material EL spectrum of 1300–1650 nm. Compared to the fabricated structure with g_{th} of 10610cm^{-1} at 300K, a 99.7% reduction in threshold gain is obtained.

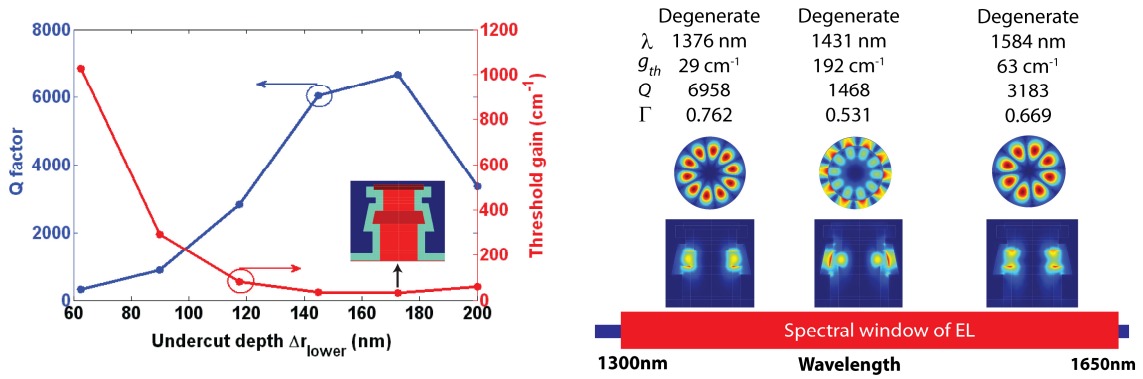

(a) (b)

Figure 4.9: Simulated, room temperature (a) Threshold gain gth, cavity Q-factor, and diagram of the structure with the lowest gth (b) Mode distribution of all modes that fall within the spectral window of EL and have g_{th}<200 cm^{-1}, for the device geometry shown in (a).

For the thermal analysis, following the procedure outlined in Section 4.2.1, we use SILVACO to estimate the heat generation in various regions of the device, at the same 0.5mA injection current used in Section 4.2.4. Figure 4.10 shows the temperature distribution, maximum steady-state temperature T_{ss} and heat flux of the designed device, with different shield materials and/or thermal conductivities. The total heat generated in the undercut laser design is higher than that of our fabricated device (Figure 4.8), largely attributed to the increase in Joule heating in the pedestal layers and junction heating at the interface between the lower InP pedestal and the highly doped p+ InGaAsP layer. Because this heating occurs near the edges of the laser stack, where heat may be more readily dissipated through the substrate and metal shield, the impact of this additional heating is minimal. In addition, SILVACO predicts ~2% decrease in carrier density of the designed device compared to that in the fabricated one, leading to a ~5% decrease in non-radiative heating power generated in the gain layer. The net effect is that the final temperature in the T_c = 20 W/(m·K) α-Al_2O_3 shield device is actually a fraction of a

degree lower than that of the as-fabricated device, while the T_c = 10 W/(m·K) α-Al2O3 shield device is a only fraction of a degree higher than that of the as-fabricated device. In the case of the SiO_2 shield, however, we observe a 17K rise. This observation agrees with intuition: as the undercut is made deeper, and the pathway for heat dissipation through the pedestals decreases, the ability to dissipate heat through the shield layer becomes more important. We expect the same trend as the gain core radius is decreased.

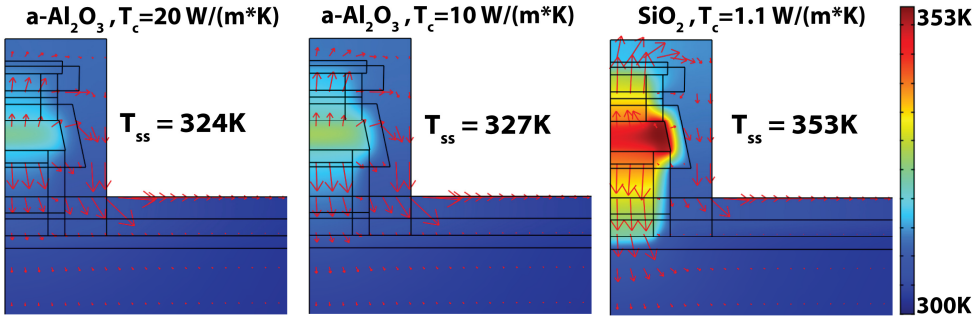

Figure 4.10: Temperature distribution, maximum steady-state temperature Tss and heat flux (indicated by the red arrows) of the designed device, with (a) α-Al_2O_3 shield with the highest literature thermal conductivity value of 20 W/(m·K), (b) α-Al_2O_3 shield with medium literature thermal conductivity value of 10 W/(m·K), and (c) SiO_2 shield with well–calibrated literature thermal conductivity value of 1.1 W/(m·K).

Next, we analyze the optical performance of our design at the operating temperatures of 77K, 300K, and 327K (taking ε(Ag,327K) = −130.4–0.569i [17]); the latter is the predicted steady-state temperature (assuming a modest T_c value of 10 W/(m·K) for the α-Al_2O_3 shield) when operated at an ambient temperature of 300K. The optical characteristics of the lowest threshold gain mode of the designed device, in terms of resonant wavelength λ_{cav}, cavity Q-factor, mode confinement factor Γ, and threshold gain g_{th}, are tabulated in Table 4.4.

Table 4.4: Simulated Optical Characteristics of the Lowest Threshold Gain Mode of the Designed Device at 77K, 300K and 327K

Temperature (K)	λ_{cav} (nm)	g_{th} (cm^{-1})	Q	Γ
77	1376	5	43350	0.762
300	1376	20	6958	0.762
327	1376	31	6487	0.762

Next, we analyze the amount of material gain available at our simulated steady−state operating temperature and lasing wavelength, and compare this to the mode's simulated threshold gain. Following the semiclassical approach of [17], we compute properties of the gain material at 77K, 300K, and 327K. Figure 4.11(a) shows the material gain spectrum for a range of carrier densities from 1e18 cm^{-3} to 9e18 cm^{-3}, at 327K. At the 0.5 mA injection current used in the thermal and electromagnetic simulations above, we find the carrier density of our designed device to be 7.072e18 cm^{-3}. We plot the material gain spectrum at this injection (Figure 4.11(b)), as well as the material gain with increasing carrier density at the wavelength of the lowest-threshold mode, 1376 nm (Figure 4.11(c)). Comparing the available material gain at the carrier density of 7.072e18 cm^{-3} with the predicted threshold gain values listed in Figure 4.9(b), even though the mode simulations do not capture the non-radiative loss that is directly related to temperature and carrier density, we expect that the laser could be operated at a much lower injection level than the 0.5 mA considered, as evidenced in Figure 4.11(d). Lastly, with a very slight change in the gain core radius, the cavity mode can be tuned to fall in the middle of the gain spectrum. A similar highly-undercut approach will likely

work for other shield materials, shield thicknesses, and gain volumes as well; a generalized investigation is the subject of future research.

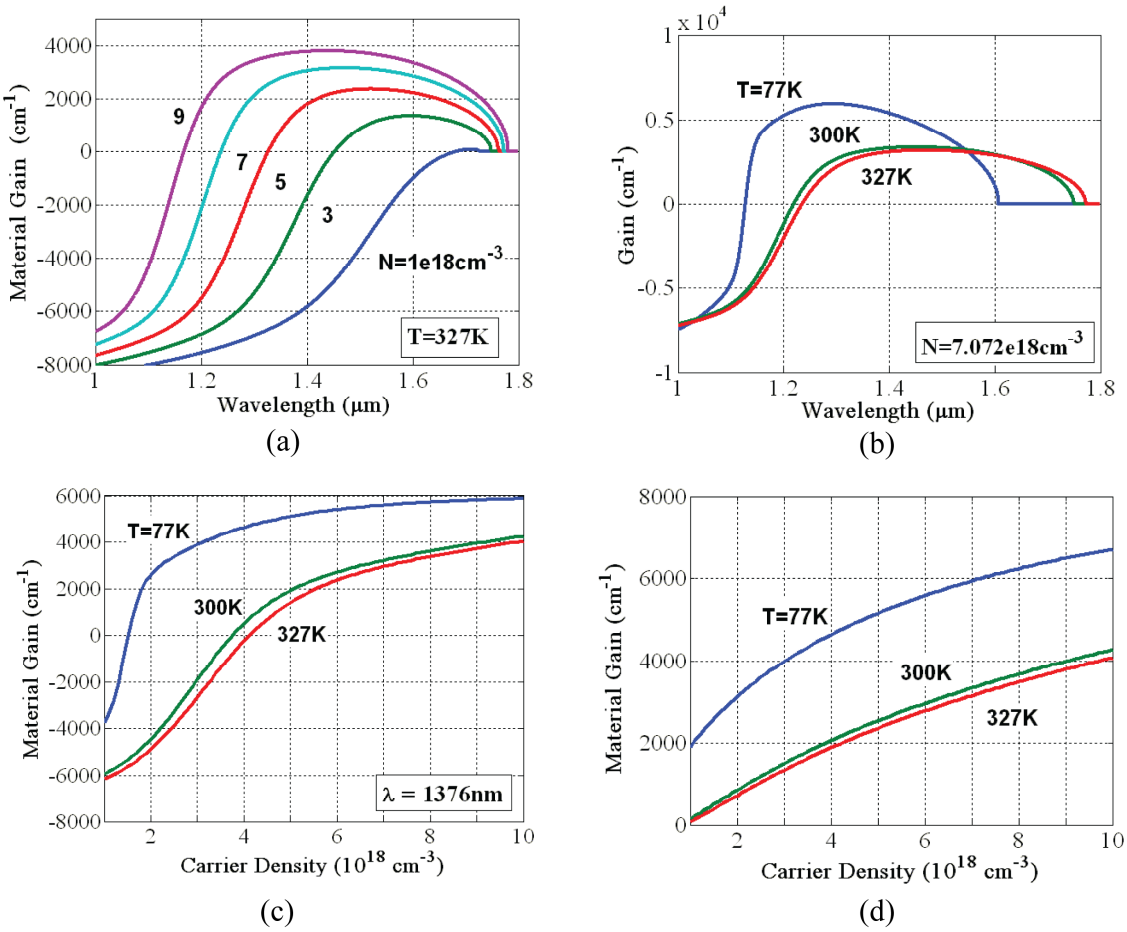

Figure 4.11: (a) Material gain spectrum at 327K, for a range of carrier densities. (b) Material gain spectrum at 0.5 mA injection current, corresponding to a carrier density of 7.072e18 cm^{-3}. (c) Material gain versus carrier density at the cavity resonance wavelength of 1376 nm. (d) Peak gain versus carrier density.

4.4 Discussion

In the preceding sections, we have summarized the temperature effects in semiconductor nanolasers, with focus on metal-clad nanolasers. The temperature effects can be explored in two paths: one path is through understanding the temperature

dependence of material properties, EM mode, Purcell factor F_p, as well as spontaneous emission factor β over a range of temperatures (77K–400K is considered in this review). The other path is through thermal management in device design and fabrication techniques, with the goal of achieving stable room temperature or higher temperature operation. This can be accomplished by choosing novel optically-low index and thermally-conductive materials, and considering the interplay of various design parameters including optical, electrical, thermal and material gain properties, which builds on the understanding of temperature effects in materials and EM nano-cavities.

Regarding thermal aspects of device design, we discussed techniques for simulating self-heating and heat dissipation in optically- and electrically-pumped nanolasers. We reviewed recent progress in the thermal simulation of nanolasers, including an example of a metallo-dielectric laser with α-Al_2O_3 shield. This example showed the importance of the interplay of thermal, optical, electrical, and material considerations, both for yielding insight into the key parameter limiting device performance, and to the validation of new nanolaser designs. Additionally, the analysis showed α-Al_2O_3 to be a promising shield material, enhancing metal-clad nanolaser heat dissipation through the shield, a previously-overlooked mechanism for nanolaser heat dissipation. The integrated analysis reveals that α-Al_2O_3's advantages become especially evident as the pedestal undercut depth increases and/or the device size decreases.

We note that, in the thermal management studies, the thermal conductivities used for α-Al_2O_3 represented a range of reported literature values. A 3-ω measurement can be conducted to obtain the thermal conductivity of α-Al_2O_3 deposited under specific ALD conditions, yielding the actual experimental value used for a given laser [127]. However,

the errors introduced by the two-dimensional heat spreading effect in the upper layer of the target film make this measurement non-trivial [128]. The precise determination of the heat conductivity of the deposited α-Al_2O_3, as well as the optimization of the α-Al_2O_3 deposition technique for increased thermal conductivity, would aid in the fabrication and analysis of future nanolasers. Recently, aluminum nitride (AlN) has emerged as an effective passivation material, when prepared by plasma-enhanced ALD [129]. With a higher thermal conductivity than α-Al_2O_3, AlN can be explored as an alternative shield material in the future.

Similar to that introduced for the more mature field of VCSELs [104], a self-consistent analysis of the interconnected dynamics of nanolaser thermal behavior would incorporate the above dependencies, yielding insights into the dynamic behavior of current nanolaser designs, as well as suggesting devices with new functionalities. In combination with recent fabrication advances [38, 108], we expect the exploration of thermal effects in nanolasers to enable a new generation of robust electrically-pumped nanolasers for room-temperature operation and above.

Chapter 4, in part, is a reprint of the material as it appears in Q. Gu, J. Shane, F. Vallini, B. Wingad, J. S. Smalley, N. C. Frateschi and Y. Fainman, "Amorphous Al_2O_3 shield for thermal management in electrically pumped metallo-dielectric nanolasers," *IEEE. J. Quantum. Electron.,* (Accepted). and Q. Gu, J. S. Smalley, J. Shane, O. Bondarenko and Y. Fainman, "Temperature effects in metal-clad semiconductor nanolasers," *Nanophotonics Journal*, (Accepted). And J. S. Smalley, Q. Gu and Y. Fainman, "Temperature dependence of the spontaneous emission factor in subwavelength

semiconductor lasers," *IEEE. J. Quantum. Electron.,* vol. 50, pp. 175-185, 2014. The dissertation author was the primary co-researcher and co-author.

Chapter 5

Conclusion and Future Directions

In this thesis, we have focused on the semiconductor nanolasers operating in the near-infrared frequency range, for applications in chip-scale photonic integrated circuits (PICs) that supplement electronic circuits in modern optical communication systems. As electromagnetically isolated, sub-wavelength sources of coherent light, metal-clad nanolasers make excellent candidates for integration into chip-scale photonic circuits. We have described the design, fabrication, characterization and analysis of metallo-dielectric [35, 36, 56] nanolasers, both optically and electrically pumped. In Chapter 2, we presented a QED-based model of the Purcell effect to quantify the quantum effects in nanoscale cavities [59]. The application of this model to an optically pumped metallo-dielectric nanolaser suggested that, the operating temperature can play a significant role in determining the spontaneous emission factor in nanolasers. Through analyzing the carrier saturation effects in the MQW gain medium of a metallo-dielectric nanopatch laser design in Chapter 3, we showed that the barrier between the QWs will be heavily pumped at carrier concentrations required for nanolaser operation. As a result, spontaneous emission from the barrier in low Q modes and/or undesired high Q modes with resonance wavelengths close to the barrier bandgap occurs. This behavior results in

competition for carriers between barriers and wells, and consequently, suppressed emission of the lasing mode. Therefore, although MQW has been successfully employed in mirco- and larger scale semiconductor lasers, bulk material may be a better choice for gain medium in nanolasers. In Chapter 4, by employing α-Al_2O_3, a thermally conductive dielectric material, and simultaneously optimizing various physical parameters in the nanolaser design, we showed that thermal heating can be well controlled in nanolasers.

The demonstration of thermally stable, electrically pumped nanolasers amenable to room temperature operation, however, is only the first step toward realizing chip-scale PICs. To fully integrate optical sources into PICs, the extraction of emitted light into optical waveguides on-chip is of great importance. Monolithic integration with existing material platform is crucial in ensuring chip-scale integration too. Ultra-dense arrays of individually-addressable metal-clad nanolasers can find a wide range of applications, such as in optical communications, sensing, and beam steering.

Other future research directions include the realization of high β-factor metallo-dielectric nanolasers and direct high-speed modulation of these lasers [10]. From a materials science point of view, gain material grown radially around nanowire cores can be explored to minimize non-radiative recombination inherent to non-ideal surfaces after the dry etching processes of fabrication [130]. Theoretical studies of linewidth behavior, photon statistics in sub-wavelength lasers, as well as emitter-field interaction in dissipative nanoscale systems are also of great interest [59]. In the following subsections, we will briefly discuss a few of the on-going and future research efforts.

5.1 Coupling between nanolasers and optical waveguides

The coupling of light from optical sources to waveguides helps to extract light in integrated circuits. In particular, out-coupling emitted light from nanolasers to single-mode silicon-on-insulator (SOI) waveguides can lead to on-chip integration of laser sources with silicon photonics technology [131, 132]. Generally speaking, because of the extremely small output apertures of nanolaser cavities, the radiation patterns of nanolasers tend to be very broad, and emitted light from the cavity diverges rapidly. Therefore, developing methods to efficiently couple light from nanolasers into optical waveguides is of great importance. To this end, the dielectric shielded nanopatch laser that we discussed in Chapter 3 was one of the first proposed devices to enhance the coupling efficiency by engineering the directional radiation pattern of the cavity mode. A 22% coupling efficiency is estimated for the nanopatch laser considered in Ref [89]. However, these nanopatch lasers are constructed on lossy metal substrate, consequently, integrating such lasers onto silicon platform poses difficulties. Recently, Kim et al. [133] proposed that, efficient out-coupling of light from metallo-dielectric nanolasers, such as those described in Chapter 4, into integrated Si waveguides positioned at the bottom of the nanolaser structures can be achieved [134]. This method relies on breaking the symmetry of the transverse electric (TE) mode of the cavity by manipulating the dielectric shield thickness. Nearly 90% efficiency is estimated in Ref [134]. Adding the waveguide coupling efficiency as another parameter into our integrated design procedure described in Chapter 4, efficiently out-coupled, low threshold and thermally stable metal-

clad nanolasers can be designed and realized. We believe that integrated nanolaser-waveguide devices will be important components in the next-generation on-chip optical communication systems.

5.2 Integration with silicon platform

The discussion in Section 5.1 shed some light on the importance of the integration of multiple devices. In terms of optical sources, we have focused on III-V-compound-semiconductor-based nanolasers that are advantageous for construction of active optical elements and logic devices, owing to III-V materials' direct energy bandgaps, covering a wide range of the spectrum, and their high carrier mobility. Besides lasers, III-V-material-based devices have found a wide range of applications, including optical switching, routing, modulation, and detection. On the other hand, silicon currently serves not only as a foundation for complementary metal–oxide–semiconductor (CMOS) technology, but also as a primary material for passive photonics, due to its numerous advantages for on-chip light transport [135]. For light generation, however, silicon is inferior to its III–V counterparts due to its indirect bandgap.

There are two approaches toward on-chip integration, namely, an entirely monolithic and a partial hybrid-monolithic approach. When it comes to entirely monolithic approach, despite the remarkable progress with growing epitaxial III-V semiconductor layers on silicon [136, 137], the dissimilar crystal structures of these materials make it extremely challenging to grow sufficiently large areas of III-V on Si for PIC manufacturing [138]. Recent lasing results from electrically pumped germanium lasers grown on silicon also offer a solution for directly grown lasers on a silicon

platform [139]. At present, however, the partial hybrid-monolithic approach offers a timely practical alternative.

Today most photonic circuits with active components are implemented via flip-chip bonding of independently fabricated active components to a silicon-based passive photonic circuit. This approach is complex, time consuming, and has tight alignment tolerances (<0.5μm) for a minimal (1dB per link) coupling loss for microscale components [140]. For nanoscale components, the alignment restriction becomes impractical. An alternative method is wafer bonding prior to the PIC nanofabrication, which is currently the most amenable for dense, large-scale hybrid-monolithic integration [132]. Among a number of existing wafer bonding techniques [141], plasma assisted wafer bonding has the advantages of scalability, low temperature operation, and directness [142]. It has already been successfully used to demonstrate a variety of SOI-compatible evanescent optoelectronic devices [132].

The plasma-assisted wafer bonding technique can be combined with a self-aligned fabrication approach [131], which requires a single resist mask to etch both III-V and silicon layers. This combination offers the benefit of simple, alignment-free fabrication, which is very important when device dimensions approach the alignment resolution limit of commercial mask aligners, as is the case with nanolasers and even microlasers. Using this combined approach, we have demonstrated a number of integrated light sources on silicon platform, including optically pumped metallo-dielectric nanolasers heterogeneously integrated with SiO_2 on Si [143], and compact optically pumped SOI-compatible III-V/Si distributed feedback (DFB) lasers with sidewall modulated Bragg

gratings [133]. The next step toward inserting electrically pumped metal-clad nanolasers into PICs is to fabricate these lasers in a wafer-bonded III-V/Si material platform.

5.3 Ultra-dense arrays of individually-addressable metal-clad nanolasers

By their nature, the optical output power of wavelength- and subwavelength-scale lasers is small relative to their more macroscopic counterparts. To increase the total output power, nanolasers may be grouped together in arrays where the modes of individual devices are coupled to form a supermode. Such coupled arrays have been demonstrated with photonic crystal lasers [144], metallic bowtie lasers [145], nanowire lasers [146], liquid crystal lasers [147], and nanoparticles lasers [148] acting as the individual elements. In addition to higher power, some coupled arrays may attain higher efficiency relative to the stand-alone element efficiency [144].

For applications in communications, sensing, and beam steering, however, un-coupled nanolaser arrays are desired. An uncoupled array of metal-clad nanolasers may contain four to five orders of magnitude more elements than a commercially available diode laser array and more elements than any existing array. While the output power of the individual element remains small compared to the total power of the entire array, individually addressable, decoupled elements are essential for creating independent channels for guided and freespace signal propagation [149]. Additionally, beam steering of a phased array necessitates individually addressable, uncoupled elements [150].

Because of their size, uncoupled nanolasers may be packed at enormous density, compared to their macroscopic counterparts. For example, the die of a state-of-the-art

commercially available 4x1 VCSEL array has a footprint of 1000 μm x 300 μm (0.3 mm^2), with a pitch of 250 μm between lasers. In comparison, a recent photonic crystal array used for live-cell imaging has a pitch of 5 μm [149]. This means that over 12,000 photonic crystal lasers may be placed in the same footprint of the 4 commercial VSCELs. This comparison is, however, unfair, because the mentioned photonic crystal lasers are optically pumped. The recently demonstrated nanophotonic phased array, on the other hand, is, like commercial VCSELs, electronically controlled. It contains over 4,000 elements in roughly the same footprint (0.33 mm^2) as that of the VCSELs [150].

Metal-clad nanolasers offer even greater packing density. The electrically-pumped laser of the previous section [36] has a diameter of 1.5 μm. If we assume a pitch of twice this length, then over 30,000 electronically controlled, metal-clad nanolasers could be placed in the same footprint as that of 4 commercial VCSELs. Such a densely packed array would be ideal for high-resolution imaging/sensing. Depending on their Purcell factors, metal-clad nanolasers may exhibit high relaxation bandwidths that make them suitable for transmitting, receiving, and processing information at the chip-scale. Large packing density combined with low power consumption and potentially fast operation make metal-clad nanolaser arrays strong candidates for light sources of future PICs. Other potential applications of these ultra-dense arrays include imaging of biological samples, trapping and manipulation of particles, and guided and free-space optical communication [149, 150].

Chapter 5, in part, is a reprint of the material as it appears in Q. Gu, J. S. Smalley, M. P. Nezhad, A. Simic, J. H. Lee, M. Katz, O. Bondarenko, B. Slutsky, A. Mizrahi, V.

Lomakin and Y. Fainman, "Subwavelength semiconductor lasers for dense chip-scale integration," *Advances in Optics and Photonics,* vol. 6, pp. 1-56, 2014. The dissertation author was the primary co-researcher and author.

Appendix A

A.1 Non-relativistic QED in free space and in a resonant cavity

Following the formalism of ([99]. §III.A.1), we begin the non-relativistic QED description of the electric field in free space and in a cavity by separating the longitudinal and transverse components of the electric field operator, $\hat{\boldsymbol{E}} = \hat{\boldsymbol{E}}_{\parallel} + \hat{\boldsymbol{E}}_{\perp}$. The longitudinal field operator $\hat{\boldsymbol{E}}_{\parallel}$ is fully determined by the charge distribution and describes the quasi-static field of charged particles. In what follows, we model electron-hole pairs in the gain material as two-level quantum systems, and cavity materials with their macroscopic permittivities ε; the model includes no charged particles. We therefore focus on the source-free condition and ignore $\hat{\boldsymbol{E}}_{\parallel}$. The transverse component of a free field is given by ([99]. §III.B.2).

$$\hat{\boldsymbol{E}}_{\perp}(\mathbf{r},t) = \sum_{\mathbf{k},\boldsymbol{\varepsilon}} \sqrt{\frac{\hbar\omega_{\mathbf{k}}}{2\varepsilon_0 L^3}}\, i\left(\hat{a}_{\mathbf{k},\boldsymbol{\varepsilon}}(t)\, e^{i\mathbf{k}\cdot\mathbf{r}} - \hat{a}^{\dagger}_{\mathbf{k},\boldsymbol{\varepsilon}}(t)\, e^{-i\mathbf{k}\cdot\mathbf{r}}\right)\boldsymbol{\varepsilon} \tag{1}$$

In Equation (1), the summation is over all free space modes, **k** is the wavevector of the mode, and **ε** is the polarization unit vector of the mode, satisfying $\boldsymbol{\varepsilon} \perp \mathbf{k}$. $\omega_{\mathbf{k}} = |\mathbf{k}|c$ is the mode frequency, L^3 is the quantization volume, $\hat{a}^{\dagger}_{\mathbf{k},\boldsymbol{\varepsilon}}(t)$ and $\hat{a}_{\mathbf{k},\boldsymbol{\varepsilon}}(t)$ are photon creation and annihilation operators for the mode, respectively, and

$$\hat{a}_{\mathbf{k},\boldsymbol{\varepsilon}}(t) = \hat{a}_{\mathbf{k},\boldsymbol{\varepsilon}}(0)\cdot e^{-i\omega_{\mathbf{k}}t}; \qquad \hat{a}^{\dagger}_{\mathbf{k},\boldsymbol{\varepsilon}}(t) = \hat{a}^{\dagger}_{\mathbf{k},\boldsymbol{\varepsilon}}(0)\cdot e^{i\omega_{\mathbf{k}}t} \tag{2}$$

where $\hat{a}(0)$ and $\hat{a}^{\dagger}(0)$ are the operator values at time t=0. Equations (1) and (2) are written for a free field in the Heisenberg picture, in which quantum states are constant and operators vary with time. They also apply in the Dirac picture for a field interacting with, for example, a two-level emitter if the interaction is included as correction to the un-perturbed Hamiltonian. In this situation, the quantum states evolve due to the interaction ([71]. §5.5). It is often convenient to separate Equation (1) into annihilation $\hat{\boldsymbol{E}}_{\perp}^{+}$ and creation $\hat{\boldsymbol{E}}_{\perp}^{-}$ terms,

$$\begin{aligned}
&\hat{\boldsymbol{E}}_{\perp}(\mathbf{r},t)=\hat{\boldsymbol{E}}_{\perp}^{+}(\mathbf{r},t)+\hat{\boldsymbol{E}}_{\perp}^{-}(\mathbf{r},t),\\
&\hat{\boldsymbol{E}}_{\perp}^{+}(\mathbf{r},t)=\sum_{\mathbf{k},\boldsymbol{\varepsilon}}\sqrt{\frac{\hbar\omega_{\mathbf{k}}}{2\varepsilon_0 L^3}}\,i\,\hat{a}_{\mathbf{k},\boldsymbol{\varepsilon}}(t)\,e^{i\mathbf{k}\cdot\mathbf{r}}\boldsymbol{\varepsilon},\\
&\hat{\boldsymbol{E}}_{\perp}^{-}(\mathbf{r},t)=\left(\hat{\boldsymbol{E}}_{\perp}^{+}(\mathbf{r},t)\right)^{\dagger}=-\sum_{\mathbf{k},\boldsymbol{\varepsilon}}\sqrt{\frac{\hbar\omega_{\mathbf{k}}}{2\varepsilon_0 L^3}}\,i\,\hat{a}_{\mathbf{k},\boldsymbol{\varepsilon}}^{\dagger}(t)\,e^{-i\mathbf{k}\cdot\mathbf{r}}\boldsymbol{\varepsilon}
\end{aligned} \tag{3}$$

An analogous representation exists for the electric field operator in a cavity [151, 152]. In a source-free cavity, the electric field operator becomes

$$\hat{\boldsymbol{E}}_{u}(\mathbf{r},t)=\hat{\boldsymbol{E}}_{u}^{+}(\mathbf{r},t)+\hat{\boldsymbol{E}}_{u}^{-}(\mathbf{r},t)=\sum_{\omega_k>0} i\sqrt{\hbar\omega_k}\left(\hat{a}_k(t)-\hat{a}_k^{\dagger}(t)\right)\cdot\boldsymbol{e}_k(\mathbf{r}) \tag{4}$$

where the summation is over all cavity modes and ω_{k} is the eigenfrequency of the mode *k*. In Equation (4), **r** is the location at which the field is evaluated, $\boldsymbol{e}_k(\mathbf{r})$ is the electric field modal profile normalized so that the mode energy evaluates to $\frac{1}{2}\hbar\omega_k\left(\hat{a}_k(t)\hat{a}_k^{\dagger}(t)+\hat{a}_k^{\dagger}(t)\hat{a}_k(t)\right)$, i.e., $\hbar\omega_k$ per quantum level of the harmonic oscillator and $\frac{1}{2}\hbar\omega_k$ in the oscillator ground state. Explicitly, in non-dispersive media,

$$\boldsymbol{e}_k(\mathbf{r})=\frac{\boldsymbol{E}_k(\mathbf{r})}{\sqrt{N_k}},\qquad N_k\equiv\int_V\left[\varepsilon(\mathbf{r})\boldsymbol{E}_k^2(\mathbf{r})+\mu(\mathbf{r})\boldsymbol{H}_k^2(\mathbf{r})\right]d^3\mathbf{r} \tag{5}$$

where N_k is the normalization factor for mode k and the integration is over the entire volume in space. $\boldsymbol{E}_k(\mathbf{r})$ and $\boldsymbol{H}_k(\mathbf{r})$ represent real cavity mode fields (solutions of the classical Maxwell's equations for the cavity geometry), and integration is over all space. In electrically dispersive but magnetically non-dispersive media, N_k becomes [48]

$$\begin{aligned} N_k &= \int_V \left[\left. \frac{\partial\left(\omega'\varepsilon_R(\mathbf{r},\omega')\right)}{\partial\omega'} \right|_{\omega'=\omega_k} \boldsymbol{E}_k^2(\mathbf{r}) + \mu(\mathbf{r})\boldsymbol{H}_k^2(\mathbf{r}) \right] d^3\mathbf{r} \\ &= \int_V \left[\left(\left. \frac{\partial\left(\omega'\varepsilon_R(\mathbf{r},\omega')\right)}{\partial\omega'} \right|_{\omega'=\omega_k} + \varepsilon_R(\mathbf{r},\omega_k) \right) \boldsymbol{E}_k^2(\mathbf{r}) \right] d^3\mathbf{r} \end{aligned} \tag{6}$$

where ε_R stands for the real part of permittivity ε. The assumed, non-dispersive magnetic permeability enables us to express the total magnetic energy in Equation (6) in terms of the electric field [152]. Although ε_R may be negative in some metallic materials, the integral in Equation (6) is always positive. Note that the preceding formalism lacks the imaginary part of the permittivity, and therefore ignores damping in the cavity. Damping may be introduced using Heisenberg-Langevin reservoir theory ([64]. §9). We discuss such an approach to damping in the rest of this section.

When the electromagnetic mode interacts with the environment, the time dependence of $\hat{a}_k(t)$ and $\hat{a}_k^\dagger(t)$ can no longer be described by Equation (2). A damping environment can often be modeled as a thermal reservoir. The reservoir model is applicable when the interaction is weak and the environment is a large stochastic system that satisfies the Markovian approximation, namely, a system that over a short time $\tau_{\text{reservoir}}$ becomes fully disordered and loses all memory of its earlier state. Intuitively, the interaction must be sufficiently weak and the reservoir characteristic time $\tau_{\text{reservoir}}$ sufficiently short, so the mode experiences all possible states of the reservoir in equal

measure. We employ the reservoir formalism to describe loss at the boundary of the cavity. Hereafter the terms environment and reservoir are used interchangeably.

When a mode interacts with a thermal reservoir, the evolution of the mode operators $\hat{a}_k(t)$ and $\hat{a}_k^\dagger(t)$ also becomes stochastic. As a result, only statistical correlations involving $\hat{a}_k(t)$ and $\hat{a}_k^\dagger(t)$ can be predicted for each mode. The correlations obey [64]

$$\begin{aligned}\frac{d}{dt}\left[\hat{a}_k^\dagger(t)\hat{a}_k(t+\tau)\right]_R &= -\mathrm{C}_k\left[\hat{a}_k^\dagger(t)\hat{a}_k(t+\tau)\right]_R + \mathrm{C}_k\bar{n}(\omega_k)e^{-\frac{1}{2}\mathrm{C}_k|\tau|}e^{-i\omega_k\tau}\\ \frac{d}{dt}\left[\hat{a}_k(t)\hat{a}_k^\dagger(t+\tau)\right]_R &= -\mathrm{C}_k\left[\hat{a}_k(t)\hat{a}_k^\dagger(t+\tau)\right]_R + \mathrm{C}_k\left(\bar{n}(\omega_k)+1\right)e^{-\frac{1}{2}\mathrm{C}_k|\tau|}e^{i\omega_k\tau}\end{aligned} \tag{7}$$

where $[\cdots]_R$ denotes the statistical expected value, and $\bar{n}(\omega_k)$ represents the reservoir energy at frequency ω_k. In Equation (7), C_k is the mode-reservoir coupling constant, thus $1/C_k$ represents the cavity damping time. The expected value $\left[\hat{a}_k^\dagger(t)\hat{a}_k(t)\right]_R$ of the photon count decays exponentially with the damping constant $1/C_k$ toward its steady state value $\bar{n}(\omega_k)$, which is usually referred to as the reservoir temperature. Comparing the reservoir characteristic time $\tau_{\text{reservoir}}$ with the cavity damping time, the mode-reservoir weak coupling condition is $\tau_{\text{reservoir}} << 1/C_k$. After time $t >> 1/C_k$, the evolution of the correlation, which is described by Equation (7), reaches steady state, with its behavior described by Equation (8) below.

$$\begin{aligned}\left[\hat{a}_k^\dagger(t)\hat{a}_k(t+\tau)\right]_R &= \bar{n}(\omega_k)e^{-\frac{1}{2}C_k|\tau|}e^{-i\omega_k\tau}\\ \left[\hat{a}_k(t)\hat{a}_k^\dagger(t+\tau)\right]_R &= \left(\bar{n}(\omega_k)+1\right)e^{-\frac{1}{2}C_k|\tau|}e^{i\omega_k\tau}\end{aligned} \tag{8}$$

Once mode-reservoir equilibrium has been reached, the correlations on the left hand side of Equation (8) are fully determined by C_k and $\bar{n}(\omega_k)$.

We next introduce the interaction between the electromagnetic field and a two-level emitter, such as an electron-hole pair in a semiconductor laser. Suppose the emitter is prepared at time $t=t_0$ in its upper state |2>. The emitter interacts with the electromagnetic field mode, and the two become quantum mechanically entangled. At some later time $t > t_0$, a phase-destroying event occurs, e.g., a collision between two electrons in the conduction band of semiconductors [70]. Such an event either makes the emitter transition to the lower state |1> while simultaneously adding a photon of frequency ω_{21} to the field, or leaves the emitter in the upper state |2> and the mode with its original photon count. The emitter-mode interaction then begins anew and continues until the next phase-destroying event occurs. When such events are much more frequent than level transitions (transitions between states), the photonemission probability between time t_0 and a later time $t > t_0$ is small and is given by [153]

$$P_{2\to 1,i}(t) = \frac{1}{\hbar^2}\int_{t_0}^{t_0+\tau_{coll}}\int_{t_0}^{t_0+\tau_{coll}}\int e^{-i\omega_{21}(t''-t')}\langle i|\left(\wp^*_{12}(\omega_{21})\cdot\hat{\mathbf{E}}^+_\perp(\mathbf{r},t')\right)\cdot\left(\wp_{12}(\omega_{21})\cdot\hat{\mathbf{E}}^-_\perp(\mathbf{r},t'')\right)|i\rangle D(\omega_{21})\,d\omega_{21}dt'dt'' \tag{9}$$

where $|i\rangle$ is the initial state of the field, and $\wp_{12}(\omega_{21})$ is the dipole matrix element. $\wp_{12}(\omega_{21})$ is a property of the emitter and determines the potential strength of the emitter-mode interaction ([74]. §4.3). The actual interaction strength depends on the orientation of the dipole relative to the electric field and is thus governed by the dot product between the two. $D(\omega_{21})$ is the density of emitter states, which characterizes the inhomogeneity of the system ($D(\omega_{21}) = \delta(\omega_{21} - \bar{\omega}_{21})$ if all emitters are identical with natural frequency $\bar{\omega}_{21}$). Equation (9) is valid over time intervals short enough such that $P_{2\to 1}(t) << 1$. This condition, known as the emitter-mode weak coupling regime, is met in semiconductors

owing to fast phase-destroying intraband collisions, which occur with characteristic frequency $1/\tau_{coll} \sim (0.3ps)^{-1}$ at room temperature [70, 81]. The photonemission rate is generally much lower, except under very strong applied field and/or very strong spontaneous emission enhancement [7, 154]. The opposite limit is the strong-coupling regime, in which neither the emitter nor the field mode experience dephasing events that are more frequent than level transitions; in this situation, Equation (9) does not apply, and Rabi oscillations result instead [7, 155, 156]. In this paper, however, we focus on the emitter-mode weak-coupling regime. Equation (9) is therefore employed throughout and evaluated at times $t = t_0 + \tau_{coll}$ when, on average, the next phase-destroying collision is expected to occur. To obtain emission probability in free space and in cavities, we evaluate Equation (9) with the transverse electric field operator of the respective condition.

A.2 Spontaneous Emission probability in free space and in a resonant cavity

It can be shown from Equation (9) that photonemission still takes place, with a well-defined probability, even when the mode is in the vacuum state $|0\rangle$; this is referred to as spontaneous emission. We apply Equation (9) in free space, with all free space modes in the vacuum state and no reservoir present. The field operators in this case have deterministic time dependences described by Equation (2). By substituting Equations (1) and (2) into Equation (9), we recover the Weisskopf-Wigner probability of spontaneous emission in the limit of a 2-level system when $D(\omega_{21}) = \delta(\omega-\omega_{21})$ [157],

$$P^{free}_{2\to 1,|0\ldots 0\rangle} = \frac{1}{\hbar^2}\int_{t_0}^{t_0+\tau_{coll}}\int_{t_0}^{t_0+\tau_{coll}} e^{-i\omega_{21}(t''-t')}\langle 0\ldots 0|\left(\boldsymbol{\wp}^{*}_{12}(\omega_{21})\cdot\sum_{\mathbf{k}',\boldsymbol{\varepsilon}'}\sqrt{\frac{\hbar\omega_{\mathbf{k}'}}{2\varepsilon_0 L^3}}\boldsymbol{\varepsilon}'\hat{a}_{\mathbf{k}',\boldsymbol{\varepsilon}'}(t')e^{i\mathbf{k}'\cdot\mathbf{r}_e}\right)\times$$
$$\left(\boldsymbol{\wp}_{12}(\omega_{21})\cdot\sum_{\mathbf{k}'',\boldsymbol{\varepsilon}''}\sqrt{\frac{\hbar\omega_{\mathbf{k}''}}{2\varepsilon_0 L^3}}\boldsymbol{\varepsilon}''\hat{a}^{\dagger}_{\mathbf{k}'',\boldsymbol{\varepsilon}''}(t'')e^{-i\mathbf{k}''\cdot\mathbf{r}_e}\right)|0\ldots 0\rangle D(\omega_{21})\,d\omega_{21}dt'dt'' \qquad (10)$$
$$= \sum_{\mathbf{k},\boldsymbol{\varepsilon}}\frac{\omega_{\mathbf{k}}}{2\hbar\varepsilon_0 L^3}\int\left|\boldsymbol{\wp}_{12}(\omega_{21})\cdot\boldsymbol{\varepsilon}\right|^2 D(\omega_{21})R(\omega_{\mathbf{k}}-\omega_{21},\tau_{coll})\,d\omega_{21}$$
$$\approx \int\frac{\omega_{21}^3}{3\pi\hbar\varepsilon_0 c^3}\tau_{coll}\left|\boldsymbol{\wp}_{12}(\omega_{21})\right|^2 D(\omega_{21})\,d\omega_{21}$$

In Equation (10), $\mathbf{r}_e$ is the location of the emitter, and summation cross-terms cancel owing to $\langle 0\ldots 0|\hat{a}_{\mathbf{k}',\boldsymbol{\varepsilon}'}\hat{a}^{\dagger}_{\mathbf{k}'',\boldsymbol{\varepsilon}''}|0\ldots 0\rangle = \delta_{\mathbf{k}\mathbf{k}'}\delta_{\boldsymbol{\varepsilon}'\boldsymbol{\varepsilon}''}$. The quantity $\mathrm{R}(\omega-\omega_{21},\tau_{coll}) \equiv \int_{t_0}^{t_0+\tau_{coll}}\int_{t_0}^{t_0+\tau_{coll}} e^{-i(\omega-\omega_{21})(t''-t')}dt'dt'' = \left|\frac{\sin\left[\frac{1}{2}(\omega-\omega_{21})\tau_{coll}\right]}{\frac{1}{2}(\omega-\omega_{21})}\right|^2$, which absorbs the time exponents inserted from Equation (2), is the homogeneous broadening function and depends on τ_{coll}. Viewed as a function of ω, $R(\omega-\omega_{21},\tau_{coll})$ peaks at ω_{21}, has a width on the order of $1/\tau_{coll}$, and satisfies $\int R(\omega-\omega_{21},\tau_{coll})\,d\omega = 2\pi\cdot\tau_{coll}$ [71]. The approximation in Equation (10) consists in replacing the summation over free space modes $\mathbf{k}$ with appropriate integration and then taking $\omega_{\mathbf{k}}\approx\omega_{21}$. Such an approximation is justified because the free space modes form a continuum with an infinitesimal spectral spacing between adjacent modes, and the quantity ω_k^3 varies little over the width of $R(\omega-\omega_{21},\tau_{coll})$.

A similar procedure can be carried out in an undamped cavity if all cavity modes are initially in vacuum state. Applying Equation (4) to Equation (9), summation cross-terms cancel again according to $\langle 0\ldots 0|\hat{a}_{k'}\hat{a}^{\dagger}_{k''}|0\ldots 0\rangle = \delta_{k'k''}$, and we obtain

$$P^{cav}_{2\to 1,|0\ldots 0\rangle} = \sum_k\frac{\omega_k}{\hbar}\int\left|\boldsymbol{\wp}_{12}(\omega_{21})\cdot\boldsymbol{e}_k(\mathbf{r}_e)\right|^2 D(\omega_{21})R(\omega_k-\omega_{21},\tau_{coll})\,d\omega_{21} \qquad (11)$$

Unlike in free space, the summation over modes k in Equation (11) cannot be replaced with integration if the spectral spacing between adjacent modes is non-

negligible. This is especially the case in micro- and nano- cavities in which the spacing between adjacent modes may be a significant fraction of the modes' resonance frequencies. The cavity spontaneous emission probability given by Equation (11) may depend significantly on the number of available modes and their location relative to the density of emitter states $D(\omega_{21})$. It also depends on the location and orientation of the emitter relative to the normalized mode field $\boldsymbol{e}_k(\mathbf{r})$. For example, the probability is zero for an emitter located at a field node.

A.3 Discussions

Consistent application of the theory reveals that some of the intuitions and commonly used formulae originally derived for gas or quantum dot lasers do not carry over to bulk and MQW semiconductor lasers. Two observations are of particular importance.

First, the Purcell factor is often thought to scale as $Q/(V_a/\Gamma_k)$, the ratio of cavity Q to the mode volume V_a/Γ_k. In bulk and MQW semiconductors, however, inhomogeneous and homogeneous broadenings typically overwhelm the cavity linewidth, and consequently cavity Q has negligible effect on the spontaneous emission rate. In nanocavities where the cavity modes are sparse and radiation out of the cavity is weak, homogeneous and inhomogeneous broadenings also result in much lower overall spontaneous emission rates than might be the case if all emitters exactly matched the cavity resonance.

Second, in the present model the field-reservoir interaction ($\hat{H}_{FR}$ in Equation (2.3)) includes only losses at the cavity boundary in the form of radiation output and loss through cavity walls. It does not include interaction of the field with the gain material, apart from the single emitter under immediate consideration, which is accounted for in Equation (2.3) by the terms $\hat{H}_A$ and $\hat{H}_{AF}$. Consequently, the mode damping constant C_k in Equation (8), and the Lorentzian $L_k(\omega)$ in Equation (2.9), describe only cavity wall and radiation loss, and must be computed for a hypothetical structure in which the gain medium (with complex permittivity) is replaced with a transparent medium (with purely real permittivity). Most authors who report estimates of Purcell factor use the same approach [7, 35, 66-69].

References

[1] S. I. Bozhevolnyi, *Plasmonic Nanoguides and Circuits.* Pan Stanford Publ., 2008.

[2] T. H. Maiman, "Stimulated optical radiation in ruby," 1960.

[3] E. M. Purcell, "Spontaneous emission probabilities at radio frequencies," *Phys. Rev.,* vol. 69, pp. 681, 1946.

[4] H. Yokoyama and S. Brorson, "Rate equation analysis of microcavity lasers," *J. Appl. Phys.,* vol. 66, pp. 4801-4805, 1989.

[5] H. Yokoyama, K. Nishi, T. Anan, H. Yamada, S. Brorson and E. Ippen, "Enhanced spontaneous emission from GaAs quantum wells in monolithic microcavities," *Appl. Phys. Lett.,* vol. 57, pp. 2814-2816, 1990.

[6] Y. Yamamoto, S. Machida and G. Björk, "Microcavity semiconductor laser with enhanced spontaneous emission," *Phys. Rev. A,* vol. 44, pp. 657, 1991.

[7] J. M. Gérard and B. Gayral, "Strong Purcell effect for InAs quantum boxes in three-dimensional solid-state microcavities," *J. Lightwave Technol.,* vol. 17, pp. 2089-2095, 1999.

[8] E. K. Lau, A. Lakhani, R. S. Tucker and M. C. Wu, "Enhanced modulation bandwidth of nanocavity light emitting devices," *Opt. Express,* vol. 17, pp. 7790-7799, 2009.

[9] C. A. Ni and S. L. Chuang, "Theory of high-speed nanolasers and nanoLEDs," *Opt. Express,* vol. 20, pp. 16450-16470, 2012.

[10] T. Suhr, N. Gregersen, K. Yvind and J. Mørk, "Modulation response of nanoLEDs and nanolasers exploiting Purcell enhanced spontaneous emission," *Opt. Express,* vol. 18, pp. 11230-11241, 2010.

[11] B. Ellis, M. A. Mayer, G. Shambat, T. Sarmiento, J. Harris, E. E. Haller and J. Vučković, "Ultralow-threshold electrically pumped quantum-dot photonic-crystal nanocavity laser," *Nat. Photonics,* vol. 5, pp. 297-300, 2011.

[12] P. Bhattacharya, B. Xiao, A. Das, S. Bhowmick and J. Heo, "Solid State Electrically Injected Exciton-Polariton Laser," *Phys. Rev. Lett.,* vol. 110, pp. 206403, 2013.

[13] S. Noda, "Seeking the Ultimate Nanolaser," *Science,* vol. 314, pp. 260, 2006.

[14] M. Khajavikhan, A. Simic, M. Katz, J. Lee, B. Slutsky, A. Mizrahi, V. Lomakin and Y. Fainman, "Thresholdless nanoscale coaxial lasers," *Nature,* vol. 482, pp. 204-207, 2012.

[15] G. Björk, A. Karlsson and Y. Yamamoto, "Definition of a laser threshold," *Phys. Rev. A,* vol. 50, pp. 1675, 1994.

[16] C. Ning, "What is Laser Threshold?" *IEEE J. Sel. Top. Quantum Electron.,* 2013.

[17] J. S. Smalley, Q. Gu and Y. Fainman, "Temperature Dependence of the Spontaneous Emission Factor in Subwavelength Semiconductor Lasers," *IEEE. J. Quantum. Electron.,* vol. 50, pp. 175-185, 2014.

[18] S. McCall, A. Levi, R. Slusher, S. Pearton and R. Logan, "Whispering-gallery mode microdisk lasers," *Appl. Phys. Lett.,* vol. 60, pp. 289-291, 1992.

[19] D. J. Gargas, M. C. Moore, A. Ni, S. Chang, Z. Zhang, S. Chuang and P. Yang, "Whispering gallery mode lasing from zinc oxide hexagonal nanodisks," *ACS Nano,* vol. 4, pp. 3270-3276, 2010.

[20] J. Hofrichter, O. Raz, L. Liu, G. Morthier, F. Horst, P. Regreny, T. De Vries, H. J. Dorren and B. J. Offrein, "All-optical wavelength conversion using mode switching in InP microdisc laser," *Electron. Lett.,* vol. 47, pp. 927-929, 2011.

[21] Q. Song, H. Cao, S. Ho and G. Solomon, "Near-IR subwavelength microdisk lasers," *Appl. Phys. Lett.,* vol. 94, pp. 061109-061109-3, 2009.

[22] O. Painter, R. Lee, A. Scherer, A. Yariv, J. O'brien, P. Dapkus and I. Kim, "Two-dimensional photonic band-gap defect mode laser," *Science,* vol. 284, pp. 1819-1821, 1999.

[23] Y. Akahane, T. Asano, B. Song and S. Noda, "High-Q photonic nanocavity in a two-dimensional photonic crystal," *Nature,* vol. 425, pp. 944-947, 2003.

[24] A. C. Scofield, S. Kim, J. N. Shapiro, A. Lin, B. Liang, A. Scherer and D. L. Huffaker, "Bottom-up photonic crystal lasers," *Nano Lett.,* vol. 11, pp. 5387-5390, 2011.

[25] C. Chen, C. Chiu, S. Chang, M. Shih, M. Kuo, J. Huang, H. Kuo, S. Chen, L. Lee and M. Jeng, "Large-area ultraviolet GaN-based photonic quasicrystal laser with high-efficiency green color emission of semipolar {10-11} In 0.3 Ga 0.7 N/GaN multiple quantum wells," *Appl. Phys. Lett.,* vol. 102, pp. 011134-011134-4, 2013.

[26] R. F. Oulton, V. J. Sorger, T. Zentgraf, R. M. Ma, C. Gladden, L. Dai, G. Bartal and X. Zhang, "Plasmon lasers at deep subwavelength scale," *Nature,* vol. 461, pp. 629-632, 2009.

[27] Y. Lu, J. Kim, H. Chen, C. Wu, N. Dabidian, C. E. Sanders, C. Wang, M. Lu, B. Li and X. Qiu, "Plasmonic nanolaser using epitaxially grown silver film," *Science,* vol. 337, pp. 450-453, 2012.

[28] C. Lin, J. Wang, C. Chen, K. Shen, D. Yeh, Y. Kiang and C. Yang, "A GaN photonic crystal membrane laser," *Nanotechnology,* vol. 22, pp. 025201, 2011.

[29] S. Arai, N. Nishiyama, T. Maruyama and T. Okumura, "GaInAsP/InP membrane lasers for optical interconnects," *IEEE J. Sel. Top. Quantum Electron.,* vol. 17, pp. 1381-1389, 2011.

[30] W. Zhou and Z. Ma, "Breakthroughs in Nanomembranes and Nanomembrane Lasers," *IEEE Photon. J.,* vol. 5, 2013.

[31] Z. Wang, B. Tian and D. VanThourhout, "Design of a Novel Micro-Laser Formed by Monolithic Integration of a III-V Pillar With a Silicon Photonic Crystal Cavity," *J. Lightwave Technol.,* vol. 31, pp. 1475-1481, 2013.

[32] J. Lin, Y. Huang, Q. Yao, X. Lv, Y. Yang, J. Xiao and Y. Du, "InAlGaAs/InP cylinder microlaser connected with two waveguides," *Electron. Lett.,* vol. 47, pp. 929-930, 2011.

[33] F. Albert, C. Hopfmann, A. Eberspacher, F. Arnold, M. Emmerling, C. Schneider, S. Hofling, A. Forchel, M. Kamp and J. Wiersig, "Directional whispering gallery mode emission from Limaçon-shaped electrically pumped quantum dot micropillar lasers," *Appl. Phys. Lett.,* vol. 101, pp. 021116-021116-4, 2012.

[34] M. T. Hill, Y. S. Oei, B. Smalbrugge, Y. Zhu, T. De Vries, P. J. van Veldhoven, F. W. M. van Otten and T. J. Eijkemans, "Lasing in metallic-coated nanocavities," *Nat. Photonics,* vol. 1, pp. 589-594, 2007.

[35] M. P. Nezhad, A. Simic, O. Bondarenko, B. Slutsky, A. Mizrahi, L. Feng, V. Lomakin and Y. Fainman, "Room-temperature subwavelength metallo-dielectric lasers," *Nat. Photonics,* vol. 4, pp. 395-399, 2010.

[36] J. H. Lee, M. Khajavikhan, A. Simic, Q. Gu, O. Bondarenko, B. Slutsky, M. P. Nezhad and Y. Fainman, "Electrically pumped sub-wavelength metallo-dielectric pedestal pillar lasers," *Opt. Express,* vol. 19, pp. 21524-21531, 2011.

[37] K. Ding, M. Hill, Z. Liu, L. Yin, P. van Veldhoven and C. Ning, "Record performance of electrical injection sub-wavelength metallic-cavity semiconductor lasers at room temperature," *Opt. Express,* vol. 21, pp. 4728-4733, 2013.

[38] Q. Gu, J. Shane, F. Vallini, B. Wingad, J. S. Smalley, N. C. Frateschi and Y. Fainman, "Amorphous Al2O3 shield for thermal management in electrically pumped metallo-dielectric nanolasers," *IEEE. J. Quantum. Electron.,* accepted.

[39] R. Hall, G. Fenner, J. Kingsley, T. Soltys and R. Carlson, "Coherent Light Emission from Ga-As Junctions," *Phys. Rev. Lett.,* vol. 9, pp. 366, 1962.

[40] H. Soda, K. Iga, C. Kitahara and Y. Suematsu, "GaInAsP/InP surface emitting injection lasers," *Japanese Journal of Applied Physics,* vol. 18, pp. 2329-2330, 1979.

[41] F. Albert, T. Braun, T. Heindel, C. Schneider, S. Reitzenstein, S. Hofling, L. Worschech and A. Forchel, "Whispering gallery mode lasing in electrically driven quantum dot micropillars," *Appl. Phys. Lett.,* vol. 97, pp. 101108-101108-3, 2010.

[42] V. Sandoghdar, F. Treussart, J. Hare, V. Lefevre-Seguin, J. Raimond and S. Haroche, "Very low threshold whispering-gallery-mode microsphere laser," *Physical Review-Section A-Atomic Molecular and Optical Physics,* vol. 54, pp. R1777, 1996.

[43] A. Imamog, R. Ram, S. Pau and Y. Yamamoto, "Nonequilibrium condensates and lasers without inversion: Exciton-polariton lasers," *Physical Review A,* vol. 53, pp. 4250, 1996.

[44] C. Schneider, A. Rahimi-Iman, N. Y. Kim, J. Fischer, I. G. Savenko, M. Amthor, M. Lermer, A. Wolf, L. Worschech and V. D. Kulakovskii, "An electrically pumped polariton laser," *Nature,* vol. 497, pp. 348-352, 2013.

[45] H. Deng, G. Weihs, C. Santori, J. Bloch and Y. Yamamoto, "Condensation of semiconductor microcavity exciton polaritons," *Science,* vol. 298, pp. 199-202, 2002.

[46] A. A. High, J. R. Leonard, A. T. Hammack, M. M. Fogler, L. V. Butov, A. V. Kavokin, K. L. Campman and A. C. Gossard, "Spontaneous coherence in a cold exciton gas," *Nature,* vol. 483, pp. 584-588, 2012.

[47] Y. Ma, X. Guo, X. Wu, L. Dai and L. Tong, "Semiconductor nanowire lasers," *Advances in Optics and Photonics,* vol. 5, pp. 216-273, 2013.

[48] S. W. Chang and S. L. Chuang, "Fundamental formulation for plasmonic nanolasers," *IEEE. J. Quantum. Electron.,* vol. 45, pp. 1014-1023, 2009.

[49] D. Li and C. Ning, "Giant modal gain, amplified surface plasmon-polariton propagation, and slowing down of energy velocity in a metal-semiconductor-metal structure," *Physical Review B,* vol. 80, pp. 153304, 2009.

[50] D. Li and C. Ning, "Peculiar features of confinement factors in a metal-semiconductor waveguide," *Appl. Phys. Lett.,* vol. 96, pp. 181109, 2010.

[51] A. Maslov and C. Ning, "Reflection of guided modes in a semiconductor nanowire laser," *Appl. Phys. Lett.,* vol. 83, pp. 1237-1239, 2003.

[52] M. I. Stockman, "Nanoplasmonics: past, present, and glimpse into future," *Optics Express,* vol. 19, pp. 22029-22106, 2011.

[53] M. P. Nezhad, K. Tetz and Y. Fainman, "Gain assisted propagation of surface plasmon polaritons on planar metallic waveguides," *Opt. Express,* vol. 12, pp. 4072-4079, 2004.

[54] M. T. Hill, M. Marell, E. S. Leong, B. Smalbrugge, Y. Zhu, M. Sun, P. J. van Veldhoven, E. J. Geluk, F. Karouta and Y. Oei, "Lasing in metal-insulator-metal sub-wavelength plasmonic waveguides," *Opt. Express,* vol. 17, pp. 11107-11112, 2009.

[55] D. J. Bergman and M. I. Stockman, "Surface plasmon amplification by stimulated emission of radiation: quantum generation of coherent surface plasmons in nanosystems," *Phys. Rev. Lett.,* vol. 90, pp. 027402, 2003.

[56] A. Mizrahi, V. Lomakin, B. A. Slutsky, M. P. Nezhad, L. Feng and Y. Fainman, "Low threshold gain metal coated laser nanoresonators," *Opt. Lett.,* vol. 33, pp. 1261-1263, 2008.

[57] P. Yeh, A. Yariv and E. Marom, "Theory of Bragg fiber," *J. Opt. Soc. Am.,* vol. 68, pp. 1196-1201, 1978.

[58] S. Strauf and F. Jahnke, "Single quantum dot nanolaser," *Laser & Photonics Reviews,* vol. 5, pp. 607-633, 2011.

[59] Q. Gu, B. Slutsky, F. Vallini, J. S. Smalley, M. P. Nezhad, N. C. Frateschi and Y. Fainman, "Purcell effect in sub-wavelength semiconductor lasers," *Opt. Express,* vol. 21, pp. 15603-15617, 2013.

[60] H. Walther, "Experiments on cavity quantum electrodynamics," *Phys. Rep.,* vol. 219, pp. 263-281, 1992.

[61] P. R. Berman, "Cavity quantum electrodynamics," 1994.

[62] C. Sauvan, J. Hugonin, I. Maksymov and P. Lalanne, "Theory of the Spontaneous Optical Emission of Nanosize Photonic and Plasmon Resonators," *Phys. Rev. Lett.,* vol. 110, pp. 237401, 2013.

[63] G. P. Agrawal and N. A. Olsson, "Self-phase modulation and spectral broadening of optical pulses in semiconductor laser amplifiers," *IEEE. J. Quantum. Electron.,* vol. 25, pp. 2297-2306, 1989.

[64] M. O. Scully and M. S. Zubairy, *Quantum Optics.* Cambridge, U.K: Cambridge University, 1997.

[65] H. J. Carmichael, *Statistical Methods in Quantum Optics 1: Master Equations and Fokker-Planck Equations.* Berlin: Springer-Verlag, 1999.

[66] A. Meldrum, P. Bianucci and F. Marsiglio, "Modification of ensemble emission rates and luminescence spectra for inhomogeneously broadened distributions of quantum dots coupled to optical microcavities," *Opt. Express,* vol. 18, pp. 10230-10246, 2010.

[67] T. Baba, D. Sano, K. Nozaki, K. Inoshita, Y. Kuroki and F. Koyama, "Observation of fast spontaneous emission decay in GaInAsP photonic crystal point defect nanocavity at room temperature," *Appl. Phys. Lett.,* vol. 85, pp. 3989-3991, 2004.

[68] H. Ryu and M. Notomi, "Enhancement of spontaneous emission from the resonant modes of a photonic crystal slab single-defect cavity," *Opt. Lett.,* vol. 28, pp. 2390-2392, 2003.

[69] H. Iwase, D. Englund and J. Vučković, "Analysis of the Purcell effect in photonic and plasmonic crystals with losses," *Opt. Express,* vol. 18, pp. 16546-16560, 2010.

[70] M. Asada, "Intraband relaxation time in quantum-well lasers," *IEEE. J. Quantum. Electron.,* vol. 25, pp. 2019-2026, 1989.

[71] J. J. Sakurai, *Modern Quantum Mechanics.* Reading, MA: Addison-Wesley, 1994.

[72] M. Fujita, A. Sakai and T. Baba, "Ultrasmall and ultralow threshold GaInAsP-InP microdisk injection lasers: design, fabrication, lasing characteristics, and spontaneous emission factor," *IEEE J. Sel. Top. Quantum Electron.,* vol. 5, pp. 673-681, 1999.

[73] H. Altug, D. Englund and J. Vučković, "Ultrafast photonic crystal nanocavity laser," *Nat. Physics,* vol. 2, pp. 484-488, 2006.

[74] L. A. Coldren and S. W. Corzine, *Diode Lasers and Photonic Integrated Circuits.* New York: John Wiley & Sons, inc., 1995.

[75] M. Glauser, G. Rossbach, G. Cosendey, J. Levrat, M. Cobet, J. Carlin, J. Besbas, M. Gallart, P. Gilliot and R. Butté, "Investigation of InGaN/GaN quantum wells for polariton laser diodes," *Phys. Status Solidi C,* vol. 9, pp. 1325-1329, 2012.

[76] M. Yamada and Y. Suematsu, "Analysis of gain suppression in undoped injection lasers," *J. Appl. Phys.,* vol. 52, pp. 2653-2664, 1981.

[77] M. Yamanishi and Y. Lee, "Phase dampings of optical dipole moments and gain spectra in semiconductor lasers," *IEEE. J. Quantum. Electron.,* vol. 23, pp. 367-370, 1987.

[78] S. R. Chinn, P. Zory Jr and A. R. Reisinger, "A model for GRIN-SCH-SQW diode lasers," *IEEE. J. Quantum. Electron.,* vol. 24, pp. 2191-2214, 1988.

[79] A. Yariv and P. Yeh, *Photonics: Optical Electronics in Modern Communications.* New York: Oxford University, 2007.

[80] B. Deveaud, F. Clerot, N. Roy, K. Satzke, B. Sermage and D. Katzer, "Enhanced radiative recombination of free excitons in GaAs quantum wells," *Phys. Rev. Lett.,* vol. 67, pp. 2355-2358, 1991.

[81] T. Baba and D. Sano, "Low-threshold lasing and Purcell effect in microdisk lasers at room temperature," *IEEE J. Sel. Top. Quantum Electron.,* vol. 9, pp. 1340-1346, 2003.

[82] W. W. Chow and S. W. Koch, *Semiconductor-Laser Fundamentals.* Berlin: Springer, 1999.

[83] J. Masum, D. Ramoo, N. Balkan and M. Adams, "Temperature dependence of the spontaneous emission factor in VCSELs," *IEE Proceedings-Optoelectronics,* vol. 146, pp. 245-251, 1999.

[84] D. M. Ramoo and M. J. Adams, "Temperature dependence of the spontaneous emission factor in microcavities," in *Symposium on Integrated Optoelectronic Devices,* 2002, pp. 157-167.

[85] Z. Liu, J. M. Shainline, G. E. Fernandes, J. Xu, J. Chen and C. F. Gmachl, "Continuous-wave subwavelength microdisk lasers at $\lambda = 1.53$ μm," *Opt. Express,* vol. 18, pp. 19242-19248, 2010.

[86] C. Gies, J. Wiersig, M. Lorke and F. Jahnke, "Semiconductor model for quantum-dot-based microcavity lasers," *Physical Review A,* vol. 75, pp. 013803, 2007.

[87] G. Roelkens, L. Liu, D. Liang, R. Jones, A. Fang, B. Koch and J. Bowers, "III-V/silicon photonics for on-chip and intra-chip optical interconnects," *Laser & Photonics Reviews,* vol. 4, pp. 751-779, 2010.

[88] W. Rideout, W. Sharfin, E. Koteles, M. Vassell and B. Elman, "Well-barrier hole burning in quantum well lasers," *Photonics Technology Letters, IEEE,* vol. 3, pp. 784-786, 1991.

[89] Q. Ding, A. Mizrahi, Y. Fainman and V. Lomakin, "Dielectric shielded nanoscale patch laser resonators," *Opt. Lett.,* vol. 36, pp. 1812-1814, 2011.

[90] F. Vallini, Q. Gu, B. Wingad, B. Slutsky, M. Katz, Y. Fainman and N. Frateschi, "Geometry optimization of nanopatch semiconductor lasers: The trade-off between quality factor and gain," in *Latin America Optics and Photonics Conference,* 2012, pp. LT3B. 2.

[91] M. Rosenzweig, M. Mohrle, H. Duser and H. Venghaus, "Threshold-current analysis of InGaAs-InGaAsP multiquantum well separate-confinement lasers," *IEEE. J. Quantum. Electron.,* vol. 27, pp. 1804-1811, 1991.

[92] S. L. Chuang and S. L. Chuang, *Physics of Optoelectronic Devices.* Wiley New York, 1995.

[93] A. Reisinger, P. Zory Jr and R. Waters, "Cavity length dependence of the threshold behavior in thin quantum well semiconductor lasers," *Quantum Electronics, IEEE Journal of,* vol. 23, pp. 993-999, 1987.

[94] C. Wu and E. Yang, "Physical mechanisms of carrier leakage in DH injection lasers," *J. Appl. Phys.,* vol. 49, pp. 3114-3117, 1978.

[95] H. Casey, "Room-temperature threshold-current dependence of GaAs-Al x Ga 1-x As double-heterostructure lasers on x and active-layer thickness," *J. Appl. Phys.,* vol. 49, pp. 3684-3692, 1978.

[96] N. Dutta, "Calculated temperature dependence of threshold current of GaAs-AlxGa1− xAs double heterostructure lasers," *J. Appl. Phys.,* vol. 52, pp. 70-73, 1981.

[97] K. Y. Lau, "Dynamics of quantum well lasers," in *Quantum Well Lasers*, P. S. Zory, Ed. New York: Academic, 1993, pp. 217-276.

[98] R. Nagarajan, M. Ishikawa, T. Fukushima, R. S. Geels and J. E. Bowers, "High speed quantum-well lasers and carrier transport effects," *Quantum Electronics, IEEE Journal of,* vol. 28, pp. 1990-2008, 1992.

[99] C. Cohen-Tannoudji, J. Dupont-Roc and G. Grynberg, *Photons and Atoms: Introduction to Quantum Electrodynamics.* New York,: Wiley, 1989.

[100] P. B. Johnson and R. Christy, "Optical constants of the noble metals," *Phys. Rev. B,* vol. 6, pp. 4370, 1972.

[101] M. Asada and Y. Suematsu, "Density-matrix theory of semiconductor lasers with relaxation broadening model-gain and gain-suppression in semiconductor lasers," *IEEE. J. Quantum. Electron.,* vol. 21, pp. 434-442, 1985.

[102] J. Van Campenhout, P. Rojo-Romeo, D. Van Thourhout, C. Seassal, P. Regreny, L. Di Cioccio, J. Fedeli and R. Baets, "Thermal characterization of electrically injected thin-film InGaAsP microdisk lasers on Si," *J. Lightwave Technol.,* vol. 25, pp. 1543-1548, 2007.

[103] O. Hess, J. Pendry, S. Maier, R. Oulton, J. Hamm and K. Tsakmakidis, "Active nanoplasmonic metamaterials," *Nat. Mater.,* vol. 11, pp. 573-584, 2012.

[104] C. Ning, R. Indik and J. Moloney, "Self-consistent approach to thermal effects in vertical-cavity surface-emitting lasers," *JOSA B,* vol. 12, pp. 1993-2004, 1995.

[105] S. F. Yu, *Analysis and Design of Vertical Cavity Surface Emitting Lasers.* Wiley-VCH, 2003.

[106] M. Shur, *Handbook Series on Semiconductor Parameters.* World Scientific, 1996.

[107] G. Chen and A. Shakouri, "Heat transfer in nanostructures for solid-state energy conversion," *J. Heat Transfer,* vol. 124, pp. 242-252, 2002.

[108] K. Ding and C. Ning, "Fabrication challenges of electrical injection metallic cavity semiconductor nanolasers," *Semiconductor Science and Technology,* vol. 28, pp. 124002, 2013.

[109] B. M. Green, K. K. Chu, E. M. Chumbes, J. A. Smart, J. R. Shealy and L. F. Eastman, "The effect of surface passivation on the microwave characteristics of undoped AlGaN/GaN HEMTs," *Electron. Dev. Lett.,* vol. 21, pp. 268-270, 2000.

[110] K. Ding and C. Ning, "Metallic subwavelength-cavity semiconductor nanolasers," *Light: Sci. Appl.,* vol. 1, pp. e20, 2012.

[111] M. Shih, M. Bagheri, A. Mock, S. Choi, J. OBrien, P. Dapkus and W. Kuang, "Identification of modes and single mode operation of sapphire-bonded photonic crystal lasers under continuous-wave room temperature operation," *Appl. Phys. Lett.,* vol. 90, pp. 121116-121116-3, 2007.

[112] S. Chu, G. Wang, W. Zhou, Y. Lin, L. Chernyak, J. Zhao, J. Kong, L. Li, J. Ren and J. Liu, "Electrically pumped waveguide lasing from ZnO nanowires," *Nat. Nanotechnol.,* vol. 6, pp. 506-510, 2011.

[113] B. Min, J. S. Lee, K. Cho, J. W. Hwang, H. Kim, M. Y. Sung, S. Kim, J. Park, H. W. Seo and S. Y. Bae, "Semiconductor nanowires surrounded by cylindrical Al2O3 shells," *J. Electron. Mater.,* vol. 32, pp. 1344-1348, 2003.

[114] S. Lee and D. G. Cahill, "Heat transport in thin dielectric films," *J. Appl. Phys.,* vol. 81, pp. 2590-2595, 1997.

[115] S. Yoneoka, J. Lee, M. Liger, G. Yama, T. Kodama, M. Gunji, J. Provine, R. T. Howe, K. E. Goodson and T. W. Kenny, "Electrical and thermal conduction in atomic layer deposition nanobridges down to 7 nm thickness," *Nano Lett.,* vol. 12, pp. 683-686, 2012.

[116] J. R. Wank, S. M. George and A. W. Weimer, "Nanocoating individual cohesive boron nitride particles in a fluidized bed by ALD," *Powder. Technol.,* vol. 142, pp. 59-69, 2004.

[117] E. Dörre and H. Hübner, *Alumina: Processing, Properties, and Applications.* Springer-Verlag Berlin, 1984.

[118] X. Duan, Y. Huang, R. Agarwal and C. M. Lieber, "Single-nanowire electrically driven lasers," *Nature,* vol. 421, pp. 241-245, 2003.

[119] M. W. Kim and P. Ku, "Semiconductor nanoring lasers," *Appl. Phys. Lett.,* vol. 98, pp. 201105-201105-3, 2011.

[120] H. Yang, D. Zhao, S. Chuwongin, J. Seo, W. Yang, Y. Shuai, J. Berggren, M. Hammar, Z. Ma and W. Zhou, "Transfer-printed stacked nanomembrane lasers on silicon," *Nat. Photonics,* vol. 6, pp. 617-622, 2012.

[121] J. G. Bouillard, W. Dickson, D. P. O'Connor, G. A. Wurtz and A. V. Zayats, "Low-temperature plasmonics of metallic nanostructures," *Nano Lett.,* vol. 12, pp. 1561-1565, 2012.

[122] G. Parkins, W. Lawrence and R. Christy, "Intraband optical conductivity σ (ω, T) of Cu, Ag, and Au: Contribution from electron-electron scattering," *Phys. Rev. B,* vol. 23, pp. 6408, 1981.

[123] D. R. Cassidy and G. H. Cross, "Universal method to determine the thermo-optic coefficient of optical waveguide layer materials using a dual slab waveguide," *Appl. Phys. Lett.,* vol. 91, pp. 141914-141914-3, 2007.

[124] F. G. Della Corte, G. Cocorullo, M. Iodice and I. Rendina, "Temperature dependence of the thermo-optic coefficient of InP, GaAs, and SiC from room temperature to 600 K at the wavelength of 1.5 μm," *Appl. Phys. Lett.,* vol. 77, pp. 1614-1616, 2000.

[125] A. Matsudaira, C. Lu, M. Zhang, S. L. Chuang, E. Stock and D. Bimberg, "Cavity-Volume Scaling Law of Quantum-Dot Metal-Cavity Surface-Emitting Microlasers," *IEEE Photon. J.,* vol. 4, pp. 1103-1114, 2012.

[126] A. Forchel, A. Menschig, B. Maile, H. Leier and R. Germann, "Transport and optical properties of semiconductor quantum wires," *J. Vac. Sci. Technol. B,* vol. 9, pp. 444-450, 1991.

[127] D. G. Cahill, "Thermal conductivity measurement from 30 to 750 K: the 3ω method," *Rev. Sci. Instrum.,* vol. 61, pp. 802-808, 1990.

[128] S. Shin, H. N. Cho, B. S. Kim and H. H. Cho, "Influence of upper layer on measuring thermal conductivity of multilayer thin films using differential 3-< i> ω</i> method," *Thin Solid Films,* vol. 517, pp. 933-936, 2008.

[129] K. J. Chen and S. Huang, "AlN passivation by plasma-enhanced atomic layer deposition for GaN-based power switches and power amplifiers," *Semicond. Sci. Technol.,* vol. 28, pp. 074015-1-074015-8, 2013.

[130] J. Tang, Z. Huo, S. Brittman, H. Gao and P. Yang, "Solution-processed core-shell nanowires for efficient photovoltaic cells," *Nature Nanotechnology,* vol. 6, pp. 568-572, 2011.

[131] D. Liang, M. Fiorentino, T. Okumura, H. Chang, D. T. Spencer, Y. Kuo, A. W. Fang, D. Dai, R. G. Beausoleil and J. E. Bowers, "Electrically-pumped compact hybrid silicon microring lasers for optical interconnects," *Optics Express,* vol. 17, pp. 20355-20364, 2009.

[132] M. Heck, J. F. Bauters, M. L. Davenport, J. K. Doylend, S. Jain, G. Kurczveil, S. Srinivasan, Y. Tang and J. E. Bowers, "Hybrid silicon photonic integrated circuit technology," *IEEE Journal of Selected Topics in Quantum Electronics,* vol. 19, 2013.

[133] O. Bondarenko, Q. Gu, J. Shane, A. Simic, B. Slutsky and Y. Fainman, "Wafer bonded distributed feedback laser with sidewall modulated Bragg gratings," *Appl. Phys. Lett.,* vol. 103, pp. 043105-043105-4, 2013.

[134] M. Kim, Z. Li, K. Huang, R. Going, M. C. Wu and H. Choo, "Engineering of metal-clad optical nanocavity to optimize coupling with integrated waveguides," *Opt. Express,* vol. 21, pp. 25796-25804, 2013.

[135] B. Jalali and S. Fathpour, "Silicon photonics," *Lightwave Technology, Journal of,* vol. 24, pp. 4600-4615, 2006.

[136] C. Hahn, Z. Zhang, A. Fu, C. H. Wu, Y. J. Hwang, D. J. Gargas and P. Yang, "Epitaxial growth of InGaN nanowire arrays for light emitting diodes," *ACS Nano,* vol. 5, pp. 3970-3976, 2011.

[137] R. Chen, T. D. Tran, K. W. Ng, W. S. Ko, L. C. Chuang, F. G. Sedgwick and C. Chang-Hasnain, "Nanolasers grown on silicon," *Nature Photonics,* vol. 5, pp. 170-175, 2011.

[138] S. Lourdudoss, "Heteroepitaxy and selective area heteroepitaxy for silicon photonics," *Current Opinion in Solid State and Materials Science,* vol. 16, pp. 91-99, 2012.

[139] R. E. Camacho-Aguilera, Y. Cai, N. Patel, J. T. Bessette, M. Romagnoli, L. C. Kimerling and J. Michel, "An electrically pumped germanium laser," *Optics Express,* vol. 20, pp. 11316-11320, 2012.

[140] J. E. Cunningham, A. V. Krishnamoorthy, R. Ho, I. Shubin, H. Thacker, J. Lexau, D. C. Lee, D. Feng, E. Chow and Y. Luo, "Integration and packaging of a macrochip with silicon nanophotonic links," *IEEE Journal of Selected Topics in Quantum Electronics,* vol. 17, pp. 546-558, 2011.

[141] F. Niklaus, R. Kumar, J. McMahon, J. Yu, J. Lu, T. Cale and R. Gutmann, "Adhesive wafer bonding using partially cured benzocyclobutene for three-dimensional integration," *J. Electrochem. Soc.,* vol. 153, pp. G291-G295, 2006.

[142] D. Liang, A. W. Fang, H. Park, T. E. Reynolds, K. Warner, D. C. Oakley and J. E. Bowers, "Low-temperature, strong SiO2-SiO2 covalent wafer bonding for III–V compound semiconductors-to-silicon photonic integrated circuits," *J Electron Mater,* vol. 37, pp. 1552-1559, 2008.

[143] O. Bondarenko, A. Simic, Q. Gu, J. Lee, B. Slutsky, M. Nezhad and Y. Fainman, "Wafer Bonded Subwavelength Metallo-Dielectric Laser," *IEEE Photon. J.,* pp. 608, .

[144] H. Altug and J. Vuckovic, "Photonic crystal nanocavity array laser," *Opt.Express,* vol. 13, pp. 8819-8828, 2005.

[145] J. Y. Suh, C. H. Kim, W. Zhou, M. D. Huntington, D. T. Co, M. R. Wasielewski and T. W. Odom, "Plasmonic Bowtie Nanolaser Arrays," *Nano Lett.,* vol. 12, pp. 5769-5774, 2012.

[146] H. Zhou, M. Wissinger, J. Fallert, R. Hauschild, F. Stelzl, C. Klingshirn and H. Kalt, "Ordered, uniform-sized ZnO nanolaser arrays," *Appl. Phys. Lett.,* vol. 91, pp. 181112-181112-3, 2007.

[147] S. M. Morris, P. J. Hands, S. Findeisen-Tandel, R. H. Cole, T. D. Wilkinson and H. J. Coles, "Polychromatic liquid crystal laser arrays towards display applications," *Opt. Express,* vol. 16, pp. 18827-18837, 2008.

[148] W. Zhou, M. Dridi, J. Y. Suh, C. H. Kim, M. R. Wasielewski, G. C. Schatz and T. W. Odom, "Lasing action in strongly coupled plasmonic nanocavity arrays," *Nat. Nanotechnol.,* 2013.

[149] H. Abe, M. Narimatsu, S. Kita, A. Tomitaka, Y. Takemura and T. Baba, "Live cell imaging using photonic crystal nanolaser array," *Micro-TAS,* vol. 593, pp. 2011, 2011.

[150] J. Sun, E. Timurdogan, A. Yaacobi, E. S. Hosseini and M. R. Watts, "Large-scale nanophotonic phased array," *Nature,* vol. 493, pp. 195-199, 2013.

[151] R. J. Glauber and M. Lewenstein, "Quantum optics of dielectric media," *Phys. Rev. A,* vol. 43, pp. 467, 1991.

[152] S. W. Chang and S. L. Chuang, "Normal modes for plasmonic nanolasers with dispersive and inhomogeneous media," *Opt. Lett.,* vol. 34, pp. 91-93, 2009.

[153] R. J. Glauber, "Optical coherence and photon statistics," in *Quantum Optics and Electronics,* 1965, pp. 63.

[154] G. Björk, S. Machida, Y. Yamamoto and K. Igeta, "Modification of spontaneous emission rate in planar dielectric microcavity structures," *Phys. Rev. A,* vol. 44, pp. 669, 1991.

[155] K. Srinivasan and O. Painter, "Linear and nonlinear optical spectroscopy of a strongly coupled microdisk–quantum dot system," *Nature,* vol. 450, pp. 862-865, 2007.

[156] G. Khitrova, H. Gibbs, M. Kira, S. Koch and A. Scherer, "Vacuum Rabi splitting in semiconductors," *Nat. Physics,* vol. 2, pp. 81-90, 2006.

[157] V. Weisskopf and E. Wigner, "Calculation of the natural brightness of spectral lines on the basis of Dirac's theory," *Z. Phys.,* vol. 63, pp. 54-73, 1930.